The Application of the Solar Chimney for Ventilating Buildings

David Park

Dissertation submitted to the faculty of the Virginia Polytechnic Institute and State University in partial fulfillment of the requirements for the degree of

Doctor of Philosophy
In
Mechanical Engineering

Francine Battaglia, Chair
Bahareh Behkam
Scott T. Huxtable
Alan A. Kornhauser
Anne E. Staples

October 13, 2016
Blacksburg, VA

Keywords: Natural ventilation, solar chimney, buoyancy-driven flow, building energy, basement

The Application of the Solar Chimney for Ventilating Buildings

David Park

ABSTRACT

This study sought to demonstrate the potential applications of the solar chimney for the naturally ventilating a building. Computational fluid dynamics (CFD) was used to model various room configurations to assess ventilation strategies. A parametric study of the solar chimney system was executed, and three-dimensional simulations were compared and validated with experiments. A new definition for the hydraulic diameter that incorporated the chimney geometry was developed to predict the flow regime in the solar chimney system. To mitigate the cost and effort to use experiments to analyze building energy, a mathematical approach was considered. A relationship between small- and full-scale models was investigated using non-dimensional analysis. Multiple parameters were involved in the mathematical model to predict the air velocity, where the predictions were in good agreement with experimental data as well as the numerical simulations from the present study.

The second part of the study considered building design optimization to improve ventilation using air changes per hour (ACH) as a metric, and air circulation patterns within the building. An upper vent was introduced near the ceiling of the chimney system, which induced better air circulation by removing the warm air in the building. The study pursued to model a realistic scenario for the solar chimney system, where it investigated the effect of the vent sizes, insulation, and a reasonable solar chimney size. It was shown that it is critical to insulate the backside of the absorber and that the ratio of the conditioned area to chimney volume should be at least 10.

Lastly, the application of the solar chimney system for basement ventilation was discussed. Appropriate vent locations in the basement were determined, where the best ventilation was achieved when the duct inlet was located near the ceiling and the exhaust vent was located near the floor of the chimney. Sufficient ventilation was also achieved even for scenarios of a congested building when modeling the presence of multiple people.

The Application of the Solar Chimney for Ventilating Buildings

David Park

GENERAL AUDIENCE ABSTRACT

Energy consumption is an important issue and has become a great concern during the last few decades, where most energy consumption is utilized for conditioning buildings. Natural ventilation is a method to provide fresh air into the building as well as save energy. The solar chimney system is a natural ventilation technique that utilizes solar energy to ventilate buildings. This study sought to demonstrate the potential applications of the solar chimney to naturally ventilate a building. Computational fluid dynamics (CFD) was used to model various room configurations to assess ventilation strategies.

This study presented a computational model to study the performance of a solar chimney system in buildings. To mitigate the cost and effort to use experiments to analyze building energy, a mathematical approach was considered, and relationships between small- and full-scale models were developed. The air velocity through the window was predicted using the geometry of the solar chimney system and building, and outdoor conditions, where the predictions agreed well with the experimental data as well as the numerical simulations from the present study.

In the second part of the study, building designs were modified to improve ventilation rate and thermal condition of the building. Additionally, multiple factors (insulation, vent sizes, and solar chimney size) were considered in an effort to examine the performance of the solar chimney system in a realistic scenario. Lastly, the application of the solar chimney system for basement ventilation was discussed. Appropriate vent locations in the basement were determined, where the best ventilation was achieved when the duct inlet was located near the ceiling and the exhaust vent was located near the floor of the chimney. Sufficient ventilation was also achieved even for scenarios of a congested building when modeling the presence of multiple people.

Acknowledgements

Foremost, I thank God for the opportunity to study this research and also providing great people during my Ph.D. study.

I thank Dr. Francine Batttaglia, my advisor, who once told me that she will teach me everything that she knows. I have continued the journey with her ever since, and I really appreciate her efforts to teach every moment, and to guide me not only to be a fine researcher, but a better person. I also thank Dr. Bahareh Behkam, Dr. Scott Huxtable, Dr. Alan A. Kornhauser, and Dr. Anne Staples for serving on my committee. Their directions and suggestions for the research during the preliminary exam were very helpful to produce this study.

I thank my parents, Seung-Ryong Park and Eun-Bok Lee, for all the support and opportunities for me to study in U.S. I only understand a little about the difficulties of being apart from their children and the sacrifice to provide the best environment for the children. Although thousands miles away, their love never left me, and always supported me to get through the struggles. I thank my brothers, Sam and Paul, for being here during the last year of my Ph.D. study and supporting me through all the struggles. I thank my host family, who treated me as one of their own children and a brother. I could never thank enough for so much love and care.

I thank fellow students in CREST lab: Lu, Jeff, Ryan, and Dr. Wang; It was a blessing to have such great people around me in the lab who were good friends before fellow workers. Lastly, I thank all my friends for always being there during good and bad times.

Table of Contents

List of Tables viii

List of Figures ix

Nomenclature xii

Chapter 1. Introduction and Literature Review 1

1.1. Background 1

1.2. Research Objectives 3

1.3. Outline 5

Chapter 2. Literature Review 6

2.1. Numerical study of natural ventilation 6

2.2. Indoor air quality guidelines 7

2.3. Potential of solar chimney 8

2.4. Small-scale studies 10

2.5. Numerical models of wall-solar chimney 11

2.6. Heat sources 11

Chapter 3. Theory and Numerical Formulation 13

3.1. Governing Equations 13

3.2. Turbulence modeling 14

3.3. Radiation model 15

3.4. Discretization methods 16

3.5. Grid resolution study 17

Chapter 4. Modeling wall-solar chimney 22

4.1. Introduction 22

4.2. Boundary conditions 23

4.3. The effect of H and Z on the flow regime 27

4.4. The effectiveness of the solar chimney 34

4.5. Conclusions 38

Chapter 5. Small and full-scale modeling 39

5.1. Introduction 39

5.2. Boundary conditions 40

5.3. The effect of window-position on thermal condition of the room 42

5.4. Regression analysis 50

5.5. Conclusions 56

Chapter 6. Improvement in the performance of solar chimney system 58

6.1. Introduction 58

6.2. Design modifications to improve ventilation 60

6.2.1. Extended solar chimney (improving ACH) 60

6.2.2. Additional vent (improving thermal condition) 63

6.3. The effect of $Vent_L$ 67

6.4. Disregard solar absorptivity on room floor 73

6.5. The effect of insulation 76

6.6. Realistic size of the solar chimney 79

6.6.1. Smaller width of the solar chimney 80

6.6.2. Smaller air gap (*Z*) 81

6.7. Conclusions 84

Chapter 7. Basement ventilation utilizing solar chimney 86

7.1. Introduction 86

7.2. Location of various vents 88

7.3. Realistic considerations 93

7.4. Human heat sources 97

7.5. Importance of the lower vent in the basement 106

7.6. Conclusions 109

Chapter 8. Conclusions and Future work 111

8.1. Summary 111

8.2. Significance and contribution 113

8.3. Future work 114

References 116

List of Tables

Table 2.1 The allowable operative temperature for naturally ventilated spaces 8

Table 3.1 GCI for ACH, velocity and temperature for fine, medium and coarse grid resolutions 21

Table 4.1 Thermal properties of the walls 25
Table 4.2 Radiation properties of the walls 25
Table 4.3 Summary of ACH comparing experiments and with simulations 30
Table 4.4 Estimated Ra_Z^2 33
Table 4.5 Estimated Ra_H^3 33
Table 4.6 Modified Ra^* 34

Table 5.1 ACH comparisons for middle and top window configurations for varying room size and solar intensity 43
Table 5.2 Constants for the mathematical model in Eq. (5.12) 53
Table 5.3 Summary of random cases to test the mathematical model 55
Table 5.4 Comparison between predicted and simulated velocity for Model B using new cases 55

Table 6.1 Comparison between two boundary conditions for BC_1 61
Table 6.2 Summary of mass flow rate through lower and upper vent, ACH_{total}, and T_{room} 66
Table 6.3 Comparison in mass flow rate through vents, ACH_{total}, and T_{room} for non-adiabatic and adiabatic cases 78
Table 6.4 Mass flow rate, ACH, and room temperature for different width of the solar chimney system 83
Table 6.5 parameter length and surface area that absorbed solar intensity 84

Table 7.1 Conditions and location of vents in the basement 89
Table 7.2 Mass flow rates through various vents 92
Table 7.3 ACH and average temperature 93
Table 7.4 ACH and average temperature for Test E and F 96
Table 7.5 Mass flow rates through vents for Test E and F for no heat and heat 105
Table 7.6 ACH and average temperature for Test E and F for no human, 2 people and 6 people 106
Table 7.7 mass flow rates through vents for Test F and G with two people in each space 109
Table 7.8 ACH and temperature for Test F and G with two people in each space 109

List of Figures

Figure 3.1 Grid cells for the (a) coarse (4 cm) and (b) fine (1.5 cm) grid resolutions 19
Figure 3.2 Average(a) velocity and (b) temperature of multiple planes in the chimney for coarse, medium, and fine grid resolutions 20
Figure 3.3 y^+ at room floor for all grids 21

Figure 4.1 2D view of the wall-solar chimney 22
Figure 4.2 Geometry of wall-solar chimney and room with absorber and window 24
Figure 4.3 Absorbed solar heat flux on building for average solar heat flux on absorber 26
Figure 4.4 ACH with respect to solar chimney for consistent Z = 0.3 m: 28
Figure 4.5 ACH for Z = 0.1 m and H = 0.2 m 29
Figure 4.6 Mean absorber temperature with respect to the solar intensity 31
Figure 4.7 Room temperature with velocity vector for $H = Z = 0.3$ m 36
Figure 4.8 Room temperature with velocity vector at 500 W/m^2 with $Z = 0.2$ m 37

Figure 5.1 Two different domains with window positioned at the (a) middle and (b) top 40
Figure 5.2 Geometry of wall-solar chimney and room with absorber and window positioned at middle of northern wall 41
Figure 5.3 Comparison of domain sizes between small (1 m^3, left) and full (27 m^3, right) rooms 42
Figure 5.4 Average velocity ratio versus d for window position and solar intensity 44
Figure 5.5 Effect of room size d on (a) room temperature, (b) absorber temperature, and (c) nondimensional temperature 45
Figure 5.6 Effect of solar intensity I on (a) room temperature, (b) absorber temperature, and (c) nondimensional temperature 46
Figure 5.7 Velocity (left) and temperature (right) contours at the room centerplane for room volumes of 1 m^3 and 27 m^3 for both window positions 48
Figure 5.8 Temperature contours superimposed with streamlines at three different heights, $L_{20\%}$, $L_{50\%}$, and $L_{80\%}$, for both window positions 49
Figure 5.9 Temperature streamlines through the room for middle (left) and top (right) cases 50
Figure 5.10 Relationship between π_1 and π_2 through π_7 for the window positioned at top (filled, red) and middle (hollow, blue) with solar intensities 52
Figure 5.11 Comparison between predicted π_1 using Eq. (5.12) and simulated π_1 for Model B: cases for the window positioned at top (filled, red), middle (hollow, blue), and turbulent cases from [53] (triangle, green) 54
Figure 5.12 Comparison between predicted π_1 using Eq. (5.12) and simulated π_1 for Model B for test cases in Table 3 55

Figure 6.1 Schematic of the geometry for increasing chimney height (h_c) 59

Figure 6.2 Schematic of the geometry with the additional vent above the absorber 59
Figure 6.3 Absorbed solar intensity for two different surface conditions: 61
Figure 6.4 The effect of r_c on ACH and temeprature (room and absorber) 62
Figure 6.5 Velcoity and temeprature contours superimposed with streamlines for r_c = (a) 1, (b) 1.2, and (c) 1.5 63
Figure 6.6 Velocity and temperature contours for cases with additional vent of (a) 15 cm, (b) 30 cm, and (c) 45 cm..... 64
Figure 6.7 Temperature contours superimposed with streamlines at three different heights, $L_{20\%}$, $L_{50\%}$, and $L_{96.7\%}$, for no vent (top), 15 cm vent (middle), and 30cm vent (bottom) 65
Figure 6.8 Absorbed solar intensity in the system for $Vent_U$ = (a) 15 cm (b) 30 cm and (c) 45 cm 67
Figure 6.9 Velocity and temperature contours for cases with additional vent of (a) 15 cm, (b) 30 cm, and (c) 45 cm..... 68
Figure 6.10 The effect of $Vent_L$ on (a) $mVentL$, (b) $mVentU$, and (c) ACH_{total}..... 70
Figure 6.11 Effect of $Vent_L$ on average temperature of air entering through vents, (a) lower and (b) upper vents, and (c) room temperature..... 71
Figure 6.12 Absorbed solar intensity on the room for *vent* = 15 cm (a) H = 30 cm, (b) 60 cm, and (c) 90 cm 72
Figure 6.13 Absorbed solar intenstiy for the consideration of $\alpha_{floor} = 0.5$ (left) and $\alpha_{floor} = 0$ (right) on the floor..... 73
Figure 6.14 The effect of $Vent_L$ on mass flow rates through (a) lower and (b) upper vents, (c) ACH, and (d) room temperature for the cases with and without α_{floor} 74
Figure 6.15 The effect of upper vent on mass flow rates through (a) lower and (b) upper vents, (c) ACH, and (d) room temperature for the cases with and without α_{floor}..... 76
Figure 6.16 Velocity (top) and temperature (bottom) contours for (a) non-adiabatic and (b) adiabatic walls 78
Figure 6.17 Comparison between full-width and 1/6 width solar chimney..... 80
Figure 6.18 Velocity (top) and temperature with streamlines (bottom) contours at the center of the room for the solar chimney width equal to (a) full width and (b) 1/6 of L_{room} 81
Figure 6.19 Velocity (top) and temerpature (bottom) contours at the center of the room for Z = (a) 1/3 L_{room} and (b) 1/6 L_{room}..... 82

Figure 7.1 Crowded subway stations in Seoul..... 87
Figure 7.2 Schematic of various vent locations for basement ventilation 88
Figure 7.3 Illustration of different vent locations for Test A to D..... 89
Figure 7.4 Velocity (top) and temperature contours superimposed with streamline (bottom) for (a) Test A and (b) Test B 90
Figure 7.5 Velocity (top) and temperature contours superimposed with streamline (bottom) for (a) Test C and (b) Test D 91
Figure 7.6 Schematics for case E (left) and F (right)..... 94

Figure 7.7 Velocity and temperature contours superimposed with streamlines for Test E and F 95
Figure 7.8 Pressure contours for Test E (left) and F (right) (fix case to test) 96
Figure 7.9 Layouts for Test E with consideration of (a) two people and (b) six people in each space 97
Figure 7.10 Temperature contours for Test E (left) and F (right) with no human, two people, and six people at the center of the building (x = 0 m) 99
Figure 7.11 Temperature contours for Test E (left) and F (right) with no human, two people, and six people at x = 1 m 100
Figure 7.12 Temperature contours for Test E (left) and F (right) with no human, two people, and six people at x = 1.5 m 101
Figure 7.13 Temperature contours for Test E (left) and F (right) with no human, two people, and six people at (a) y = 0.2 m and (b) y = 1.5 m for the main room 103
Figure 7.14 Temperature contours for Test E (left) and F (right) with no human, two people, and six people at (a) y= 0.2 m and (b) y = 1.5 m for the basement 104
Figure 7.15 Building layout for Test G with consideration of two people (a) isometric view (b) side view 107
Figure 7.16 Temperature contours superimposed with streamlines for Test F and G at various locations: x = 0 m, y = 0.2 and 1.5 m in the main floor and basement 108

Nomenclature

A_c Cross-sectional area

D Hydraulic diameter (m)

E Total energy

e Emissivity

G Production of turbulence kinetic energy

$\vec{g}$ Gravitational vector

H Height of solar chimney inlet (m)

h Convective heat transfer coefficient (W/m^2-K)

I Solar intensity (W/m^2)

k Turbulence kinetic energy

L_c Characteristic length

P Pressure (Pa)

T Temperature (K)

t Time (s)

$\vec{v}$ Fluid velocity vector (m/s) $\vec{v} = (u, v, w)$

w Width of the room (m)

x Horizontal coordinate

y Vertical coordinate

Z Air gap between absorber plate and glass (m)

z Depth coordinate

Greek Letter

α Absorptivity

β Thermal expansion coefficient (1/K)

ε Turbulence dissipation rate

ϕ Inclination angle for IPWSC

ρ Density of fluid (kg/m^3)

μ Viscosity

θ Converging angle

τ Transmissivity

$\bar{\bar{\tau}}$ Fluid tensor

Subscripts

b Buoyancy

c Chimney

k Mean velocity gradients

p Pressure

t Turbulence

B Basement

H Chimney inlet

L Lower

U Upper

Z Air gap

0 Reference

∞ Ambient condition

Chapter 1. Introduction and Literature Review

1.1. Background

Energy consumption is an important issue and has become a great concern during the last few decades. Fossil fuels (coal, oil, and natural gas) are currently the dominant energy resources, accounting for 82% of energy consumption in U.S [1]. However, burning fossil fuels for our convenience releases carbon dioxide and leads to a greenhouse effect, acid rain, and environment hazards [2]. According to a temperature analysis by Hansen et al. [3] at NASA's Goddard Institute for Space Studies (GISS), the average global Earth temperature has increased approximately by 0.8 °C (1.4°F) since 1880, where most of the warming occurred in the last few decades at a rate of 0.2 °C per decade since 1970.

Another concern is a rapid increase in energy consumption while energy resources are limited. The U.S. Energy Information Administration projected that world energy consumption will increase 56% between 2010 and 2040 [4], from 524 Btu to 820 Btu. Building energy utilization accounts for approximately 41% of total energy consumption in the U.S [5], where most of building energy is used for space heating and cooling purposes.

While considering ventilation of the building, the indoor air quality must be considered. The average person in the U.S. spends more than 90% of their time in buildings [6]. Thus, it is important to maintain comfortable indoor conditions. Natural ventilation has a potential to save energy costs as well as to maintain good air quality within the building [7-10], where natural ventilation is a method to deliver fresh air through buildings creating pressure difference. There are two types of natural ventilation: wind-driven ventilation and stack ventilation (buoyancy-driven ventilation), and occur by wind and buoyancy forces, respectively. Stack ventilation occurs due to presence of vertical pressure difference developed by thermal buoyancy [7]. There are two main ventilation

principles: single-sided and cross ventilation. Single-sided ventilation involves a room with one opening. The temperature difference between the indoor and the outdoor environment creates a pressure difference whereby air moves through an opening. Cross ventilation is usually used for cooling purposes, which relies on wind to transport the cool air into an inlet (window, door, etc.) and to transport the warm interior air through an outlet.

The solar chimney is a cross ventilation technique, which can improve energy usage as well as air quality through the building, and utilizes solar energy to heat air so that it naturally rises due to buoyancy forces in either a vertical or inclined chimney. The solar chimney is often used in conjunction with a solar collector. There are two main types of solar collectors: the wall and the roof solar collector. The chimney is vertically attached to the side of the building for wall-solar collectors, whereas it is positioned at an incline on the roof for the latter [11].

The concept of utilizing solar energy for ventilating buildings first appeared in Greece in the 5th century BC when the Greeks faced fuel shortages. The idea was to build a house that could maximize the use of the Sun's warm rays during winter. Then, the Romans in the 1st century BC realized their massive energy consumption and improved the design by covering south-facing windows with clear materials such as mica or glass [12]. The solar chimney has been in use for centuries, but it has not been attractive due to the increasing use of fossil fuels. Just as in ancient Greece and Rome, the world is experiencing an energy crisis, with rising fuel costs and environmental hazards; thus utilizing natural unlimited sources such as solar energy is an attractive approach to mitigate current issues.

Designing a naturally ventilated building is a greater challenge than designing a mechanically ventilated building because natural ventilation depends on weather, which changes continuously. For a mechanically ventilated building, ambient conditions outside the building are not as

important, and the room can be maintained at comfortable thermal conditions without opening windows or doors. However for a naturally ventilated building, fluctuating ambient temperature, humidity, wind speed, and wind direction must be considered. How the changes in weather affect the airflow in the building is the broader research question. The spatial layout of the building also must be considered when designing a naturally ventilated building. The position and geometry of opening, heat sources, or objects (furniture) are important factors that affect the airflow in the building.

There are several approaches to study the principles of natural ventilation, commonly experimental investigation and numerical analysis. Experiments are suited to study realistic airflow patterns, but it is expensive and time consuming. In addition, it is difficult to study the details of the airflow patterns in a building. One method to model natural ventilation in a building is computational fluid dynamics (CFD), which is a numerical analysis to solve the Navier-Stokes equations and predict the airflow within the building. In contrast to experimental methods, CFD is cost-effective and easy to investigate the effect of changes in geometry on the flow. In addition, CFD provides spatial information giving values for pressure, velocity, temperature, and etc. throughout the entire flow domain. CFD has great potential to become a powerful tool to model natural ventilation in buildings with careful and correct modeling of the problem.

1.2. Research Objectives

The goal of this research is to computationally model a wall-solar chimney system using the commercial software ANSYS Fluent, and investigate the potential energy savings and air quality improvements. The flow and thermal conditions of the building will be evaluated using guidelines from ASHRAE [13] and Baker [14].

Previous literature that utilized numerical modeling to study the wall-solar chimney for different dimensions of chimney geometry only considered a two-dimensional solar chimney with one-directional heat transfer. In addition, the flow was assumed to be laminar and non-radiation absorbing despite the change in dimensions of solar chimney system. Thus, the first part of this study is an attempt to model a solar chimney three-dimensionally for a more realistic simulation of actual flow and thermal conditions of the room. Both laminar and turbulent models are considered and the results are compared and validated with experimental data by Mathur et al. [15]. The initial study also considers the Rayleigh number to relate the dimensions of solar chimney system and determine the transition regime from laminar to turbulent flow.

In reality, it is difficult to analyze flow in the actual size buildings due to its large size. As an alternative, research studies have considered small-scale models since analyzing the actual size of building is impractical. The second part of this study investigates the relationship between a small- and a full-scale model in a room with a solar chimney system. Relationship between a small- and a full-scale model can facilitate using more small-scale models to predict actual flow in larger buildings.

Ventilation rate and thermal conditions are main concerns for this study, which are also important factors to justify the performance of the solar chimney system. The application of the solar chimney system can vary from industrial purposes to residential purposes, where the requirements for the comfort level also varies. In this study, various ways to improve performance of the solar chimney system are investigated, where modifications of key design parameters are considered.

Prior to the investigation on the applications of the solar chimney, the study explores the effect of multiple factors that may be a concern for implementing the solar chimney system in reality.

These factors contain the vent sizes, the effect of solar radiation on the room floor, insulation, and a reasonable chimney size. Efforts ensued to model the building with the solar chimney system more realistic and demonstrate the following flow patterns and overall thermal conditions.

Lastly, the application of the solar chimney for underground space ventilation is studied. The basement spaces are usually cooler compared to outdoor ambient conditions during the summer. Since warm air arises, it is challenging to naturally ventilate the basement space utilizing the outdoor environment. This study investigates the potential use of solar chimney system to provide fresh air to underground spaces as well as to upper level spaces.

1.3. Outline

In Chapter 2, a survey of the study of natural ventilation and the effect of heat sources in the building is summarized. Then, the indoor air quality guidelines will be presented. The rest of Chapter 2 introduces literature that investigates solar chimneys, categorized by the potential of solar chimney, small-scale studies, and the numerical modeling of wall-solar chimney. Chapter 3 will present the theory and numerical formulation in terms of governing equations, turbulence and radiation models, discretization methods, and mesh. Chapter 4 focuses on validation of experimental results and modeling a wall-solar chimney utilizing 3D simulations. Chapter 5 investigates the relationship between a small- and a full-scale models by utilizing two different layouts of the room. The effect of window location on the flow and thermal condition of the room will be also discussed in this chapter. Chapter 6 investigates the optimization of the solar chimney system. In addition, realistic wall conditions concerning conduction and radiation are discussed as well as the appropriate size of the solar chimney system in Chapter 6. Lastly, Chapter 7 considers underground ventilation with realistic considerations.

Chapter 2. Literature Review

2.1. Numerical study of natural ventilation

Studies have been performed to understand the physics of natural ventilation systems, especially using CFD instead of experiments since CFD is more efficient considering time, cost, design modifications, and detailed analysis. Gan [16] utilized CFD to evaluate the effective depth of fresh air in rooms for single-sided buoyancy-driven ventilation. The effect of window opening, heat gains, and outdoor air temperature was investigated to determine acceptable room depth. The effective depth was influenced both by the size and the ratio of the dimensions of window opening, where the height of the window opening had a larger effect on the effective depth compared to the width. The effective depth also increased with the addition of heat gain and cooler outdoor air temperature because of increased room air movement. Peren et al. [17] modeled a room with various roof angles and asymmetric opening positions, where the wind-driven cross ventilation was considered. They found that the roof inclination angle has a significant effect on the volume flow rate, which increased by 22% when the roof inclination angle changed from 0° to 45°. However, the effect of opening location was minimal on the volume flow rate (less than 5%). Nie et al. [18] modeled a residential building with five window-openings in Changsha (China) and studied the effect of different window-opening behavior. In addition, energy consumption was evaluated for different building orientations. Difference between Peren et al. [17] and Nie et al. [18] was that the former study investigated the effect of a single window location in a room, whereas the latter study modeled a building with multiple windows positioned at multiple locations to evaluate the ventilation rate through building. Nie et al. [18] showed the opening location in the building affects the ventilation rate, and the building orientation was also an important factor to improve energy consumption, where the energy consumption was the least when the building was

oriented west for their case in Changsha. Stoakes et al. [19, 20] modeled natural ventilation flows in large, multistory buildings using the commercial software Fluent 6.0. They performed passive cooling and heating cases in whole buildings, and showed the potential of CFD to model natural ventilation in buildings.

While CFD is one of the easier and effective ways to analyze building energy (flow, thermal conditions, pressure, etc.), the main concern for CFD modeling is representing realistic flows. However, accuracy of CFD results compared to experimental studies has improved over the years. Allocca et al. [21] utilized a numerical method to study the effects of buoyancy, wind, and their combination on ventilation rates and indoor conditions, and showed that their CFD results for buoyancy-driven flows had a 10% difference compared to semi-analytical results, and 25% error for combined wind- and buoyancy- driven flow. Cheuong and Liu [22] explored the effects of building interference on natural ventilation using CFD, where airflow rates for cross-ventilation were predicted within an error of 10-15%. Park [23] modeled a single-sided ventilation in a room with heat sources to investigate the airflow patterns and the effect of heat sources on ventilation rates. The study was conducted in both 2D and 3D models, where the predicted neutral level had a difference of 5.6% and 0.08%, respectively.

2.2. Indoor air quality guidelines

Air change per hour (ACH) and thermal condition of the building are important considerations when implementing natural ventilation. ACH simply means movement of a volume of air in an one-hour period [24]. Baker [14] summarized required ACH for typical scenarios:

1. To maintain a minimum air quality (1 – 2 ACH)
2. To remove heat or other pollutant (2 – 15 ACH)
3. To provide perceptible air movement to enhance thermal comfort (0.5 – 2 m/s)

Table 2.1 The allowable operative temperature for naturally ventilated spaces

	T_∞ = 10 °C		T_∞ = 33.5 °C	
Acceptability	**80 %**	**90 %**	**80 %**	**90 %**
Lower limit	17 °C	18.5 °C	25 °C	26 °C
Upper limit	24.5 °C	23 °C	31 °C	30.5 °C

Depending on climate and locations of the buildings, the required ACH may vary, and can be very high, around 50 to 100 ACH to supply sufficient air to enhance thermal comfort (scenario 3). ASHRAE [25] introduced acceptable temperature ranges for naturally conditioned spaces with respect to outdoor air temperature, which is applicable when outdoor air temperature is between 10 °C and 33.5 °C. The range of acceptability changes depending on T_∞, where the upper and lower limits have a linear relationship with a respect to T_∞. The guideline by ASHRAE [25] presents 90% and 80% acceptability limits for the corresponding ambient temperature, and the allowable operative temperature for T_∞ = 10 °C and 33.5 °C is shown in Table 2.1.

Air velocity is also an important factor that determines level of indoor thermal comfort. According to ASHRAE [25], the maximum acceptable velocity is 0.8 m/s when $T_\infty > 25.5°C$ and the maximum acceptable velocity is 0.15 m/s when $T_\infty < 22°C$. For ambient conditions between 22°C and 25.5°C, the maximum velocity allowed is determined by:

$$v_{maximum} = 50.45 - 4.4047T_\infty + 0.096425T_\infty^2 \tag{2.1}$$

2.3. Potential of solar chimney

The idea of utilizing solar energy has attracted research interests due to its potential to save energy as well as maintain acceptable indoor air quality. Khedari et al. [26] investigated the impact of a solar chimney in a room, where the solar chimney successfully reduced heat gain and ensured thermal comfort. They also showed that the use of a solar chimney was more efficient compared

to open windows due to higher temperature differences between the chimney and the surrounding ambient conditions. Another study by Khedari et al. [27] examined the performance of a solar chimney in an air-conditioned building, where electrical consumption of the air conditioner was reduced by 10-20%, disregarding savings in the ventilation fan. Miyazaki et al. [28] utilized CFD simulations and an analytical model to evaluate the efficiency of a solar chimney in a Japanese climate, which showed that the fan shaft power requirement was reduced by 50% in annual total with the use of the chimney.

Studies on the application of a solar chimney have not been limited to passive cooling, but have shown the potential for passive heating in cold seasons by closing the chimney vents and forcing the heated air into the building. Haghighi and Maerefat [29] numerically modeled heat transfer by natural convection and solar radiation in a 2D vented room with a cold external ambient temperature. They showed that the solar chimney during the day improved indoor air quality even with poor solar intensity of 215 W/m^2 and the low ambient temperature of 5 ºC. Lee and Strand [30] utilized EnergyPlus [31] to study effects of different parameters of the chimney in three different climates; Minneapolis, MN (cold), Spokane, WA (mild), and Phoenix, AZ (hot). Ventilation rates were enhanced with increasing chimney height, solar absorptivity, transmissivity, and air gap width, where overall performance of the solar chimney depended on climate conditions. Importantly, the overall annual percentage savings for three different climates were similar, showing the potential use of solar chimney even in cold weather.

Some work has shown that the performance of solar chimneys improves with increasing collector area or height, indicating that the passive cooling process enhances. Al-Kayiem et al. [32] utilized validated numerical model to study the effect of the chimney height and collector area on the performance of a roof-solar chimney, where increase in the flow velocity as well as mass flow

rate were noticeable with increasing chimney height or area. Punyasompun et al. [33] compared the performance of separated solar chimney to combined solar chimney, where more improvement on thermal condition was observable for the room at the higher level utilizing combined solar chimney.

2.4. Small-scale studies

Studies of buildings are often challenging due to their large sizes. There have been studies that utilize small-scale building models due to difficulty with modeling full-scale buildings. Oz et al. [34] experimentally and numerically studied the effectiveness of a solar chimney system in a three-story building, where they utilized a small prototype with a volume of 0.15 m^3. Mathur et al. [15] carried out an experimental study for the performance of a wall-solar chimney system in a room with a volume of 1 m^3 in a contrast to a typical room volume of 27 m^3. Punyasompun et al. [33] also conducted a small parametric study, where each story had a volume of 2.4 m^3. A new study will be presented in Chapter 4 related to the work of Mathur et al. [15].

Small parametric studies can show the potential for saving energy by utilizing solar chimneys as well as provide an understanding of the effect of each parameter on the flow, but may be challenging to predict the actual performance of the solar chimney for full-scale buildings. However, small-scale buildings are less time-consuming and also easier for both experiment and numerical modeling. Previous studies have not focused on finding a clear relationship between small- and full-scale studies, which can be helpful to predict flows in full-scale buildings by utilizing data from small-scale studies, where a relationship between small- and full-scale studies is the focus of Chapter 5.

2.5. Numerical models of wall-solar chimney

As mentioned in section 2.1, performance of the solar chimney improves with increasing size of the solar collector. Introducing some of the numerical work on modeling the wall-solar chimney, Ong and Chow [35] developed a mathematical model of the chimney. They investigated the effects of air gap and solar radiation intensity, where their mathematical model predicted flow rate and temperature of surfaces fairly well compared to experimental results showing differences under 24%. Similarly, a theoretical and experimental study was carried out by Mathur et al. [15], where they adapted numerical modeling from Ong and Chow [35] for the theoretical study. The parametric study by Mathur et al. [15] showed the improvement of air change per hour (ACH) due to the increase in solar intensity and air gap between absorber and glass cover. Bassiouny and Koura [36] carried on with the work by Mathur et al. [15] developed correlations for absorber wall temperature and average air exit velocity to solar intensity.

2.6. Heat sources

In a realistic scenario, buildings consist of multiple heat sources that alters the flow patterns as well as the thermal condition of the building. There are various studies that describe the effect of heat sources in a building using computational simulations. El-Agouz [37] performed two-dimensional simulations to examine the effect of open locations ventilation for room with an internal heat source. A line heat source was placed at the bottom surface, and multiple open locations were tested. The indoor air quality improved by placing openings on the upper wall. Cho and Awbi [38] studied the effect of heat source locations on the mean velocity using multiple regression analysis, where they found lower mean velocity when the heat source was located along the inlet opening. Allocca et al. [21] varied the heat loads from 0 to 1000 W in a room, and observed the increase in air change rate per hour (ACH) with increasing heat loads. Park and

Battaglia [39] investigated the effect of heat sources and furniture on single-sided ventilation, where refrigerator, computer, desk, bookshelves, and radiator were included in the model.

Several studies pursued to model human body. Metabolic rates for the human body can differ by various activities, where a standing average size male corresponds to a 75 W [40]. In general, heat from the human body is rejected in the combination of radiation, convection, evaporation, and respiration, where each accounts for 38.1%, 29%, 24.2%, and 8.7% according to Murakami et al. [41]. However, some of the work considered only the convective heat loss by the human body. Carven and Settles [42] conducted experimental study to capture thermal plume generated by human, and compared the results to numerical simulation, where the effect of radiation, evaporation, and respiration was disregarded. Thermal plume generated by the human body in their CFD model showed a similar shape as the one observed in the experimental study. Stamou and Katsiris [43] conducted an experimental and numerical study to investigate the flow and temperature stratification around the office room considering multiple heat sources. Thermal mannequin was considered in order to model a human body. A constant heat flux was applied for the human body in the numerical simulation, where the prediction error for velocity and temperature was approximately ± 0.03 m/s and ± 0.33°C, respectively [43].

Chapter 3. Theory and Numerical Formulation

3.1. Governing Equations

The commercial software ANSYS Fluent (14.5) is used for all simulations [44]. The Navier-Stokes equations represent the fundamental governing equations for fluid flow. The conservation of momentum is commonly referred as the Navier-Stokes equation. Additionally, conservation of mass and energy are used to solve the velocity and temperature fields in buildings.

The conservation of mass equation, also called the continuity equation is:

$$\frac{\partial \rho}{\partial t} + \vec{\nabla} \cdot (\rho \vec{v}) = 0 \tag{3.1}$$

where ρ is the density, t is time and $\vec{v}$ is the velocity vector. Conservation of momentum is:

$$\frac{\partial}{\partial t}(\rho \vec{v}) + \vec{\nabla} \cdot (\rho \vec{v} \vec{v}) = -\vec{\nabla} p + \vec{\nabla} \cdot \bar{\bar{\tau}} + \rho \vec{g} \tag{3.2}$$

where p is pressure, $\bar{\bar{\tau}}$ is the fluid stress tensor, and $\vec{g}$ is the gravitational vector. The fluid stress tensor for a Newtonian fluid is given by:

$$\bar{\bar{\tau}} = \mu \left[\left(\nabla \vec{v} + \nabla \vec{v}^{T} \right) - \frac{2}{3} \nabla \cdot \vec{v} I \right] \tag{3.3}$$

where μ is the dynamic viscosity of the fluid and I is the identity tensor. The last term of Eq.(3.2) represents the buoyancy force. The Boussinesq model is employed and assumes that density can be treated as a constant except in the buoyancy force term [45]. The approximation is only valid when temperature differences are small so that density variations are very small. Relating changes of density and temperature, the thermal expansion coefficient, β, is:

$$\beta = -\frac{1}{\rho}\left(\frac{\partial \rho}{\partial T}\right)_{p} \approx -\frac{1}{\rho}\frac{\rho_0 - \rho}{T_0 - T} \tag{3.4}$$

where the subscript 0 represents the reference value. Rearranging Eq.(3.4), the Boussinesq approximation can be represented as:

$$(\rho_0 - \rho) \approx \rho\beta(T - T_0) \tag{3.5}$$

Equation (3.5) is used to solve for ρ and substituted into the ρg term of Eq.(3.2). The other ρ terms in Eqs. (3.1) and (3.2) are constant equal to ρ_0. Conservation of energy is:

$$\frac{\partial}{\partial t}(\rho E) + \vec{\nabla}\cdot\left[\vec{v}(\rho E + p)\right] = \vec{\nabla}\cdot \mathrm{k_{eff}}\vec{\nabla}\mathrm{T} + \vec{\nabla}\cdot\left(\overline{\overline{\tau}}_{eff}\cdot\vec{v}\right) \tag{3.6}$$

where E is total energy and k_{eff} represents the turbulent thermal conductivity and fluid thermal conductivity, which considers the turbulent thermal conductivity in addition to fluid thermal conductivity. The viscous heating is also considered in the conservation of energy, which is the second term on the right hand side of the eq. (3.6).

3.2. Turbulence modeling

The realizable k-ε turbulence model was employed in this study, which contains a new formulation for the turbulent viscosity for better predictions for the flows involving rotation, boundary layers, separation, and recirculation [44]. The turbulence kinetic energy, k, and its rate of dissipation, ε, in the flow field are calculated from two additional transport equations. The k-ϵ transport equations [44] are:

$$\frac{\partial}{\partial t}(\rho k) + \vec{\nabla}\cdot(\rho k\vec{v}) = \vec{\nabla}\cdot\left[\left(\mu + \frac{\mu_t}{\sigma_\varepsilon}\right)\vec{\nabla}k\right] + G_k + G_b - \rho\epsilon \tag{3.7}$$

$$\frac{\partial}{\partial t}(\rho\varepsilon) + \vec{\nabla}\cdot(\rho\varepsilon\vec{v}) = \vec{\nabla}\cdot\left[\left(\mu + \frac{\mu_t}{\sigma_\varepsilon}\right)\vec{\nabla}\varepsilon\right] + \rho C_1 S_\epsilon + \rho C_2\frac{\varepsilon^2}{k + \sqrt{\nu\varepsilon}} + C_{1\epsilon}\frac{\varepsilon}{k}C_{3\epsilon}G_b \tag{3.8}$$

where G_k and G_b are the production of turbulent kinetic energy due to mean velocity gradients and buoyancy respectively; μ_t is the turbulent viscosity; $C_{1\varepsilon}$, C_2, and $C_{3\varepsilon}$ are constants; and σ_k and σ_ε are turbulent Prandtl (Pr) numbers for k and ε respectively. The values of these parameters are: $C_{1\varepsilon}$

= 1.44, C_2 = 1.9, σ_k = 1.0, and σ_ε = 1.2. The coefficient $C_{3\varepsilon}$ determines the degree to which ε is affected by buoyancy and is calculated using a relationship between the velocity vector parallel and perpendicular to the gravitational vector. Further details can be found in the Fluent manual [44].

3.3. Radiation model

Radiative heat transfer is solved using the Discrete Ordinate (DO) radiation model [44], which models semi-transparent surfaces. The DO model can be either uncoupled or coupled with energy equations in Fluent. The equations for the energy and radiation intensities are solved one by one when uncoupled [46], and they are solved simultaneously at each cell when coupled assuming that spatial neighbors are known [47]. The coupled method is useful for the applications involving high optical thicknesses or high scattering coefficients. However, one of the limitations of DO/Energy coupling is that it is not compatible with the shell conduction model, which was utilized in the study. The shell conduction model adds thermal resistance to the physically zero-thickness wall by specifying material property and thickness. Thus, the uncoupled method was employed for the current problem.

A solar load model in Fluent calculates the radiation effects from the sun's rays that enter a computational domain. The solar load model includes a solar calculator which has options to control sun's locations for a given time of day, date, and position [44]. There are two algorithms for a solar model: solar ray tracing and DO irradiation. The solar ray tracing algorithm computes the heat flux on the boundary faces depending on the directions and magnitude of the incident solar radiation. In the contrary for the DO irradiation option, the irradiation flux is applied directly to the semi-transparent walls as a boundary condition. Solar ray tracing algorithm is chosen for the

current problem since the domain includes ambient outside of the building and the effect of incident solar radiation on opaque wall is as important as its effect on the semi-transparent walls.

3.4. Discretization methods

The segregated pressure-based Navier-Stokes (PBNS) solver is used. The pressure-based solver employs the projection method, an effective method to numerically solve incompressible fluid-flow problems [48]. In the projection method, conservation of mass is rewritten as pressure that becomes the primitive variable. One of the segregated algorithms, the semi-implicit method for pressure-linked equations (SIMPLE) is chosen to solve pressure-velocity coupling. In the SIMPLE algorithm, the momentum equations are initially solved with guessed pressure field p^*, where p^* is used to solve the velocity field $\vec{v}^*$. The corrections to velocity field and pressure are proposed so that the final velocity field satisfies continuity. The final velocity field and pressure can be expressed as:

$$\vec{v} = \vec{v}^* + \vec{v}' \tag{3.9}$$

$$p = p^* + p' \tag{3.10}$$

where $\vec{v}'$ and p' are velocity field correction and pressure correction, respectively. The relationship between the velocity and pressure corrections can be expressed as:

$$\vec{v}' = -\frac{1}{A_p}\sum_l A_l \vec{v}' - \frac{1}{A_p}\nabla p'\Big|_p \tag{3.11}$$

where A_P and A_l are coefficients included in the momentum equations. The subscripts P and l represent an arbitrary velocity node and the neighbor points that appear in the discretized momentum equation. Combining the discretized continuity equation to corrected velocities and Eq. (3.9) produces the pressure-correction equation:

$$\nabla[\frac{\rho}{A_p}\nabla p'|]_P = [\nabla(\rho\vec{v}^*)]_P + [\nabla(\rho\vec{v}')]_P \tag{3.12}$$

At this point, the velocity corrections $\vec{v}'$ are unknown so the second term on the right hand side of Eq. (3.12) is neglected. The pressure correction is found using Eq. (3.12), which is then substituted into Eq. (3.11) to obtain the velocity correction. Once the velocity and pressure correction has been solved, the velocity fields and pressure are updated using Eqs. (3.9) and(3.10), respectively [49].

Fluent uses a finite volume approach for discretization. The transport equations are integrated over a finite volume defined by a grid element and calculates the dependent variables (e.g. $\vec{v}$,T) at the center of each cell. From these cell centered solutions, values at each face are interpolated using an upwind scheme. In the current study, momentum, energy and turbulent kinetic energy and dissipation rates are discretized using second-order upwind, which uses Taylor series expansions of the upstream cell centered-solution about the cell centroid to calculate the solutions at the faces of each cell. For the gradient and pressure spatial discretization, least squares cell based (LSCB) and PRESTO! are applied, respectively. Time is discretized using a first-order implicit method. The Courant-Friedrichs-Levy (CFL) number of 1 is chosen to determine time step size, where the CFL can be expressed as:

$$CFL = \frac{U\Delta t}{\Delta x} \tag{3.13}$$

U is the maximum fluid velocity. The time step size and smallest cell size are expressed as Δt and Δx, respectively. The absolute convergence criteria are set as 10^{-5}.

3.5. Grid resolution study

The discretization error is studied using the grid convergence index (GCI). The GCI is proposed by Roache [50] for uniform reporting of grid convergence studies. The GCI is based on the Richardson extrapolation [51], where the discrete solutions are assumed to have a series representation of the discretization error. The GCI converts the Richardson extrapolation error

estimate into an uncertainty by using absolute values to provide an uncertainty bounds and using a factor of safety F_s. The GCI can be represented as:

$$GCI = \frac{F_s}{r^p - 1}\left|\frac{f_2 - f_1}{f_1}\right| \tag{3.14}$$

where r is the grid refinement factor, p is the order of accuracy. Solutions for fine, medium, and coarse grids are subscripted with 1, 2, and 3, respectively. The grid refinement factor r for two-dimensional study is:

$$r = \left(\frac{N_1}{N_2}\right)^{0.5} \tag{3.15}$$

where N is the number of cells or elements. The order of accuracy is then estimated by using the following equation:

$$p = \frac{\ln\left(\frac{f_3 - f_2}{f_2 - f_1}\right)}{\ln(r)} \tag{3.16}$$

Two factor of safety values are recommended by Roache for GCI, 3 and 1.25. For grid resolution studies using two grid solutions to determine the observed order of convergence p, F_s = 3 is recommended. For three or more grid solutions, F_s = 1.25 is adequately conservative.

A similar grid resolution study was previously done by Park and Battaglia [39] for the case of single-sided natural ventilation in a room with a volume of 50 m^3. Their study determined that a uniform grid spacing of 6 cm is appropriate to obtain accurate numerical solutions as well as to save CPU time for natural ventilation in such size of the room. In the current study, three grid resolutions were compared for uniform grid spacing of 4 cm, 2 cm, and 1.5 cm for coarse, medium, and fine grids, respectively. Number of cells for coarse, medium, and fine grids is 41196, 176989 and 344286, respectively, where the mesh for the coarse and fine grids is shown in Figure 3.1.

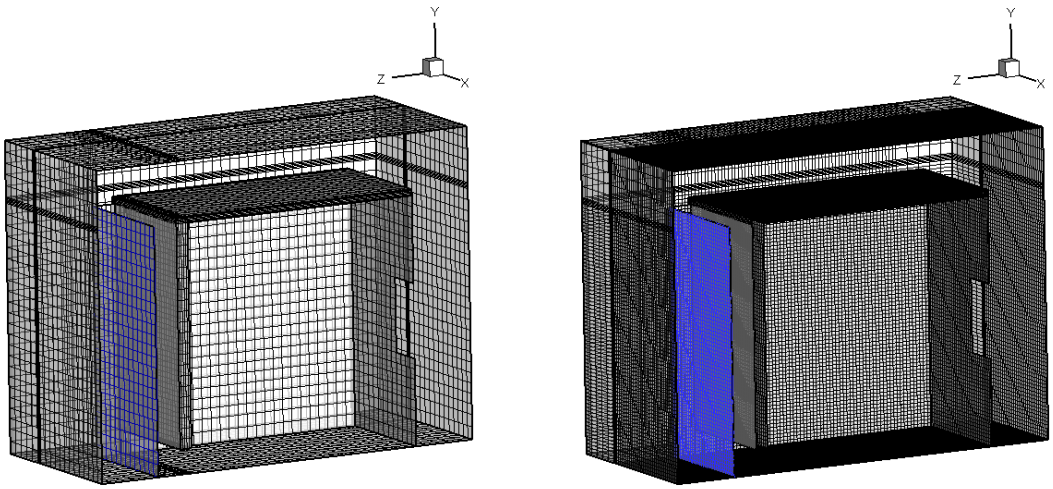

(a) (b)

Figure 3.1 Grid cells for the (a) coarse (4 cm) and (b) fine (1.5 cm) grid resolutions

The volume of the room tested is 1 m^3, where the layout will be further described in Chapter 4.2 Boundary conditions. The average velocity and temperature at different heights in the chimney are plotted in Figure 3.2 (a) and (b), respectively. The difference between grid resolutions is minor, but slight improvement in error is noticeable as the grid cell gets finer. Examining average velocity profile in Figure 3.2 (a), the difference is smaller for finer grids, where average velocity profile slightly deviates from the other two.

Grid convergence index (GCI) study was calculated in order to determine appropriate grid spacing. GCI is calculated for ACH, average velocity and temperature of multiple planes in the chimney shown in Table 3.1 The GCI for the fine grid, GCI_{12}, was relatively low compared to that for the medium grid, GCI_{23}, showing that the grid refinement is successful. Low values of GCI also indicate that the dependency of the numerical simulation on the cell size is low.

In order to determine appropriate grid size for the current model, dimensionless wall distance is investigated. The law of the wall is based on dimensionless wall distance, y^+ [52]:

$$y^+ = \frac{u_* y_*}{\nu} \tag{3.17}$$

where u_* is the friction velocity and ν is the kinematic viscosity of the fluid. The near wall node is subscripted with * and y_* is the distance from the wall to the node *. It is recommended by

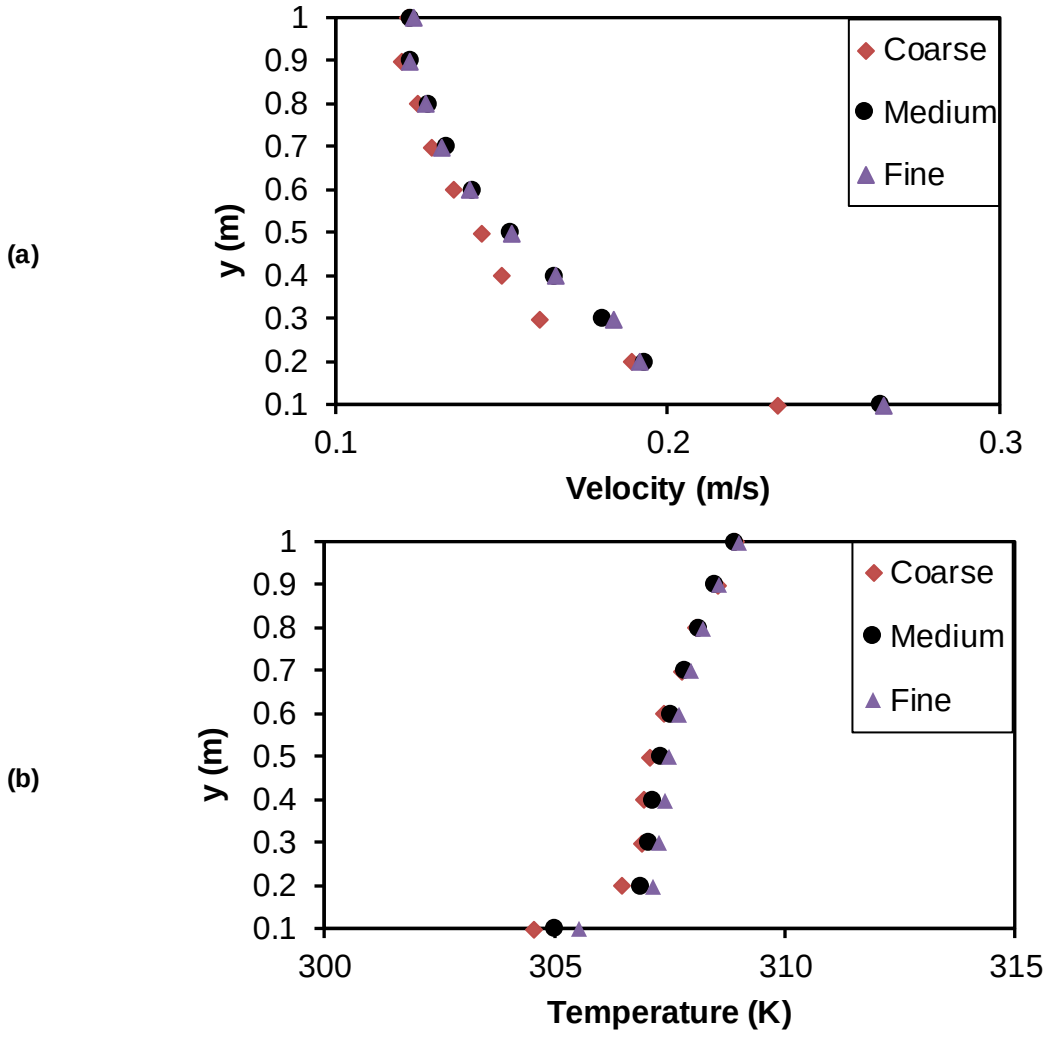

Figure 3.2 Average(a) velocity and (b) temperature of multiple planes in the chimney for coarse, medium, and fine grid resolutions

Table 3.1 GCI for ACH, velocity and temperature for fine, medium and coarse grid resolutions

	Coarse	Medium	Fine	GCI_{23} (%)	GCI_{12} (%)
# of cells	41196	176989	344286		
ACH	4.48	4.46	4.45	1.68	1.26
$V_{Chimney}$ (m/s)	0.234	0.239	0.241	1.22	0.29
$T_{Chimney}$ (K)	307.5	309.0	309.5	0.43	0.36

Fluent [52] that the adjacent wall cell centroid is placed within the log-law layer, $30 < y^+ < 300$. Figure 3.3 shows y^+ values for all grids at the room floor. The recommended limits are shown in dashed lines(black). The adjacent wall cell centroid for the coarse grid is located at $y^+ > 300$, whereas it is located between $30 < y^+ < 300$ for the medium and fine grids. Thus, the medium grid resolution (uniform cell size of 2 cm) is used for the remainder of the study to obtain accurate solutions (compared to coarse) as well as to save CPU time (compared to fine).

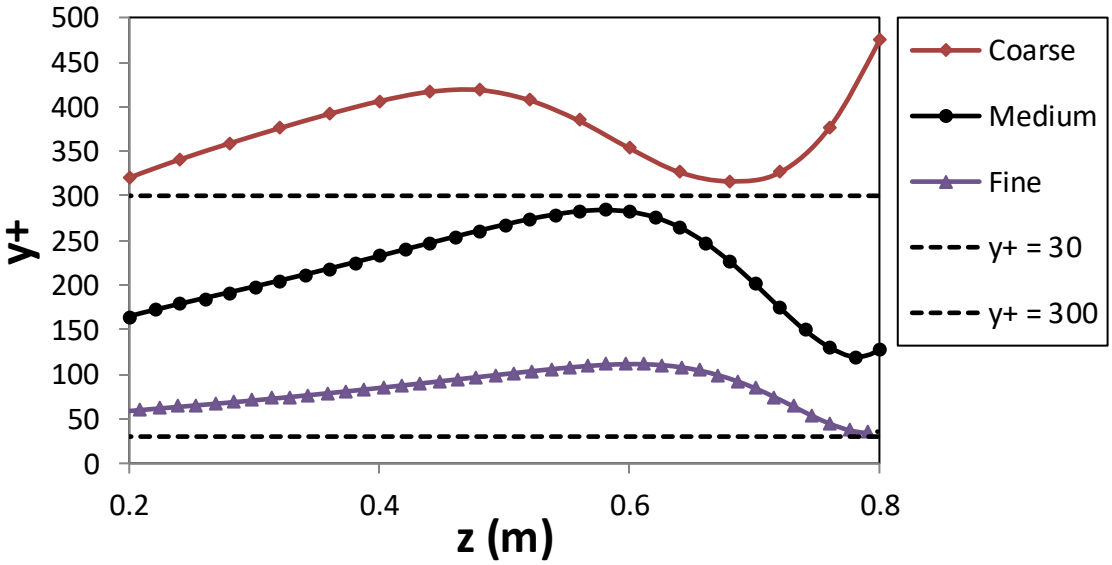

Figure 3.3 y^+ at room floor for all grids

Chapter 4. Modeling wall-solar chimney

The majority of this chapter is produced from [53] with permission from the Journal of Solar Energy Engineering:Park, D. and Battaglia, F., 2015, "Application of a Wall-Solar Chimney for Passive Ventilation of Dwellings" *Journal of Solar Energy Engineering*, 137(6), pp.061006-1-8

4.1. Introduction

The objective of the current study is to examine the effects of the wall-solar chimney on airflow distribution and thermal conditions in a room, where the 2D view of the wall-solar chimney is shown in Figure 4.1. Few numerical works on modeling the wall-solar chimney were previously introduced in 2.5. It is worth noting that previous numerical modeling [15, 35, 36] only utilized two-dimensional representations to model wall-solar chimneys, disregarding not only the effect of area difference between window and vent, but also heat transfer in all directions (other than

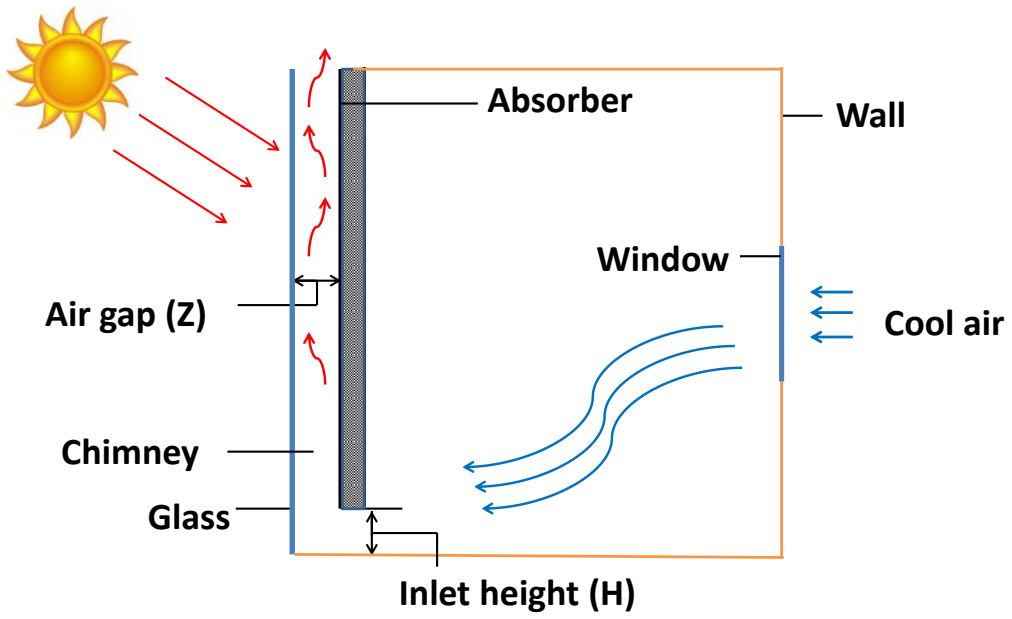

Figure 4.1 2D view of the wall-solar chimney

horizontal directions). Additionally, the flow was assumed to be laminar and non-radiation absorbing fluid.

Three-dimensional modeling is necessary to simulate realistic conditions in the building and to gain a better understanding of which flow and thermal conditions affect the chimney. The current study utilizes ANSYS Fluent to model the wall-solar chimney. While all the other work considered the flow to be laminar in two-dimensional space, more realistic modeling is approached utilizing three dimensions considering both laminar and turbulent models. The air gap (Z) and the chimney inlet (H) varied from 0.1 m to 0.3 m, and solar intensity of 300, 500, and 700 W/m^2 are tested. Air change per hour is validated for each case by comparing to published experiments [15] and numerical modeling [15, 36]. The current work uses the Rayleigh number to investigate the effect of both Z and H on the flow regime, whereas previous studies only focused on the effect of air gap. The flow regime as well as Ra number for each case are further examined to develop a new Ra* that can be utilized for the wall-solar chimney system. Lastly, the flow and thermal conditions of the room are visually shown to discuss the potential improvements of designs.

4.2. Boundary conditions

Figure 4.2 shows the 3D computational domain and interior features of the room and the chimney that replicates the experimental study of Mathur et al. [15]. The experiment consisted of a cubical wooden chamber having a size of 1 m × 1 m × 1 m and insulated with 2.5 cm thick thermocol (EPS) sheets outside of the chamber. The air gap and chimney inlet ranged from 0.1 to 0.3 m with increments of 0.1 m. The window was placed 0.5 m high on the northern wall with dimensions of 0.3 m × 0.3 m. The absorber plate and glass were facing south, where 5 cm insulation was provided on the backside of the absorber plate to prevent heat transfer from the chimney to the room. For the current study, only one-half of the room is modeled using a symmetry boundary

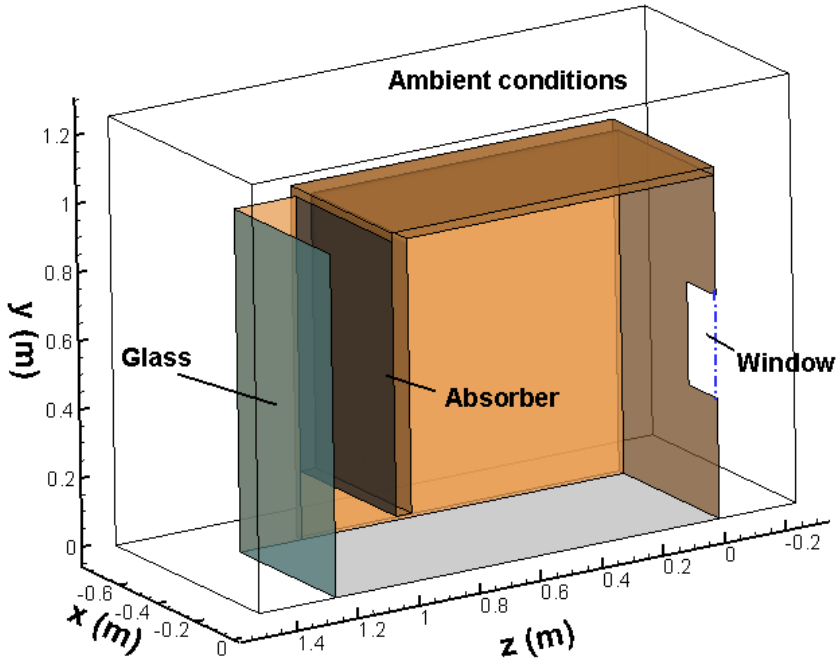

Figure 4.2 Geometry of wall-solar chimney and room with absorber and window

condition at the center of the room to save CPU time with domain having the size of 0.75 m × 1.25 m × (1.65–1.85) m in x, y, and z directions, where the variance in z is due to the variable air gap from 0.1 m to 0.3 m. The computational domain is extended beyond the building to represent the ambient environment as well as to reduce the effect of boundary conditions on the solutions. Uniform grid spacing of 2 cm is chosen for the room and the chimney, and uniform grid spacing of 5 cm is used for the ambient conditions. The grid has 31 × 56 × (68-78) cells.

The ambient conditions at the boundary are represented by specifying ambient pressure of 1 atm and temperature of 27 °C. Standard wall functions are used for the turbulence model and the

Table 4.1 Thermal properties of the walls

Materials	ρ (kg/m^3)	C_p (kJj/kg-k)	k (W/m-k)
Glass	2220	0.83	1.15
Absorber plate	2719	0.871	202.4
Wood	750	2.39	0.17
Thermocol (EPS)	10	0.83	0.1

Table 4.2 Radiation properties of the walls

Materials	α	ε	τ
Glass	0.06	0.95	0.84
Absorber plate	0.95	0.95	0
Wood	0.5	0.5	0

no-slip condition is applied for the fluid-wall interaction. The wall is modeled as non-adiabatic to consider conduction, convection and radiation heat transfer.

The thermal and radiation properties of the wall materials can be found in Table 4.1 and Table 4.2, respectively. Low thermal conductivity (k) is noticeable for wood and thermocol (expanded polystyrene styrofoam), which is utilized for insulation of the room. The transmissivity of the absorber plate and wood is 0 since they are opaque walls. Solar radiation is modeled outside the domain with an angle of 55°. The effect of solar heat flux on the room is visually presented in Figure 4.3. The absorbed heat flux on the surface depends on the solar radiation, the absorptivity of the wall and the layout. Two regions of solar intensity can be noticed on the absorber plate due to the solar angle, where a portion of solar radiation transmits through the glass and the other directly enter through the chimney outlet. The solar radiation is controlled to obtain average absorbed solar intensity (I) from 300 to 700 W/m^2 on the absorber. The floor is also considered in the radiation model, where a little portion of the room floor is affected by the solar radiation in addition to the floor in the chimney.

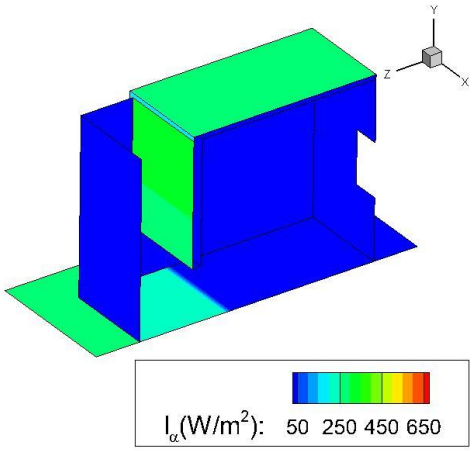

(a) 300 W/m^2

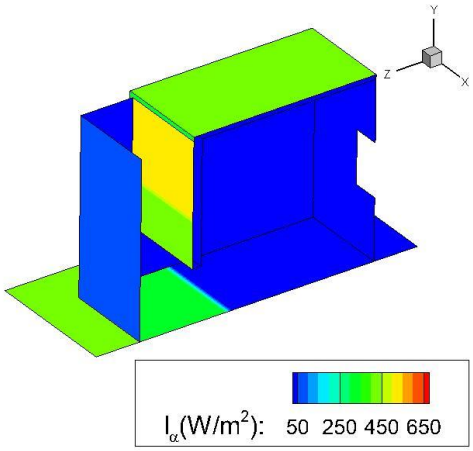

(b) 500 W/m^2

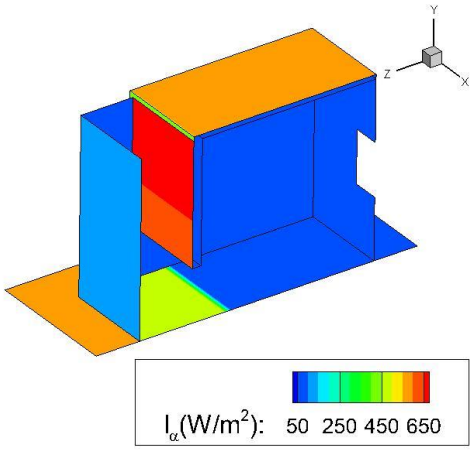

(c) 700 W/m^2

Figure 4.3 Absorbed solar heat flux on building for average solar heat flux on absorber *I* = (a) 300 W/m^2, (b) 500 W/m^2, and (c) 700 W/m^2

4.3. The effect of H and Z on the flow regime

The change in ACH is investigated by varying the solar intensity and testing both laminar and turbulence modeling. Predictions are compared to the experiments and simulations of Mathur et al. [15] and numerical work of Bassiouny and Koura [36]. The air gap Z is constant at 0.3 m and H varies from 0.1 to 0.3 m, shown in Figure 4.4 (a)-(c), respectively. ACH is calculated:

$$ACH = \frac{\dot{V}}{V_{room}} \tag{4.1}$$

where $\dot{v}$ is volume flow rate. The room volume of 27 m^3 is used for the calculation to be consistent with the calculations in [15] just in this chapter, and later actual volume of the room is utilized for ACH calculation. Both laminar and turbulent models are only tested for $I = 300$ W/m^2 to determine which model should be used for the other solar intensities for a fixed H and Z. The laminar model agrees very well with the experiments when $H = 0.1$ m (a), but the flow is predicted to be turbulent for $H \geq 0.2$ m (b and c). Such results indicate that the chimney inlet affects the flow regime, where turbulent flow is predicted with increasing H. The outlier in Figure 4.4 (b) for the experimental data is presumed to be an error, where the other results showed a linear relationship between ACH and the solar intensity.

The logic from the results in Figure 4.4 is that the laminar model for $H = 0.1$ m and turbulent model for $H \geq 0.2$ m agreed well with the other cases, except the case with $H = 0.2$ m and $Z = 0.1$ m, shown in Figure 4.5. Despite the results for $H = 0.2$ m, the laminar model agrees very well with the experiments, whereas the turbulence model over-predicts ACH. Over-prediction also continues for $I = 500$ W/m^2 using the turbulence model. The sudden increase in ACH at $I = 700$ W/m^2 for the experiment is noticeable, where it is presumed to be an error, not following the linear relationship between ACH and solar intensity.

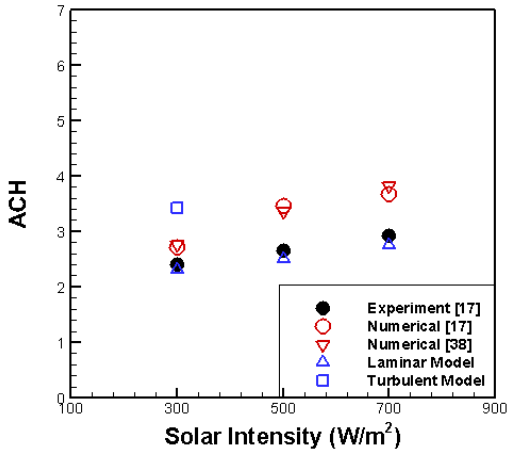

(a) H = 0.1 m and Z = 0.3 m

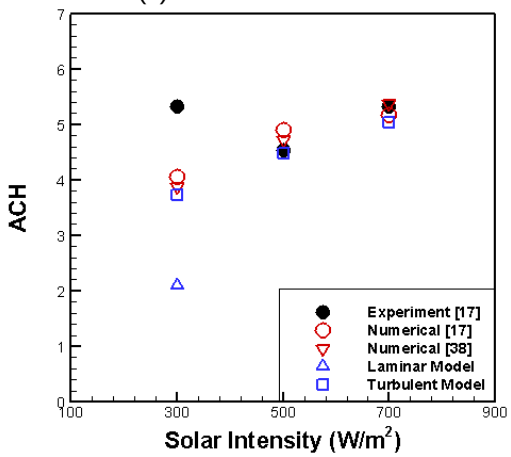

(b) H = 0.2 m and Z = 0.3 m

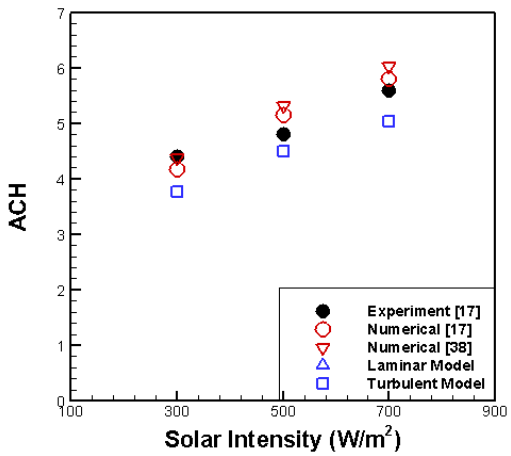

(c) H = 0.3 m and Z = 0.3 m

Figure 4.4 ACH with respect to solar chimney for consistent Z = 0.3 m: (a) H = 0.1 m, (b) H = 0.2 m and (c) H = 0.3 m

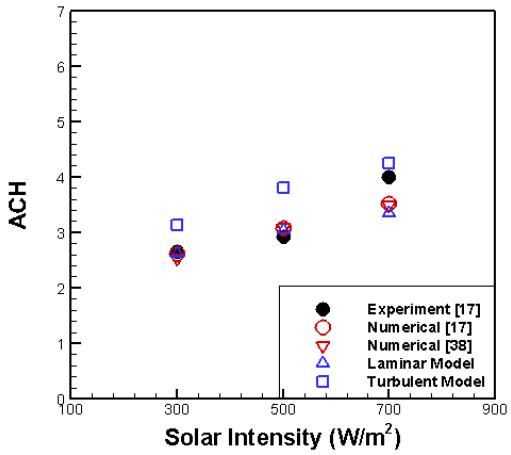

Figure 4.5 ACH for Z = 0.1 m and H = 0.2 m

ACH for all other cases are summarized and compared with experimental and numerical data by Mathur et al. [15] and numerical data by Bassiouny and Koura [36] (B&K) in Table 4.3. ACH for cases (a) to (d) are from the laminar model and the other cases are from the turbulent model. Overall, ACH for the present study has better consistency compared to other numerical results, where the overall error is 6.62% compared to 16.1 and 14.3% for numerical modeling by Mathur et al. [15] and B&K [36]. Comparing case (c) and (g), air gap and chimney inlet for case (c) are 0.3 m and 0.1 m and inversely 0.1 m and 0.3 m for case (g). While the product of H and Z are the same, the flow is different where turbulent flow is predicted for case (g). This indicates that H has a more significant effect on determining the flow-regime compared to Z. However, the effect of Z cannot be disregarded. Mathur et al. [15] stated that ACH improves with increasing air gap, which is consistent with the present study as well, and ACH is largest for case (g) and (i) when $Z = 0.3$ m. Moreover, the effect of Z on the flow regime is noticeable from Tab. 2, where the transition occurs as Z increases from 0.1 m to 0.2 m comparing case (e) and (d). Such results imply that both

Table 4.3 Summary of ACH comparing experiments and with simulations

Cases	Air gap (Z) (m)	Chimney inlet (H) (m)	ACH											
			300 W/m^2				500 W/m^2				700 W/m^2			
			Experiment	Mathur etal	B&K	Present	Experiment	Mathur etal	B&K	Present	Experiment	Mathur etal	B&K	Present
Laminar Flow regime														
(a)	0.1	0.1	2.00	2.49	2.24	**2.68**	2.40	2.99	2.73	**3.14**	2.66	3.12	3.11	**3.48**
(b)	0.2	0.1	2.80	2.94	2.65	**2.77**	2.00	3.39	3.22	**3.21**	3.73	3.87	3.67	**3.50**
(c)	0.3	0.1	2.40	2.70	2.76	**2.30**	2.66	3.46	3.36	**2.50**	2.93	3.67	3.82	**2.74**
(d)	0.1	0.2	2.66	2.60	2.53	**2.62**	2.93	3.06	3.08	**3.03**	4.00	3.51	3.50	**3.35**
Turbulent Flow regime														
(e)	0.2	0.2	4.53	3.63	3.48	**3.62**	4.26	4.04	4.23	**4.38**	3.73	4.68	4.80	**4.92**
(f)	0.3	0.2	5.33	4.05	3.89	**3.73**	4.53	4.89	4.73	**4.48**	5.33	5.17	5.37	**5.03**
(g)	0.1	0.3	3.20	2.40	2.51	**3.07**	4.00	3.0	3.06	**3.66**	4.40	3.52	3.47	**4.17**
(h)	0.2	0.3	4.00	3.61	3.70	**3.57**	5.20	4.20	4.50	**4.25**	5.20	4.94	5.11	**4.80**
(i)	0.3	0.3	4.40	4.17	4.37	**3.77**	4.80	5.16	5.31	**4.49**	5.60	5.81	6.03	**5.04**

parameters of the solar chimney system are important to determine the flow-regime, but the effect of the chimney inlet is more significant than of the air gap.

When considering natural convection, Grashof (Gr) and Rayleigh (Ra) number play an important role to determine the type of the flow, either laminar or turbulent. Gr is interpreted as the ratio of the buoyancy forces to the viscous forces and Ra is defined as the product of the Gr

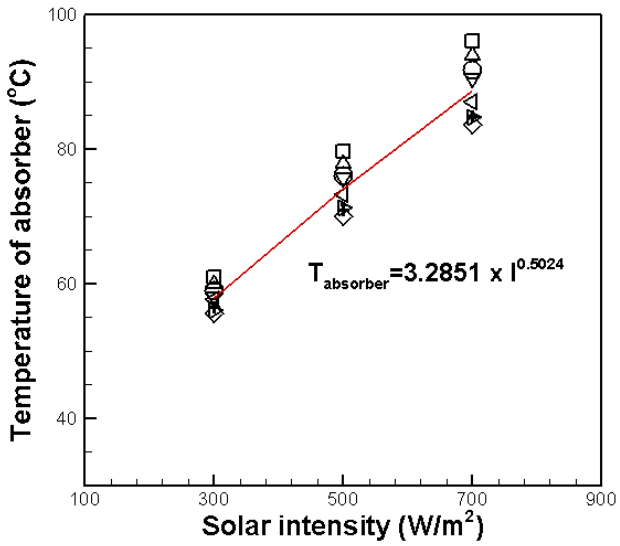

Figure 4.6 Mean absorber temperature with respect to the solar intensity

and Prandtl (Pr) number [54]. The flow is considered as laminar for Ra < 10^8, and turbulent for Ra > 10^9. The transition from laminar to turbulent occurs when Ra is between 10^8 and 10^9.

Further investigation on the flow type and the solar chimney system is conducted by calculating Ra for each case, where Gr is calculated using:

$$Gr = \frac{g\beta(\Delta T)D_h^{\,3}}{\nu^2} \tag{4.2}$$

where ΔT is the temperature difference between the absorber and ambient conditions, and ν is the kinematic viscosity. D_h is a hydraulic diameter:

$$D_h = \frac{4A_C}{P} = \frac{4(L_C w)}{2(L_C + w)} = \frac{2(L_C w)}{(L_C + w)} \tag{4.3}$$

where w is width of the room, and L_C is a characteristic length, which is equal to either H or Z. The mean absorber temperature with respect to the solar intensity for all cases is shown in Figure 4.6. A correlation for the absorber temperature is developed using the predicted mean temperatures for each case by varying the solar intensity:

$$T_{absorber} = 3.2851 \times I^{0.5024} \tag{4.4}$$

which is utilized to estimate the temperature difference between the absorber and the air as well as the mean temperature. Equation (4.4) is slightly different to the correlation developed by Bassiouny and Koura [36], which may be due to the consideration of heat transfer in all three-directions rather than just a horizontal direction in A 2D domain. The Rayleigh number is calculated by multiplying Gr and Pr. The Rayleigh numbers Ra_Z and Ra_H are summarized in Table 4.4 and Table 4.5, where D_Z and D_H are the hydraulic diameter based on Z and H, respectively. The first four cases are predicted to be laminar flow and the last five cases are turbulent flow as shown in Tab 2. However for some cases in Table 4.4 and Table 4.5, Ra contradicts the predicted flow and does not show a clear trend that distinguishes between laminar and turbulent flow, where the outliers are bolded font. Interestingly, more outliers are noticeable for Ra_Z in Table 4.4 compared to Ra_H in Table 4.5. Earlier investigations indicated that the effect of H is more significant than the effect of Z on the flow regime. Following such logic, a new Ra* is developed, where the new hydraulic diameter (D^*_{HZ}) accounts for the effect of both parameters in the solar chimney system as well as a more significant effect of H on the flow by squaring D_H:

$$D^*_{HZ} = (D_H^2 \times D_Z)^{\frac{1}{3}} \tag{4.5}$$

The new hydraulic diameter, D^*_{HZ} is substituted into Eq.(4.2) for D_h, and Ra* is obtained by multiplying the resulting Gr* with Pr and summarized in Table 4.6. A clear trend with the predicted flow is noticeable, where the flow is laminar for $Ra^* \sim 0.79 \times 10^8$ and turbulent for $Ra^* \geq 0.87 \times 10^8$. The result supports earlier findings that both the chimney inlet and air gap affect the flow in the chimney with the chimney inlet influencing the flow regime more significantly. In summary, the new Ra* can be utilized to determine the type of the flow for the wall-solar chimney system and that transition from laminar to turbulent occurs at $Ra^* \sim 0.8 \times 10^8$.

Table 4.4 Estimated Ra_Z[2]

Cases				I = 300 W/m²	500 W/m²	700 W/m²
	Z (m)	H (m)	D_H (m)	Ra_Z (×10⁸)		
	Predictions indicate that flow should be laminar					
(a)	0.1	0.1	0.18	0.14	0.20	0.23
(b)	0.2	0.1	0.33	0.87	**1.21**	**1.45**
(c)	0.3	0.1	0.46	**2.32**	**3.22**	**3.84**
(d)	0.1	0.2	0.18	0.14	0.20	0.23
	Predictions indicate that flow should be turbulent					
(e)	0.2	0.2	0.33	**0.83**	1.15	1.37
(f)	0.3	0.2	0.46	2.20	3.05	3.63
(g)	0.1	0.3	0.18	**0.13**	**0.19**	**0.22**
(h)	0.2	0.3	0.33	**0.83**	1.15	1.37
(i)	0.3	0.3	0.46	2.20	3.05	3.63

[2] *Bolded numbers indicate when Ra values are outliers of flow regime*

Table 4.5 Estimated Ra_H[3]

Cases				I = 300 W/m²	500 W/m²	700 W/m²
	Z (m)	H (m)	D_H (m)	Ra_H (×10⁸)		
	Predictions indicate that flow should be laminar					
(a)	0.1	0.1	0.18	0.14	0.20	0.23
(b)	0.2	0.1	0.33	0.14	0.20	0.23
(c)	0.3	0.1	0.46	0.14	0.20	0.23
(d)	0.1	0.2	0.18	0.87	**1.21**	**1.45**
	Predictions indicate that flow should be turbulent					
(e)	0.2	0.2	0.33	**0.87**	1.21	1.45
(f)	0.3	0.2	0.46	**0.87**	1.21	1.45
(g)	0.1	0.3	0.18	2.32	3.22	3.84
(h)	0.2	0.3	0.33	2.32	3.22	3.84
(i)	0.3	0.3	0.46	2.32	3.22	3.84

[3] *Bolded numbers indicate when Ra values are outliers of flow regime*

Table 4.6 Modified Ra*

		I =	300 W/m^2	500 W/m^2	700 W/m^2
Z (m)	H (m)	D^*_{HZ} (m)	Ra* (×10^8)		
Predictions indicate that flow should be laminar					
0.1	0.1	0.18	0.14	0.20	0.23
0.2	0.1	0.22	0.26	0.36	0.43
0.3	0.1	0.25	0.36	0.50	0.60
0.1	0.2	0.27	0.48	0.66	0.79
Predictions indicate that flow should be turbulent					
0.2	0.2	0.33	0.87	1.21	1.45
0.3	0.2	0.37	1.21	1.68	2.00
0.1	0.3	0.34	0.91	1.27	1.51
0.2	0.3	0.41	1.68	2.33	2.77
0.3	0.3	0.46	2.32	3.22	3.84

4.4. The effectiveness of the solar chimney

Figure 4.7 shows the temperature contours with velocity vectors for varying solar intensity from 300 to 700 W/m^2 for the case with both H and Z = 0.3 m. As expected, the absorber is heated by solar radiation causing the heated air in the chimney to rise and external ambient air to enter through the window. The thermal condition of the room gets warmer with increasing solar intensity and the mean room temperatures are 35.65, 40.29, and 44.65 °C, respectively, which is expected. According to ASHRAE [25], upper limits of acceptable (80% acceptability) and preferable (90% acceptability) indoor temperature are approximately 30 °C and 28.5 °C, respectively, when T_∞ = 27°C. Such high indoor temperature may be due to the location of the window, where only bottom portion of the room are cooled as shown in Figure 4.7. The average temperature of the bottom half of the room is 32.75, 35.31, and 37.72 °C, which is lower but still pretty high considering the ambient temperature. Further investigation on thermal condition will be discussed in Chapter 5. The change in air speed is not noticeable from Figure 4.7, but the ACH in Table 4.3 indicates that

more air flows into the room with increasing solar intensity. Air circulation is noticeable at the bottom corner below the window, and there is hardly any flow present at the top portion of the room, which causes the air temperature to rise. While the thermal condition of the room is hot, mostly due to position of window, acceptable ACH is predicted, where Baker [14] suggested the minimum ACH to maintain indoor quality is 1-2 and to remove heat is 2-15.

Lastly, the effect of H is investigated at $I = 500$ W/m^2 in Figure 4.8, where Z is fixed at 0.2 m and H varies from 0.1 m to 0.3 m. In the previous section, it was determined that the flow is laminar for $Z = 0.2$ m and $H = 0.1$ m (case (d)), and the other cases shown in Figure 4.8 are turbulent flow. The improvement in the thermal condition of the room is noticeable as H changes from 0.1 m (laminar) to 0.2 m (turbulent). As flow changes from laminar to turbulent, the thermal improvement is approximately 7°C, which is due to the increase in ACH comparing cases from (d) to (f) in Table 4.3. Similar flow patterns can be observed for all cases.

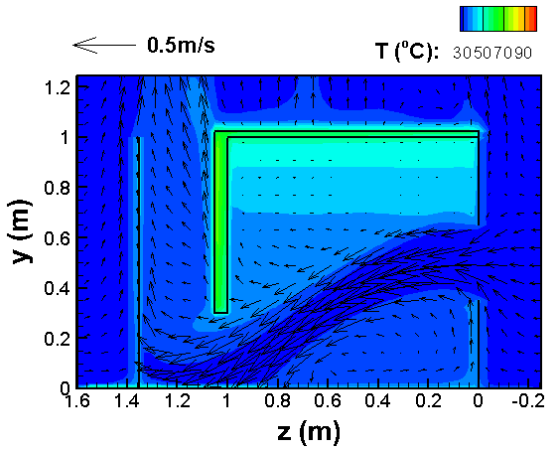

(a) I = 300W/m^2

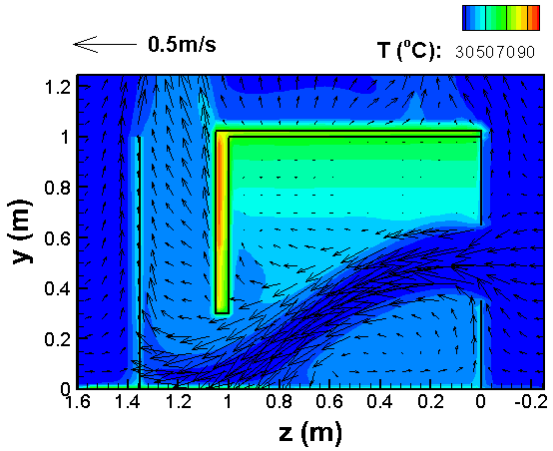

(b) I = 500W/m^2

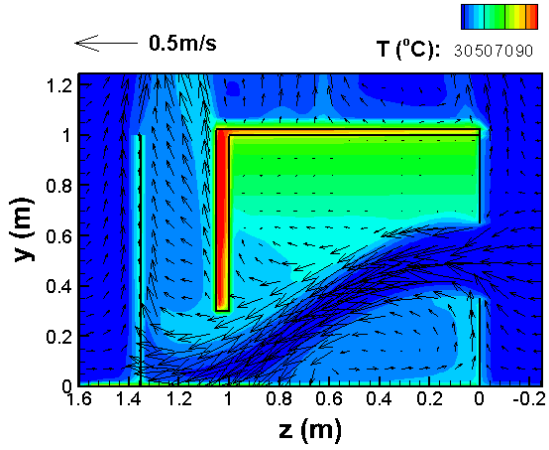

(c) I = 700W/m^2

Figure 4.7 Room temperature with velocity vector for $H = Z = 0.3$ m (a) $I = 300$ W/m^2, (b) $I = 500$ W/m^2, and (c) $I = 700$ W/m^2

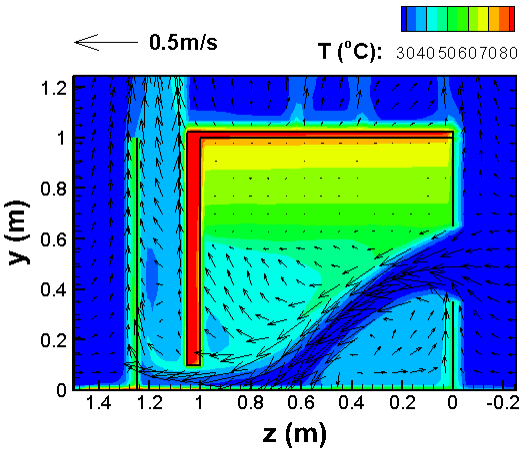

(a) H = 0.1 m (laminar)

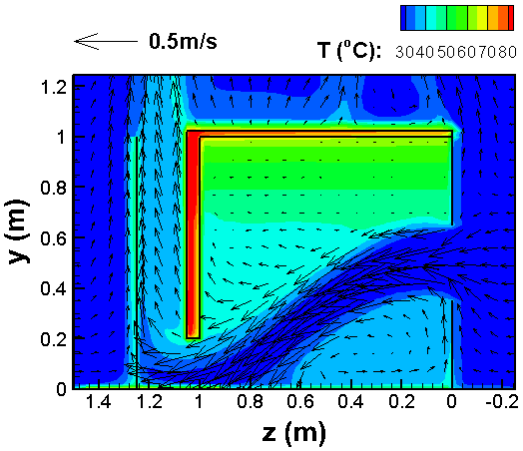

(b) H = 0.2 m (turbulent)

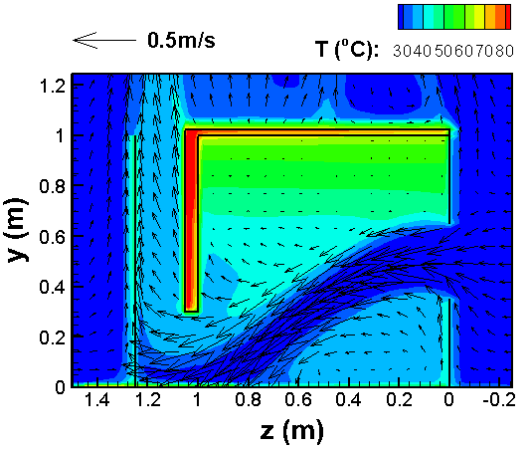

(c) H = 0.3 m (turbulent)

Figure 4.8 Room temperature with velocity vector at 500 W/m^2 with Z = 0.2 m (a) H = 0.1 m , (b) H = 0.2 m, and (c) H = 0.3 m

4.5. Conclusions

The wall-solar chimney system was investigated utilizing computational fluid dynamics. Both laminar and turbulent models were utilized to better understand the flow in the solar chimney system with changes in dimensions of the chimney. ACH for the present study agreed very well with the experiment [15], where the error was 6.62%. Consistent with the literature, ACH improved with increasing solar intensity as well as the air gap. While previous literature has not discussed the effect of the chimney inlet, the current study found that both the chimney inlet and the air gap in a solar chimney system are important to determine the type of the flow, and also that the chimney inlet has a more significant effect on the flow regime compared to the air gap. A new definition for hydraulic diameter was developed using both chimney inlet and air gap and was utilized to calculate Ra*. A clear trend in Ra* with the predicted flow suggested that Ra* can be utilized to define and understand the flow regimens in the wall-solar chimney system. The transition from laminar to turbulent occurred at $Ra^* \sim 0.8 \times 10^8$. Lastly, the flow patterns and the thermal conditions of the room were analyzed by varying the solar intensity and the chimney inlet. The improvement in thermal condition of the room was noticeable with increasing chimney inlet.

Chapter 5. Small and full-scale modeling

5.1. Introduction

The performance of a solar chimney system improves with its size. However, simulating full-scale buildings is often challenging due to its size, which makes small-scale studies more attractive, especially for experimental studies. Mathur et al. [15] conducted an experiment in a small room with a volume of 1 m^3, which is realistically too small for occupants (a typical room size is 27 m^3). While a small-scale model is easier and more convenient to conduct a parametric study, the flow may differ in a full-scale building. Thus, it is important to investigate the relationship between a small- and full-scale model, which will be helpful to predict and understand the flow in a full-scale building using an analysis from a small-scale model.

Previous studies have not focused on finding a clear relationship between small- and full-scale buildings, which can be helpful to predict ventilation in full-scale buildings by utilizing data from small-scale studies. The validated model presented in Chapter 4 is utilized to model the room with a wall-solar chimney to examine different room volumes. Additional volumes of 8, 27, and 64 m^3 are tested to compare the flow and thermal condition with increasing room size.

Window positions and chimney vent openings are investigated to determine whether there is consistency between small-scale and full-scale models. Figure 5.1 (a) and (b) present two room layouts, where the window is positioned at the middle and the top, respectively. Nondimensional parameters are used to develop correlations to better understand the relationship between small- and full-scale models. Lastly, a predictive equation is developed using the nondimensional variables for ventilation in a single room. Random cases are tested to validate the mathematical model by varying room size, ambient condition, window-position, and solar intensity. While it is difficult to predict actual performance of the wall-solar chimney for ventilation in buildings,

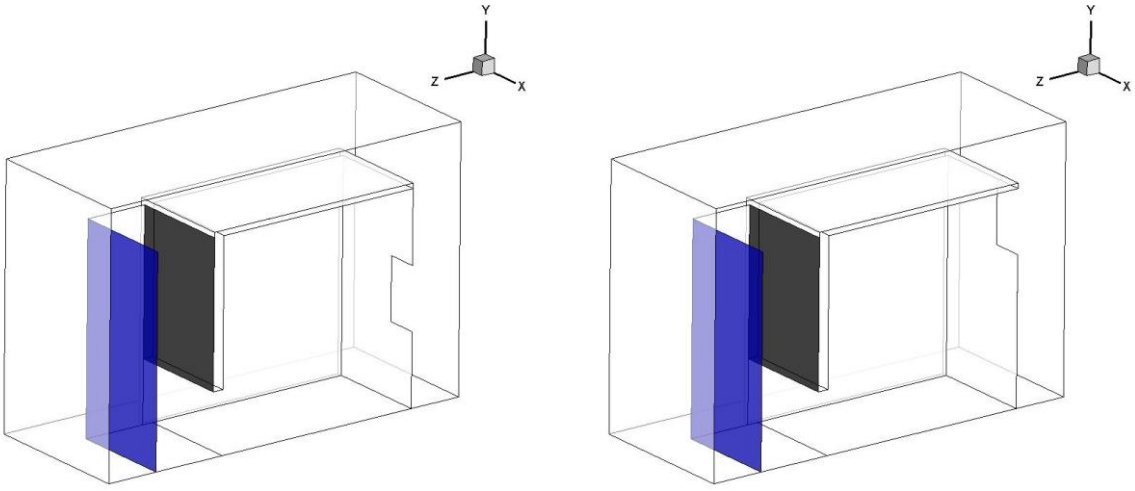

(a) Middle **(b) Top**

Figure 5.1 Two different domains with window positioned at the (a) middle and (b) top

relationships from the current study can be used to estimate ventilation rates in solar chimney systems in larger buildings.

5.2. Boundary conditions

The wall-solar chimney interior features are consistent with conditions shown in section 4.2. Additional dimensions are introduced in Figure 5.2; l_P, the height to the window center, and l_W, the side length of a square window (where $l_W = 0.3L$). The smallest room has a size of 1 m per wall for a volume of 1 m^3. The addition of the wall insulation and chimney increases the chimney-room system by 0.35 m in the z-direction. The computational domain is extended 1/4 beyond the room to represent the ambient environment and also to reduce the effect of boundary conditions on the solutions. For the smallest room, the total domain size is 0.75 m × 1.25 m × 1.85 m in the x-, y-, and z-directions. The chimney vent and air gap are $H = Z = 0.3$ m, and the window is placed on the northern wall with dimensions of 0.3 m × 0.3 m. Two window positions are considered: l_P =

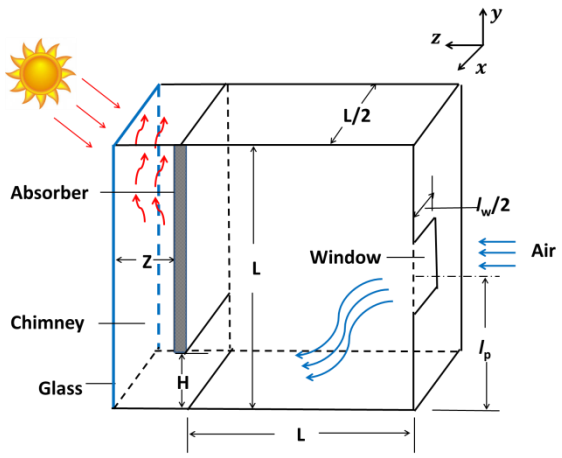

Figure 5.2 Geometry of wall-solar chimney and room with absorber and window positioned at middle of northern wall

0.5 m for the middle-wall position and l_P = 0.85 m for the top-wall position. The absorber plate and glass are facing south, where 5 cm-thick insulation was provided on the backside of the absorber plate prevents direct heat transfer from the chimney to the room.

Four different room volumes are tested: 1, 8, 27, and 64 m^3, where all the rooms are cubical. Increasing the room size in each direction is represented as $d = L_F/Ls$, where L_S is the room length of 1 m and L_F is the length of the larger rooms. The subscripts S and F represent the small-scale and full-scale rooms, respectively. For example, if the room volume increases by 27 times, d = 3 since every dimension increases by 3. Figure 5.3 shows the domains for the small- (1 m^3, black outline) and full- (27 m^3, red outline) scale rooms.

The grid convergence index (GCI) [55] and dimensionless wall distance were calculated in order to determine appropriate grid spacing. Low GCI values of 0.15 % indicated small discretization error (refer to [53] for a complete discussion of the GCI study). Uniform grid spacing

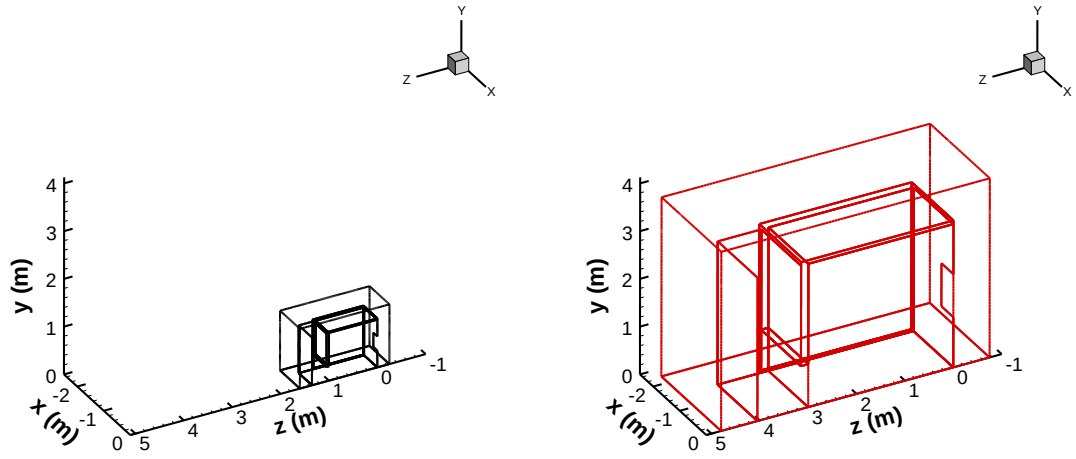

Figure 5.3 Comparison of domain sizes between small (1 m^3, left) and full (27 m^3, right) rooms

of 2 cm is chosen for the room and the chimney for the room with volume of 1 m^3, and the uniform grid spacing of 5 cm is utilized for the ambient conditions.

The ambient conditions at the outermost boundaries are represented by specifying ambient pressure of 1 atm and temperature of 27 °C to be consistent with Mathur et al. [15]. Standard wall functions are used for the turbulence model and the no-slip condition is applied for the fluid-wall interaction. The wall is modeled to consider conduction, convection and radiation heat transfer (refer to [53] for details of radiation properties of the wall material).

5.3. The effect of window-position on thermal condition of the room

Table 5.1 summarizes ACH for twenty-four cases that model four room sizes, three solar intensities and two window positions. The ACH decreases with increasing room volume for both middle- and top-window positions. Overall, ACH is smaller for the cases where the window is positioned at the top of the wall, even in larger rooms. The ACH increases with solar intensity and

Table 5.1 ACH comparisons for middle and top window configurations for varying room size and solar intensity

	V_{room} / I (W/m²)	1 m³	8 m³	27 m³	64 m³
Middle	300	101.7	64.1	47.0	40.4
	500	121.2	76.7	57.9	47.3
	700	136.1	86.5	65.5	53.9
Top	300	70.7	44.1	34.3	27.3
	500	83.1	52.6	40.4	33.4
	700	93.1	57.3	44.9	37.6

the physics will be further discussed in the following section. To determine if there is a relationship between ACH and room size, an average velocity ratio, F, is defined:

$$F = \frac{\bar{v}_F}{\bar{v}_S} \tag{5.1}$$

where $\bar{v}_F$ is the average velocity for a larger room and $\bar{v}_S$ is the average velocity for the 1 m³ room. Figure 5.4 is used to examine the trend for F, and the middle- and top-window cases are distinguished by hollow (blue) and filled (red) symbols, respectively. The trend for F versus d is the same regardless of the window position, suggesting that the average velocity in the full-scale room can be predicted using the correlation shown in Figure 5.4. The correlation between F and d is:

$$F = 0.998 d^{0.34} \approx d^{\frac{1}{3}} \tag{5.2}$$

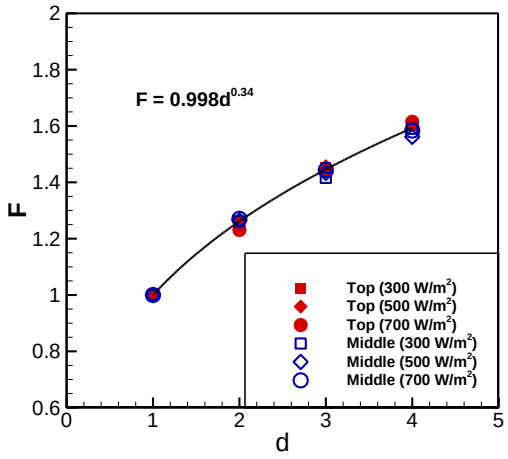

Figure 5.4 Average velocity ratio versus *d* for window position and solar intensity

Eq. (5.2) can be utilized to develop a nondimensional ACH as follows:

$$\frac{ACH_F}{ACH_S} = \frac{\dot{V}_F / \cancel{V}_F}{\dot{V}_S / \cancel{V}_S} = \frac{\bar{v}_F \cdot A_F}{\bar{v}_S \cdot A_S} \cdot \frac{\cancel{V}_S}{\cancel{V}_F} = F \cdot d^2 \cdot d^{-3} \approx d^{-2/3} \qquad (3)$$

where A is the open window area. Equation 4 shows that the ACH in a larger room reduces compared to the small room by a factor of $d^{-2/3}$.

Change in room and absorber temperatures with respect to the size of the room are presented in Figure 5.5 (a) and (b) for varying d, respectively. For each room size and solar intensity, the room temperature is lower when the window is positioned at the top. For a constant solar intensity, the difference between the room temperatures for the middle- and top-window positions decreases as room volume increases, indicating that the effect of window position reduces with larger rooms. Examining Figure 5.5 (b), the absorber temperature decreases with increasing room size and is the same for the middle- and top-window positions, suggesting that the absorber is strongly dependent on the solar radiation. Overall, the absorber temperatures are higher with increasing solar intensity.

However, there is not a clear trend that can be utilized for room temperature predictions with varying d. The room temperature is nondimensionalized and shown in Figure 5.5 (c) to develop a correlation with respect to d:

$$T^* = \frac{T_{room} - T_\infty}{T_{absorber} - T_\infty} \tag{5.4}$$

where subscript ∞ is the ambient condition. A single trend for window position is noticeable in Figure 5.5 (c). The correlation for overall T^* is presented in Figure 5.5 (c), which can approximate

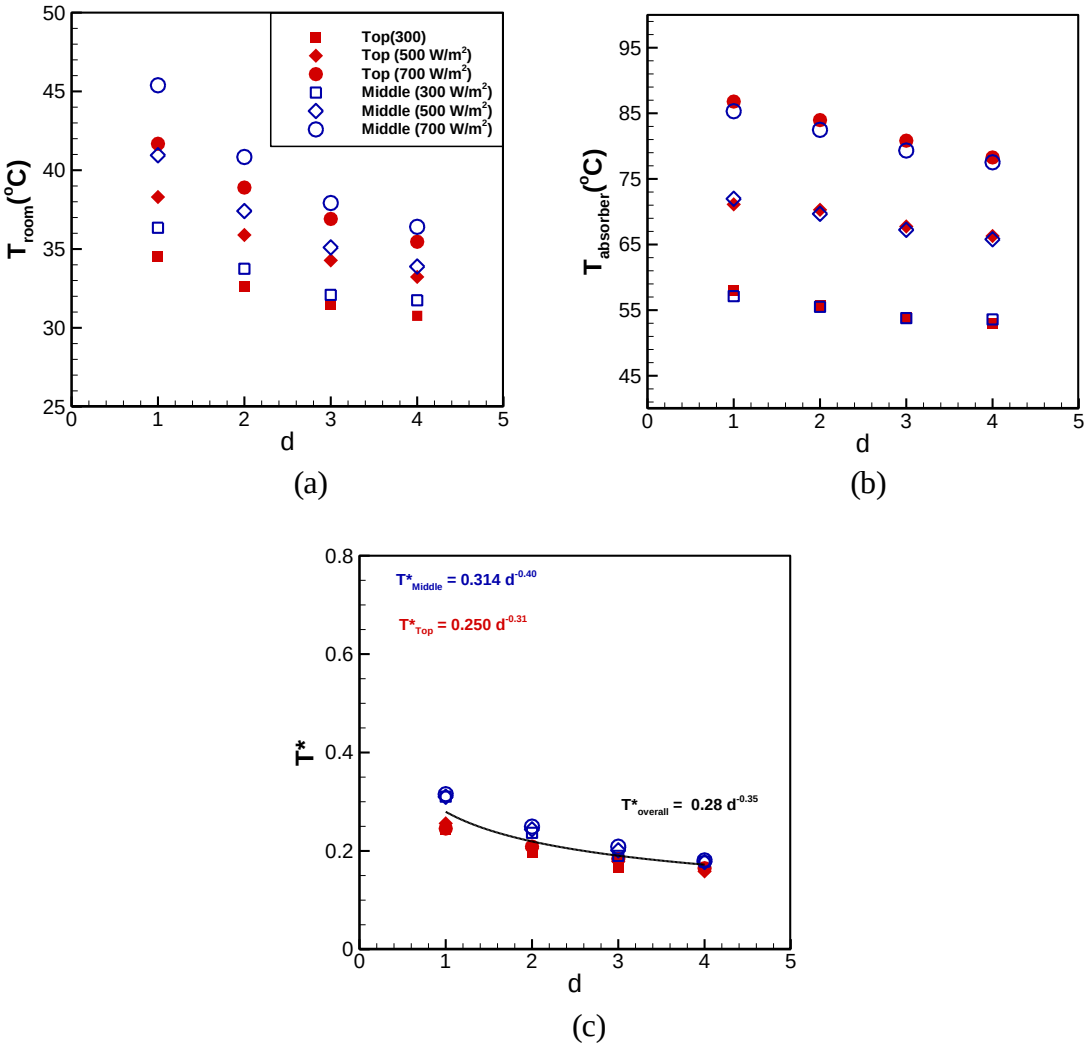

Figure 5.5 Effect of room size *d* on (a) room temperature, (b) absorber temperature, and (c) nondimensional temperature

the room temperature for a window positioned at either the middle or top, where $T^*_{overall} \approx 0.3d^{-1/3}$. The nondimensional temperature is slightly higher for the middle-positioned window due to warmer room temperatures, but it is clear that T^* decreases with increasing room volume.

Figure 5.6 (a) and (b) shows change in room and absorber temperatures with respect to the solar intensity, respectively. Both room and absorber temperature increases with increasing solar intensity. Similar to Figure 5.5 (a), the difference between room temperatures for the middle- and top- window positions decreases as room volume increases for the constant solar intensity in

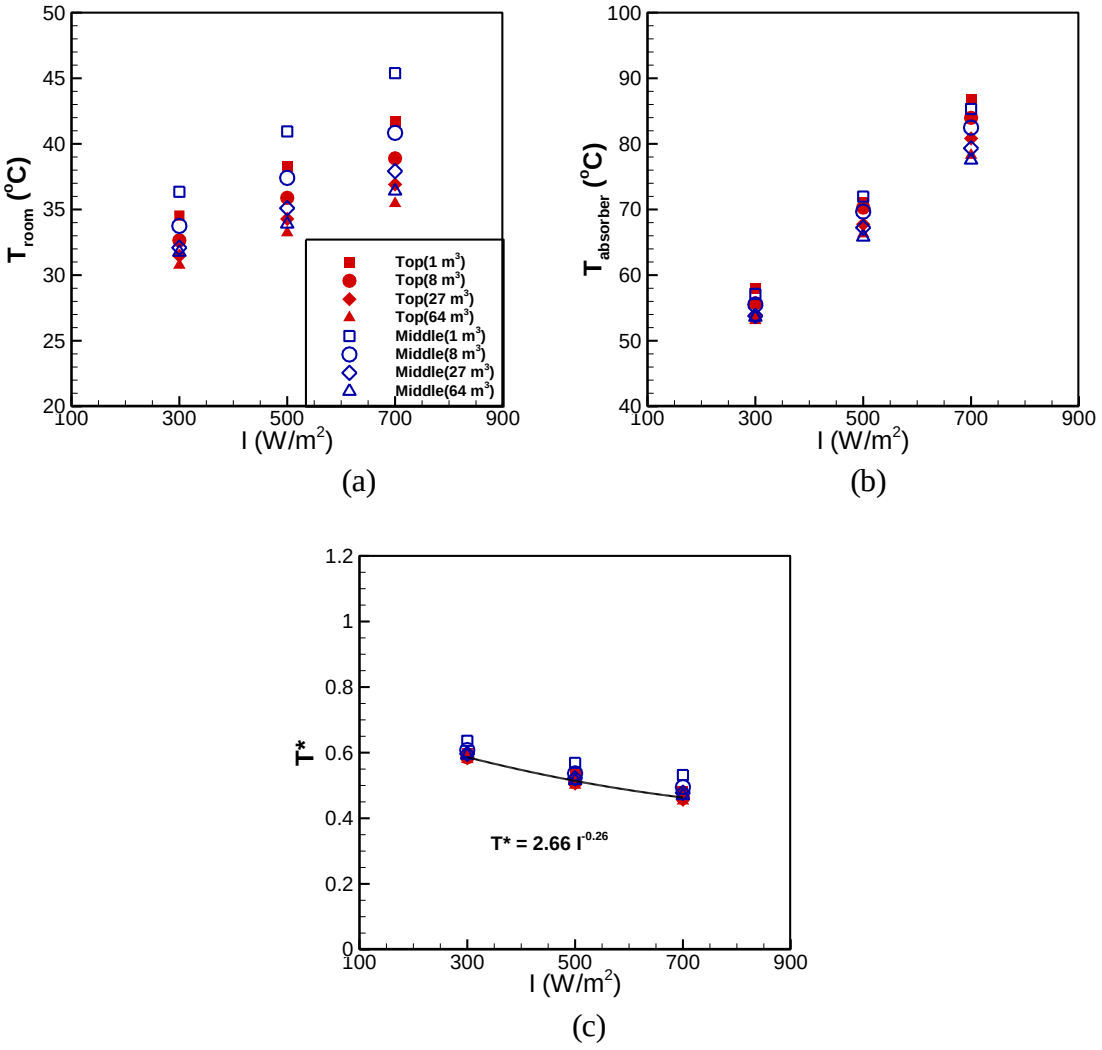

Figure 5.6 Effect of solar intensity *I* on (a) room temperature, (b) absorber temperature, and (c) nondimensional temperature

Figure 5.6 (a). Increase in absorber temperature with respect to solar intensity is consistent regardless of different room size in Figure 5.6 (b). Figure 5.6 (c) shows the nondimensional temperatures for varying I. A decreasing trend is noticeable for T^*, which is due to larger changes in T_{absorber} compared to changes in T_{room} with increasing I. The correlation is shown, where $T^*_{overall} = 2.66d^{-0.26}$.

Velocity (left column) and temperature (right column) contours of a plane at the center of the room are presented in Figure 5.7 (a) and (b), respectively for room volumes of 1 m^3 (top two rows) and 27 m^3 (bottom two rows). The cases in Figure 5.7 show the fields for the top-window and middle-window positions for I = 500 W/m^2. According to Baker [14], the recommended air velocity for thermal comfort is between 0.5–2 m/s. Peak velocity increases from 0.625 to 1 m/s when the room volume increases, which is within the recommended range to maintain thermal comfort. The incoming ambient air velocity is largest with the largest room volume. The cooler room temperatures are also noticeable when increasing the room volume, as shown in Figure 5.7. The temperature contours elucidate that when the window is positioned in the middle of the wall, the air above the window is significantly stratified and ventilation is not effective, despite the larger velocities that occur with larger room sizes. Temperature contours superimposed with streamlines for horizontal planes are shown in Figure 5.8. Three different height locations are chosen 20%, 50%, and 80% of total room height for both top and middle window position and also both room volumes 1 and 27 m^3. The flow patterns are similar between two different volumes for each window position, but cooler condition is observed for the larger room. The incoming air through window is noticeable for both top and middle window cases, which occurs at $L_{80\%}$ and $L_{50\%}$, respectively. Large circulations are present for the middle window cases at $L_{50\%}$ and $L_{80\%}$, whereas streamlines show that the air is fairly well distributed for the top window cases. The fresh air is

not properly distributed throughout the room for the middle window position compared to top window position, resulting in higher temperature difference especially at higher level of the room. Poor air circulations in the room can be also noticed in Figure 5.9, which shows temperature

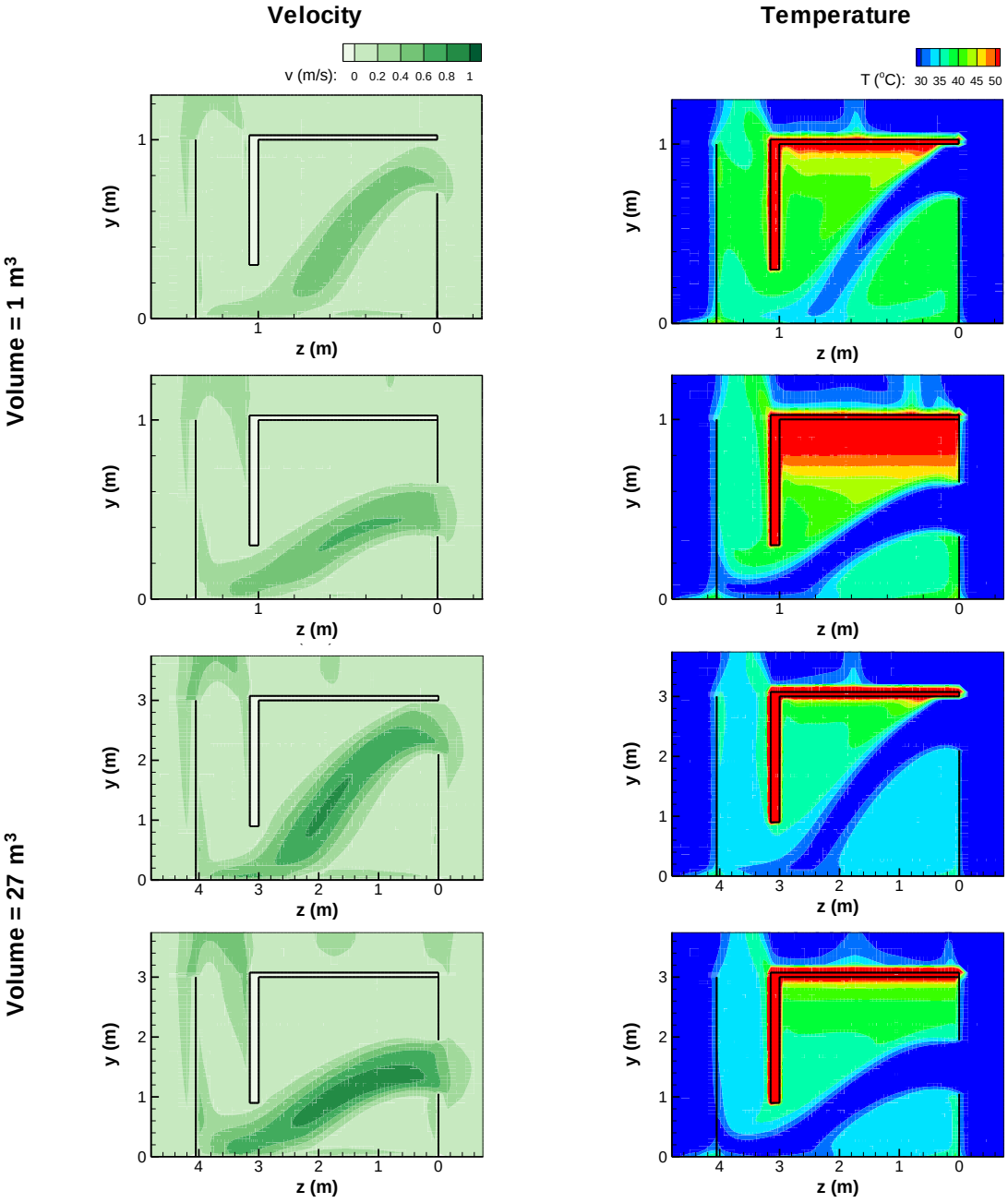

Figure 5.7 Velocity (left) and temperature (right) contours at the room centerplane for room volumes of 1 m³ and 27 m³ for both window positions

streamlines for both window positions. When the window is positioned at the middle, the heated air in the room is not affected by the incoming fresh air. The air in the room is better circulated as window is positioned at the top.

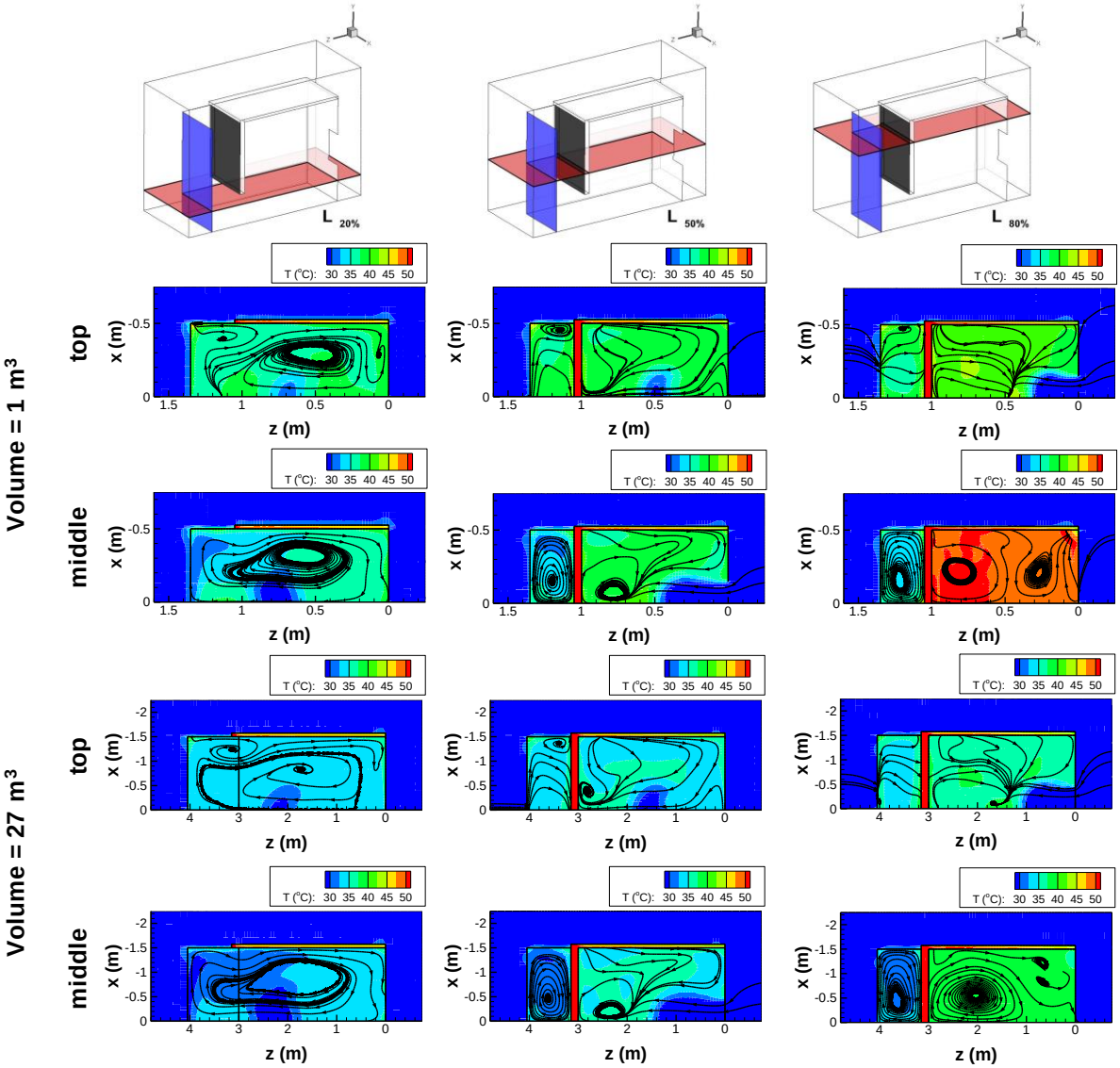

Figure 5.8 Temperature contours superimposed with streamlines at three different heights, $L_{20\%}$, $L_{50\%}$, and $L_{80\%}$, for both window positions

Middle

Top

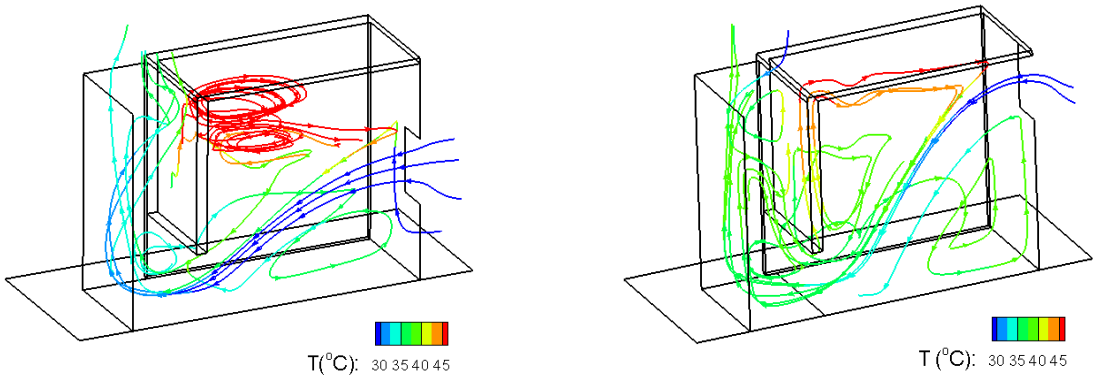

Figure 5.9 Temperature streamlines through the room for middle (left) and top (right) cases

5.4. Regression analysis

In order to further analyze relationships for the flow and geometry, Buckingham pi theorem [56] is employed to nondimensionalize the variables, where π terms are defined. Assuming that the velocity is a function of the other parameters such that $v = f(I, L_S, L_F, l_p, \rho, \mu, H, Z, T_{\text{room}}, T_{\text{absorber}}, T_\infty)$, five nondimensional parameters are developed:

$$\pi_1 = \frac{\rho v L_S}{\mu} = \text{Re} \tag{5.5}$$

$$\pi_2 = \frac{L_F}{L_S} = d \tag{5.6}$$

$$\pi_3 = \frac{l_P}{L_S} \tag{5.7}$$

$$\pi_4 = \frac{\rho^2 I L_S^3}{\mu^3} \tag{5.8}$$

$$\pi_5 = \frac{H}{L_S} \tag{5.9}$$

$$\pi_6 = \frac{Z}{L_S} \tag{5.10}$$

$$\pi_7 = \frac{T_{room} - T_\infty}{T_{absorber} - T_\infty} = T^* \tag{5.11}$$

that form the new relationship $\pi_1 = g(\pi_2, \pi_3, \pi_4, \pi_5, \pi_6, \pi_7)$. The variable π_1 is the Reynolds number (Re), d and T^*were defined in section 3.2, and the other nondimensional parameters are window-position (π_3), solar intensity (π_4), solar chimney inlet (π_5), and air gap (π_6).

Figure 5.10 presents the relationships between π_1 and the other nondimensional variables for the cases with the window positioned at the middle and top of the wall. The symbols denote the solar intensities (300 – 700 W/m^2). The legend is shown in Figure 5.10 (a) for all six parts (a-f), where unfilled and filled symbols indicate window position at middle and top, respectively. Figure 5.10 (b-f) also shows how room volume changes with the other π terms. Increasing Re (i.e., π_1) is noticeable with increasing d (i.e., π_2) shown in Figure 5.10 (a), where Re is larger for the middle-window position. Similarly Re increases with π_3 and π_4 in Figure 5.10 (b) and (c). Since H and Z increase proportionally with d, π_5 and π_6 increase with Re (Figure 5.10 (d) and (e)). Examining Figure 5.10 (f), an inverse relationship between Re and π_5 is shown since T_{room} decreases with increasing velocity, which is due to increasing room size (i.e., d). While data differ by window-position, similar trends can be observed for the two window positions in Figure 5.10 (a-f).

In order to develop a single relationship for π_1 as a function of π_2, π_3, π_4, π_5, π_6, and π_7, regression analysis is applied (using Mathematica), where the following simplified model shows good predictions for the average room velocity π_1:

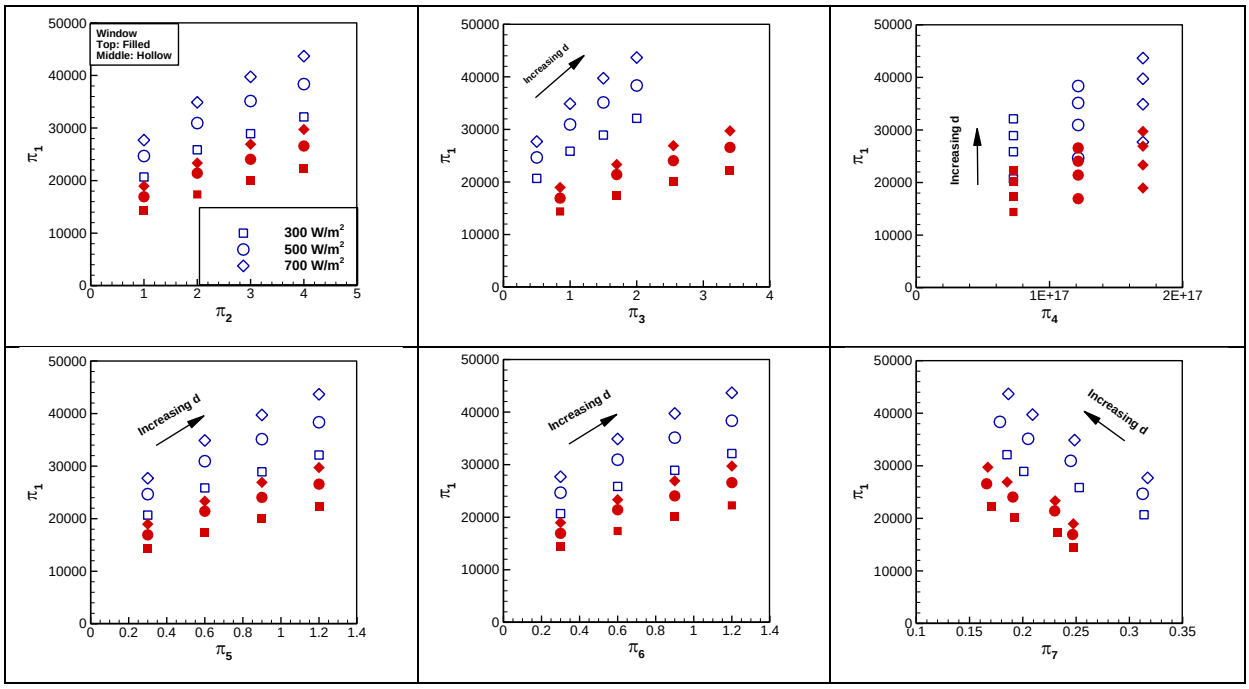

Figure 5.10 Relationship between π_1 and π_2 through π_7 for the window positioned at top (filled, red) and middle (hollow, blue) with solar intensities

$$\pi_1 = C_1 \pi_2^{\alpha} \pi_3^{\beta} \pi_4^{\gamma} \pi_5^{\kappa} \pi_6^{\lambda} \pi_7^{\omega} \tag{5.12}$$

Various cases are utilized to develop the current mathematical model: Table 5.1 (27 cases) and cases (e) to (h) for three different solar intensities (12 cases) reported in [53]. When laminar flows were considered from [53], the mathematical model produced errors as high as 30%. Thus, the current mathematical model is not applicable to laminar flows using the Rayleigh number definition guidelines from [53]. The constants C_1, α, β, γ, χ, λ, and ω are summarized in Table 5.2 based on the regression analysis. Two sets of constants are presented in Table 5.2: Model A considers parameters π_2 through π_7, but can only be utilized when thermal conditions of the room, absorber and ambient temperatures are known. The other model can be utilized without knowing the thermal conditions (Model B).

Table 5.2 Constants for the mathematical model in Eq. (5.12)

	C_1	α	β	γ	χ	λ	ω
Model A (with π_7)	0.0156	0.911	-0.714	0.354	-0.0383	0.165	0.00449
Model B (without π_7)	0.0158	0.911	-0.715	0.354	-0.0386	0.165	0

Average p-values for the constants for Model A are approximately 0.138, where the error for ω is the largest (see Table 5.2 for the constants). The p-value is defined as the probability of obtaining a greater value for the estimating constants. Lower p-values indicate that the prediction of constants have a smaller range for the confidence interval. As thermal conditions are not considered for Model B (ω=0), average p-values for the constants are less than 0.005; therefore Model B will be used for the remaining analyses.

To demonstrate the accuracy of the predictive equation, Figure 5.11 compares the data for π_1 calculated from the simulations and π_1 using predictive Eq.(5.12) and the constants for Model B, where the solid line represents perfect agreement. All of the cases in Table 5.1 are shown in Figure 5.11 and additionally the turbulent cases from [53] are presented. The symbols are very close to the straight line, which indicate that the predicted π_1 is consistent with the simulated π_1 data. The overall relative error using the predicted equation for Model B is compared to the simulations and experiments reported by Mathur et al. [15]. The error is 1.2% using Eq. (13) compared to simulations, and 3.1% compared to the experiments, demonstrating that Eq. (13) is capable of predicting velocity for varying room size, solar intensity, thermal conditions, window-position,

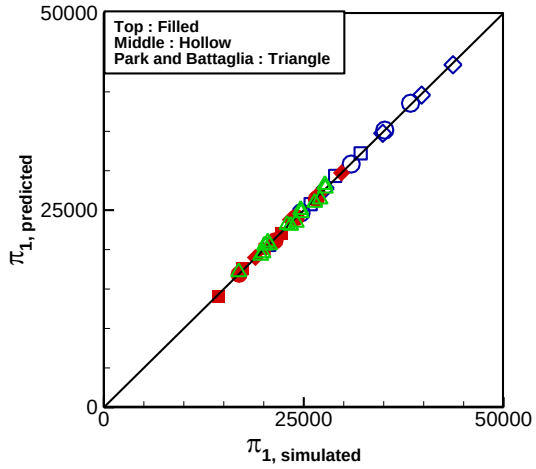

Figure 5.11 Comparison between predicted π_1 using Eq. (5.12) and simulated π_1 for Model B: cases for the window positioned at top (filled, red), middle (hollow, blue), and turbulent cases from [53] (triangle, green)

and *H* and *Z*. It should be noted that some of the experimental data were clearly outliers and those values were not considered in this analysis. Further details related to the experimental uncertainty can be found in [53].

Six random cases are simulated to further test the efficacy of the mathematical model by randomly changing solar intensity, ambient temperature, room size, window position, *H*, and *Z*, where the cases are summarized in Table 5.3. Table 5.4 compares the simulated and predicted velocity using Model B, whereby good agreement is evident with the maximum relative error below 5%. Similar to Figure 5.11, the comparison between simulated π_1 and the predicted π_1 using model B is also visually presented in Figure 5.12 for the cases in Table 5.3, whereby the data are very close to the straight line demonstrating the efficacy of the mathematical model. In summary, the mathematical model can successfully be used to predict the average room velocity as a function of window-position, ambient temperature, room size, solar intensity, *H* and *Z*.

Table 5.3 Summary of random cases to test the mathematical model

	d	*H* (m)	*Z* (m)	l_P (m)	*I* (W/m^3)	T_∞ (°C)
Case 1	1.3	0.26	0.26	0.65	625	26.85
Case 2	1.7	0.51	0.51	0.85	400	16.85
Case 3	3	0.9	0.9	1.5	600	21.85
Case 4	3.2	0.96	0.96	2.4	475	21.85
Case 5	3.3	0.66	0.99	2.34	600	21.85
Case 6	4	1.2	1.2	2.8	500	18

Table 5.4 Comparison between predicted and simulated velocity for Model B using new cases

	Sim. velocity (m/s)	Pred. velocity (m/s)	Relative Error (%)
Case 1	0.432	0.429	0.69
Case 2	0.291	0.288	1.03
Case 3	0.578	0.583	0.87
Case 4	0.420	0.410	2.38
Case 5	0.457	0.474	3.72
Case 6	0.492	0.471	4.27

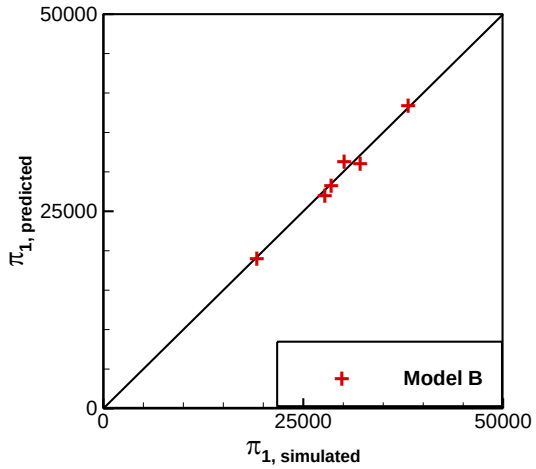

Figure 5.12 Comparison between predicted π_1 using Eq. (5.12) and simulated π_1 for Model B for test cases in Table 3

5.5. Conclusions

A natural ventilation technique based on the wall-solar chimney system was investigated by varying the room volume. The main purpose of the study was to provide a relationship between small- and full-scale models due to the difficulty of conducting studies for full-scale models experimentally and computationally. Variation in the position of the ventilation window, solar chimney design, ambient temperature, and solar intensity were considered to develop a mathematical model.

Four room volumes were examined and an average velocity ratio for full-scale to small-scale model was related to room volume Room temperatures were higher when the window was positioned at the middle of the northern wall despite larger ACH. However, with increasing the room volume, the window location was less significant. Room temperature data were used to find correlations for varying room size and solar intensity, and when the data were nondimensionalized, the curves collapsed irrespective of window position.

Regression analysis was used to develop a relationship between velocity into the room through the window and multiple nondimensional variables. The nondimensional parameters provided more correlations to understand the flow and the relationships between small- and full-scale models. The development of the mathematical model can be used with two sets of constants to create model A and B, where the former and the latter can be utilized with and without knowing thermal conditions, respectively. The predictions of velocity were in very good agreement with the experiments and numerical data from Mathur et al. The predictive equation was applied to random cases for a wall-solar chimney system and it was shown that the equation has a wide range of applicability. The predictive equation can be used to provide an indication of the ventilation velocity and ACH, as well help a user relate small-scale physics to full-scale physics.

Four room volumes were tested for each layout using a solar chimney. An average velocity ratio for a full-scale to a small-scale model F was related to room volume d, where $F = d^{1/3}$ regardless of the room layout. Other relationships such as ACH and volume and mass flow rate can be developed with mathematical modifications from the correlation for the average velocity ratio F. Similar to results in the first section, room temperature was higher as window was positioned at the middle of the northern wall even in larger rooms. However, the difference in room temperature between the middle and the top reduced with increasing the room volume, indicating that the effect of the opening location decreases in larger rooms. As room becomes larger, both room and absorber temperature decreased, which may be due to the increased air velocity. Room temperature was non-dimensionalized to find correlations for varying d and I. A trend for each room layout was noticeable as T^* varied with d, where the difference is due to the position of the window. A correlation for the overall T^* was developed, $T^*_{overall} \approx 0.28 \cdot d^{-1/3}$, which can be utilized to approximate the room temperature when the window position is between middle and top. As T^* varied with I, the data collapsed showing a decreasing trend, which is due to relatively small increase in room temperature compare to that in absorber temperature with increasing solar intensity.

The application of the solar chimney will be considered in larger buildings and the current study can encourage more small-scale models providing its relationship to full-scale models such as average velocity, ACH, and room temperature. In order to extend the current research on the relationship between small- and full-scale models, Buckingham π theorem is suggested to develop additional relationships involving more independent variables.

Chapter 6. Improvement in the performance of solar chimney system

6.1. Introduction

In Chapter 4, a CFD model for the wall-solar chimney system adjacent to a room was validated and compared to the results by Mathur et al. [15]. In Chapter 5, regression analysis was utilized to develop a mathematical formulation to relate multiple variables such as size of the room, ambient condition, and parameters of the solar chimney system. While previous chapters introduced convenient ways to study the wall-solar chimney system, actual performance of the solar chimney system was not discussed. As mentioned in Chapter 1, there are two important factors considering human comfort utilizing natural ventilation, namely air velocity (e.g., ACH) and thermal condition. In the first part of the current chapter, multiple ways to improve the performance of the solar chimney system are discussed by considering simple changes of the system.

The first modification of the system increases the solar chimney height as shown in Figure 6.1. The motivation of adding an extended section for the solar chimney system is to improve ACH by increasing the pressure difference. The applications of the solar chimney system can vary, and usually large buildings such as factories, auditoriums, and gymnasiums require high ACH to properly ventilate and prevent over-heating. The investigation on the effect of an extended solar chimney height on ACH may be useful to improve the performance of the existing solar chimney system, and will be discussed in section 6.2.

The room can be over-heated due to insufficient ACH, poor air circulation, massive heat sources, poor insulation, etc. Despite sufficient air coming into the room for ventilation, the room was over-heated for the room layouts in Chapter 4, especially for the room with the window

positioned at the middle of the wall. Air circulation improved as the window was repositioned to the top, however, the temperature of the room was still as high as 38 °C for the solar intensity of 700 W/m^2 and the room volume of 27 m^3. The second modification of the solar chimney system is shown in Figure 6.2, where a vent above the absorber is considered to improve the thermal condition of the room. The effect of an additional vent in the top portion of the absorber-solar chimney system is analyzed, and the study will emphasize the importance of the additional vent to improve the thermal condition of the building in section 6.3.

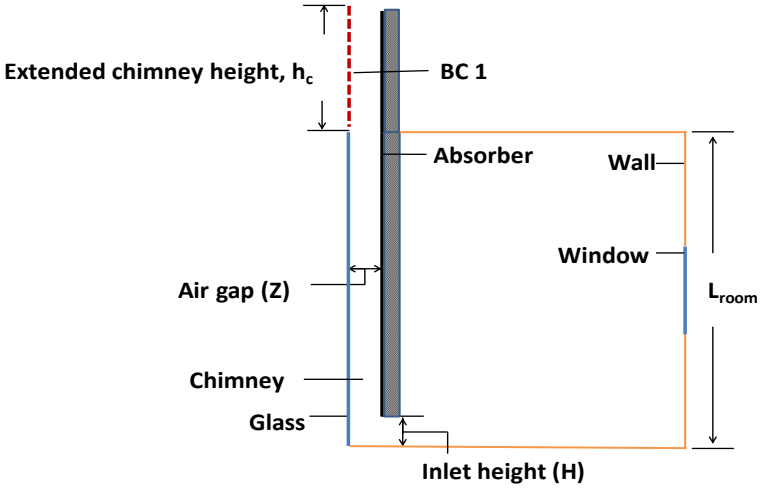

Figure 6.1 Schematic of the geometry for increasing chimney height (h_c)

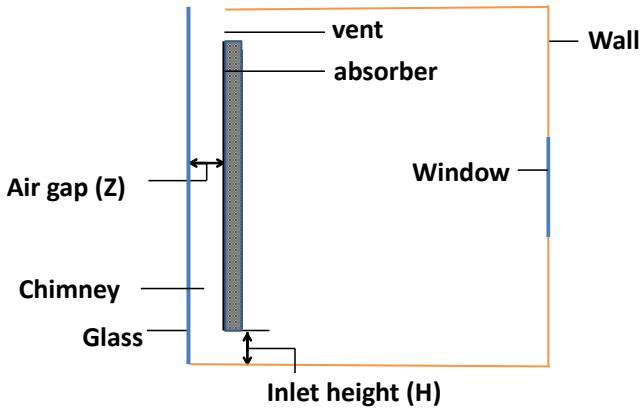

Figure 6.2 Schematic of the geometry with the additional vent above the absorber

In the second part of the chapter, the study explores the effect of multiple factors that may be a concern for implementing the solar chimney system in reality. Chapter 4 and 5 discussed the potential of the solar chimney system on building ventilation, and investigated the effect of different parameters of the solar chimney system by utilizing the conditions that are identical to the one for the experimental study by Mathur et al. [15]. However, the study did not consider realistic conditions and size of the solar chimney system to maintain acceptable air quality in the building, where previous studies showed large ACH and excessive temperatures. The last section investigates a realistic scenario by considering a common room size and the effect of solar radiation through the vent (section 6.4), insulation (section 6.5), and the size of the solar chimney system (section 6.6).

6.2. Design modifications to improve ventilation

6.2.1. Extended solar chimney (improving ACH)

Examining Figure 6.1, the extended section above the glass is represented with a red dashed line labeled BC_1. Two surface conditions, glass and a solid wall, are tested prior to investigating the effect of the extended section of the solar chimney system. Glass is transparent allowing light to pass through whereas the solid wall is opaque, blocking the light. The objective is to determine whether the surfaces used for the extended section are significant toward improving ACH. The room has a volume of 27 m^3 where the solar chimney is extended by 20% of the total height of the room. The same solar intensity is applied from the outside of the domain, and a 3D view of the absorbed solar intensity ($I_{absorbed}$) for two different surface conditions of BC_1, glass (left) and solid wall (right), are compared in Figure 6.3. The middle section of the absorber is not affected by solar intensity when the extended section is a solid wall (blue section of the absorber) because the region is blocked by the extended chimney section.

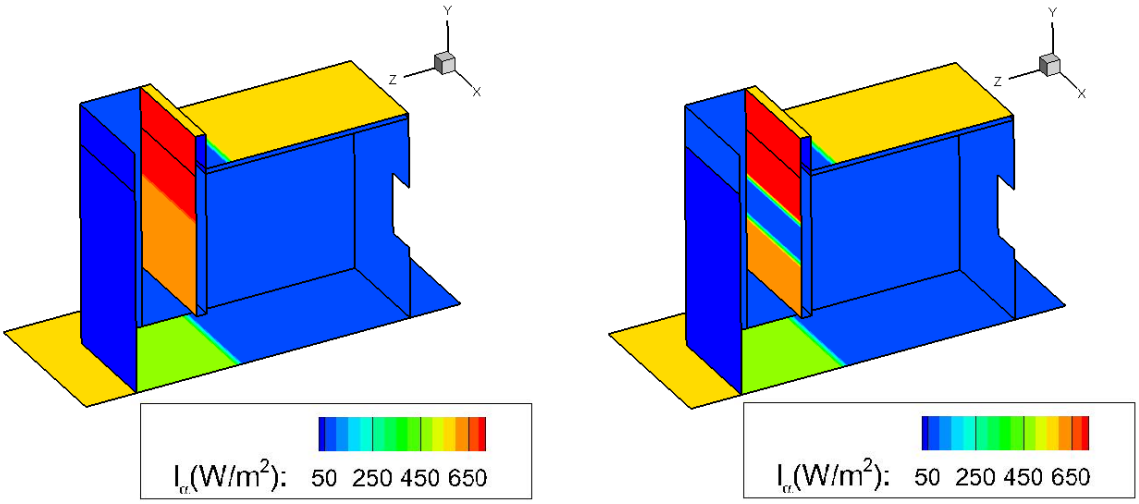

Glass Solid wall

Figure 6.3 Absorbed solar intensity for two different surface conditions: Glass (left) and Solid wall (right)

Table 6.1 compares results for the original case (no chimney extension) and 20% increase in chimney height utilizing the two different surface conditions for BC_1. The absorbed solar intensity (W/m^2) decreases as the extended section is considered since the change in area is relatively larger compared to the solar energy absorbed by the absorber. The absorbed solar intensity further decreases for the extended section represented as the solid wall because it blocks the incoming solar radiation while the glass transmits the solar radiation. ACH increases regardless of the surface condition, however, the ACH difference between the two surface conditions is insignificant despite the difference in $I_{absorbed}$. The results indicate that ACH is not affected by the surface condition

Table 6.1 Comparison between two boundary conditions for BC_1

	Original	20% increase in chimney height	
BC_1		**Glass**	**Solid wall**
$I_{absorbed}$ (W/m^2)	700	673	555
ACH	65.51	74.59	73.56
T_{room} (°C)	37.9	38.2	37.66
$T_{absorber}$ (°C)	79.64	76.2	71.1

used for the extended section, but it is rather due to extended section of the solar chimney. Room temperature is relatively consistent despite the change in chimney height and surface conditions.

Various heights of the solar chimney system are considered, where the solar chimney is extended by 10 – 50% of L_{room} with an interval of 10%. A new parameter r_c is introduced to be a ratio of total solar chimney height ($h_c + L_{Room}$) to room height (L_{Room}). For instance, $r_c = 1.2$ represents 20% increase in solar chimney height. Glass is utilized for the extend section of the solar chimney.

Figure 6.4 shows the effect of r_c on ACH (left ordinate) and temperature (right ordinate). First, examining the changes in ACH, the largest improvement occurs when r_c changes from 1 to 1.1. ACH shows a linear relationship with r_c after $r_c = 1.1$, which is represented by the red dashed line. Examining temperatures, a steady decrease in $T_{absorber}$ is noticeable with increasing r_c. T_{room} is relatively constant despite increasing ACH, which can be explained by examining velocity and temperature contours for different heights of the chimney in Figure 6.5. Increasing velocity in the crossflow is noticeable with increasing r_c. However, the crossflow only affects the bottom portion of the room, forming a recirculation zone near the ceiling (refer to results in section 5.3 for the

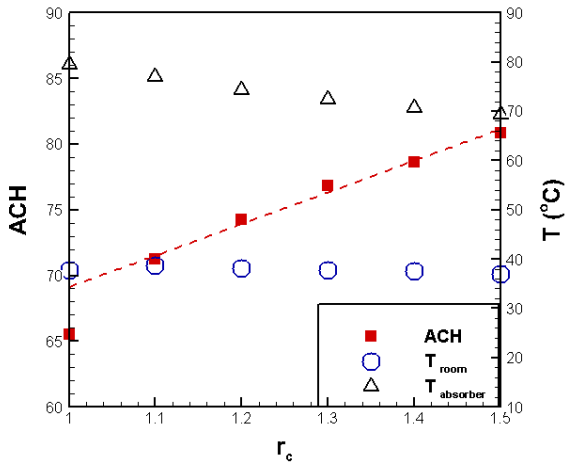

Figure 6.4 The effect of r_c on ACH and temeprature (room and absorber)

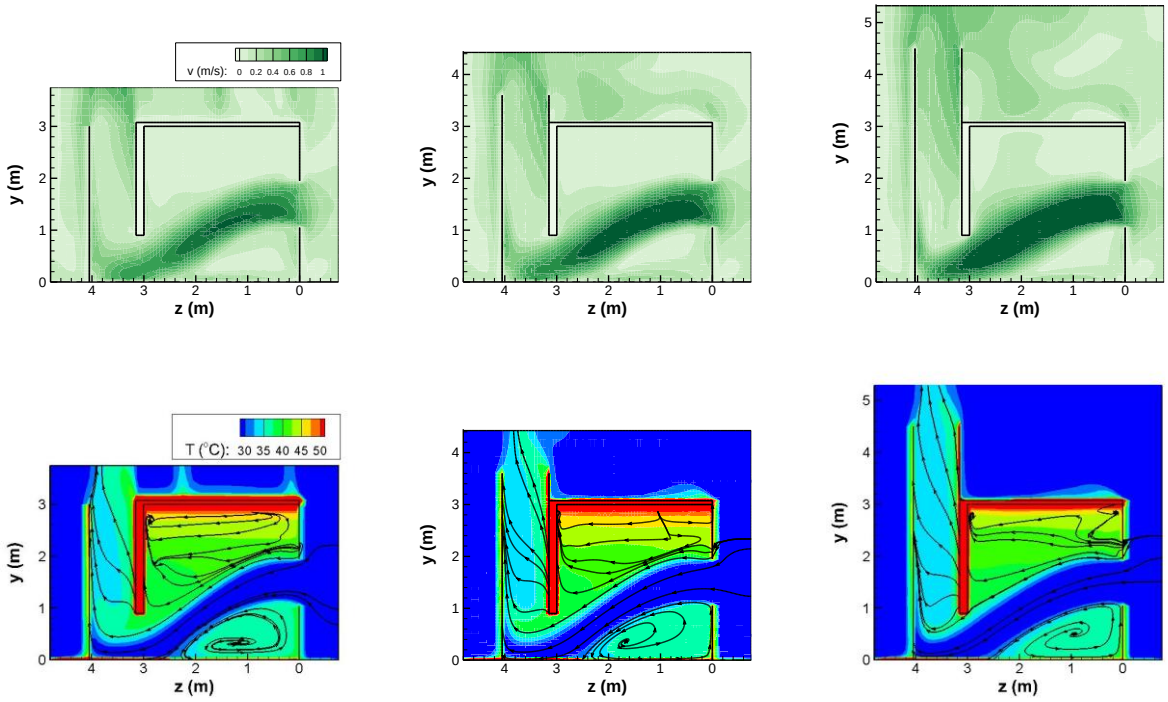

(a) r_c = 1 **(b) 1.2** **(c) 1.5**

Figure 6.5 Velcoity and temeprature contours superimposed with streamlines for r_c = (a) 1, (b) 1.2, and (c) 1.5

effect of window position). In summary, the extended chimney section improves ACH, however, a better design needs to be considered for better ventilation. The next section discusses a way to improve the thermal condition of the room.

6.2.2. Additional vent (improving thermal condition)

The effect of an additional vent in the top portion of the absorber wall is analyzed here. Vent heights of 15 cm, 30 cm, and 45 cm in a room with a volume of 27 m^3 are tested. The additional vent will be labeled as upper vent ($Vent_U$), and what was originally denoted as chimney inlet (H) will be lower vent ($Vent_L$). The lower vent is fixed at 90 cm and the extended solar chimney is not considered for this analysis.

Figure 6.6 compares velocity and temperature contours for various $Vent_U$, which can be compared to the original room in Figure 6.5 (a). The velocity magnitude of the primary flow (from window through the lower vent) is not significantly affected by the size change of the upper vent. Recirculation was noticeable in the top portion of the room for the original room, that is the case without the upper vent, and therefore the room was over-heating (refer to Figure 6.5). Examining streamlines in Figure 6.6, the upper vent improves the air circulation by allowing warm stale air to evacuate, and thus decreases room temperature. However, the overall thermal condition is relatively constant despite the size change in the upper vent in Figure 6.6.

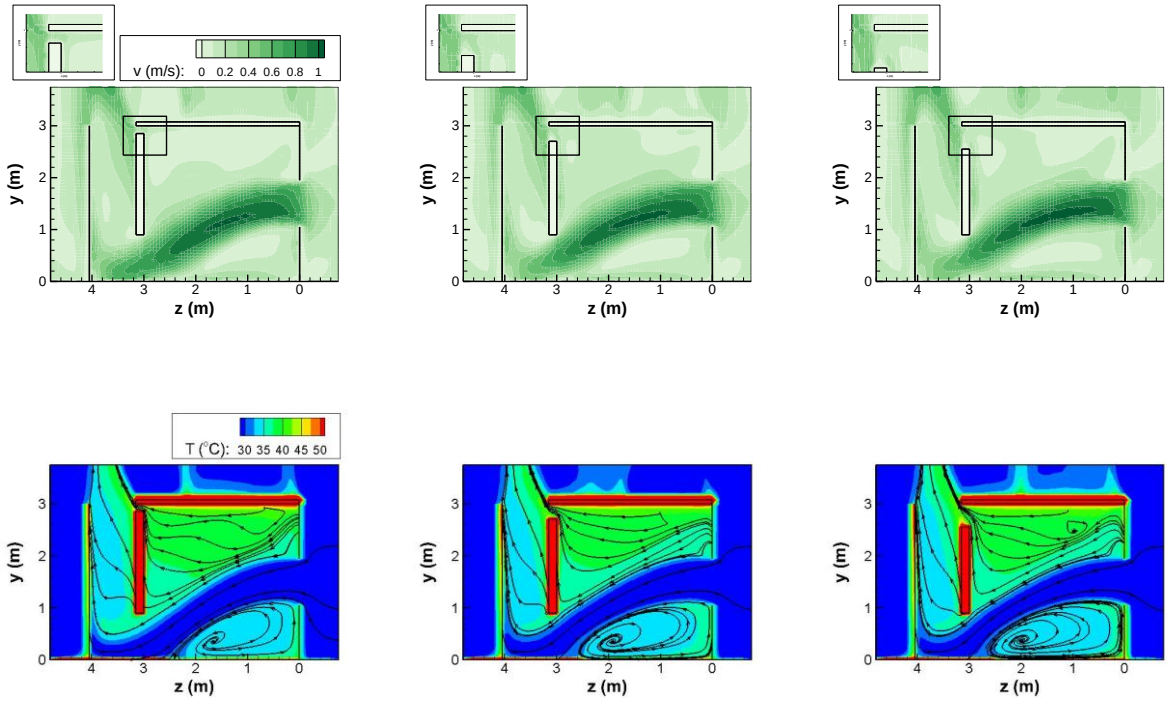

(a) 15 cm **(b) 30 cm** **(c) 45 cm**

Figure 6.6 Velocity and temperature contours for cases with additional vent of (a) 15 cm, (b) 30 cm, and (c) 45 cm

Figure 6.7 shows temperature contours superimposed with streamlines for three different horizontal planes (0.2, 0.5, and 0.97 L_{Room}) for upper vent heights from 0 to 45 cm, from top to bottom in Figure 6.7, respectively. Higher temperatures are noticeable close to the room ceiling (0.97 L_{Room}) since warm air arises. Comparing cases without and with the upper vents,

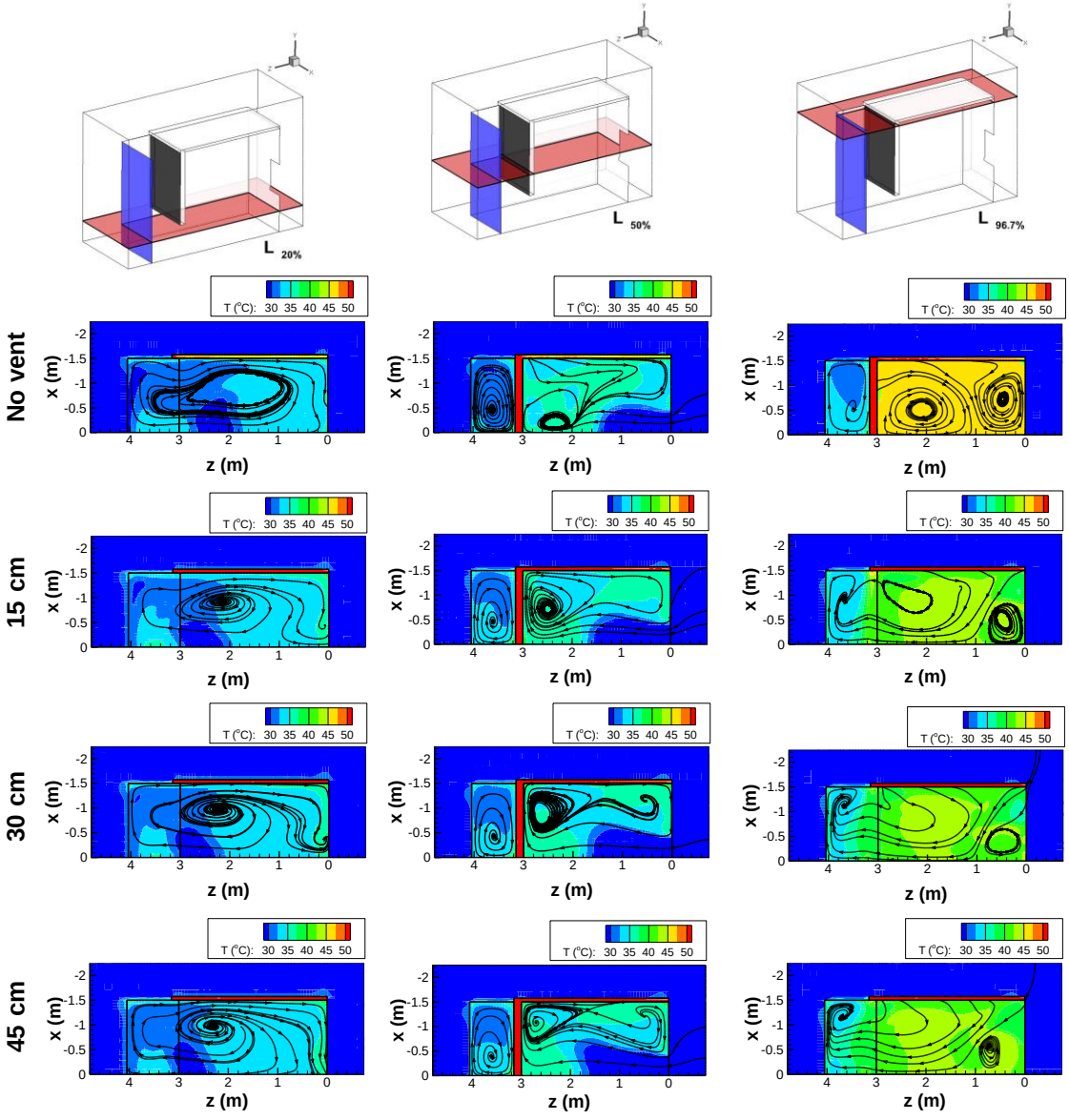

Figure 6.7 Temperature contours superimposed with streamlines at three different heights, $L_{20\%}$, $L_{50\%}$, and $L_{96.7\%}$, for no vent (top), 15 cm vent (middle), and 30cm vent (bottom)

Table 6.2 Summary of mass flow rate through lower and upper vent, ACH_{total}, and T_{room}

	No vent	15 cm	30 cm	45 cm
$\dot{m}_{Vent_L}$	0.58	0.44	0.41	0.39
$\dot{m}_{Vent_U}$	0	0.14	0.18	0.21
ACH_{total}	65.08	64.97	66.37	68.85
T_{room} (°C)	37.88	35.55	35.44	35.07

temperatures are similar for the bottom half of the room (0.2 L_{Room} and 0.5 L_{Room}) because the primary flow is not affected. The effect of the upper vent is noticeable near the ceiling (0.97 L_{Room}) where temperatures are higher for the case without the upper vent. Recirculation is present near the ceiling without the upper vent (analogous to a closed vent) whereas the upper vent allows the heated air to leave the room. However, the size of the upper vent does not significantly affect the flow patterns and temperature distribution.

Table 6.2 summarizes mass flow rate through lower and upper vents ($\dot{m}_{Vent}$), ACH_{total}, and room temperature. Mass flow rate through the lower vent ($\dot{m}_{Vent_L}$) decreases with increasing size of the upper vents while mass flow rate through the upper vent ($\dot{m}_{Vent_U}$) increases. However, the change in mass flow rate is small with increasing size of the upper vent. The overall change in ACH_{total} is relatively small despite the size change of the upper vents, indicating that the upper vent does not reduce the ventilation rate. The overall performance of the solar chimney to draw fresh air is relatively unaffected, regardless of the presence of the upper vent since the solar chimney size does not change. The room temperatures decrease approximately by 2°C with the upper vent. However, the upper vent plays an important role for the crossflow, improving both air circulation and thermal conditions.

The room temperature is relatively constant despite the size change in the upper vents, and can be explained by examining the absorbed solar intensity of the building for different upper vent

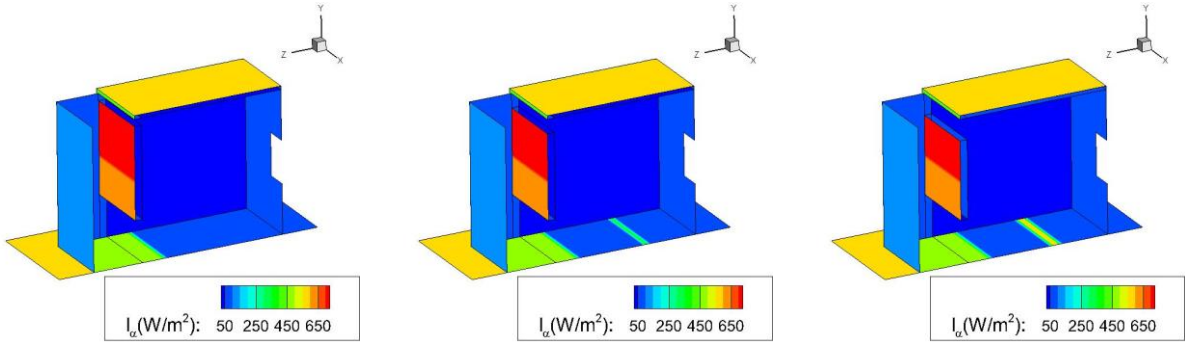

(a) (b) (c)

Figure 6.8 Absorbed solar intensity in the system for $Vent_U$ = (a) 15 cm (b) 30 cm and (c) 45 cm

sizes in Figure 6.8. Focusing on the room floor, the area of the green region increases for larger upper vent sizes, indicating that the solar radiation enters through the upper vent and affects the inside of the room. While increasing size of the upper vent exhaust more warm air from the room, it also allows more solar radiation into the space providing unnecessary heat to the building. Realistically, the solar radiation through the vent will be limited or prevented by a screen or a cover. More realistic modeling is considered in the later section, where the absorptivity of the room floor is disregarded to assume that there is no solar radiation entering through the vents in the solar chimney system.

6.3. The effect of $Vent_L$

In section 6.2.2, the lower vent size ($Vent_L$) was fixed at 90 cm while the upper vent size ($Vent_U$) increased from 0 to 45 cm with a room volume of 27 m^3. In this section, the interest is to investigate the effect of $Vent_L$ on room temperature and overall ACH with the presence of the upper vent. The effect of lower vent and air gap (Z) on ACH was investigated in section 4.3, however, the effect of lower vent on room thermal conditions was not extensively investigated since the main purpose was to validate the computational model with experiments. Additionally, 90 cm is approximately

1/3 of the L_{room}, which may be too large in real applications. The question is whether increasing the size of the $Vent_L$ has any impact on ventilation of the building, which this study explores to find a reasonable size of the lower vent.

Three lower vents are compared ranging in height from 30 cm to 90 cm with an interval of 30 cm, where the upper vent also varies from 0 to 45 cm with an interval of 15 cm for the room volume of 27 m^3. The simulation still assumes that the solar radiation enters through the vents and affects the inside of the building. The first two rows of Figure 6.9 show velocity and temperature

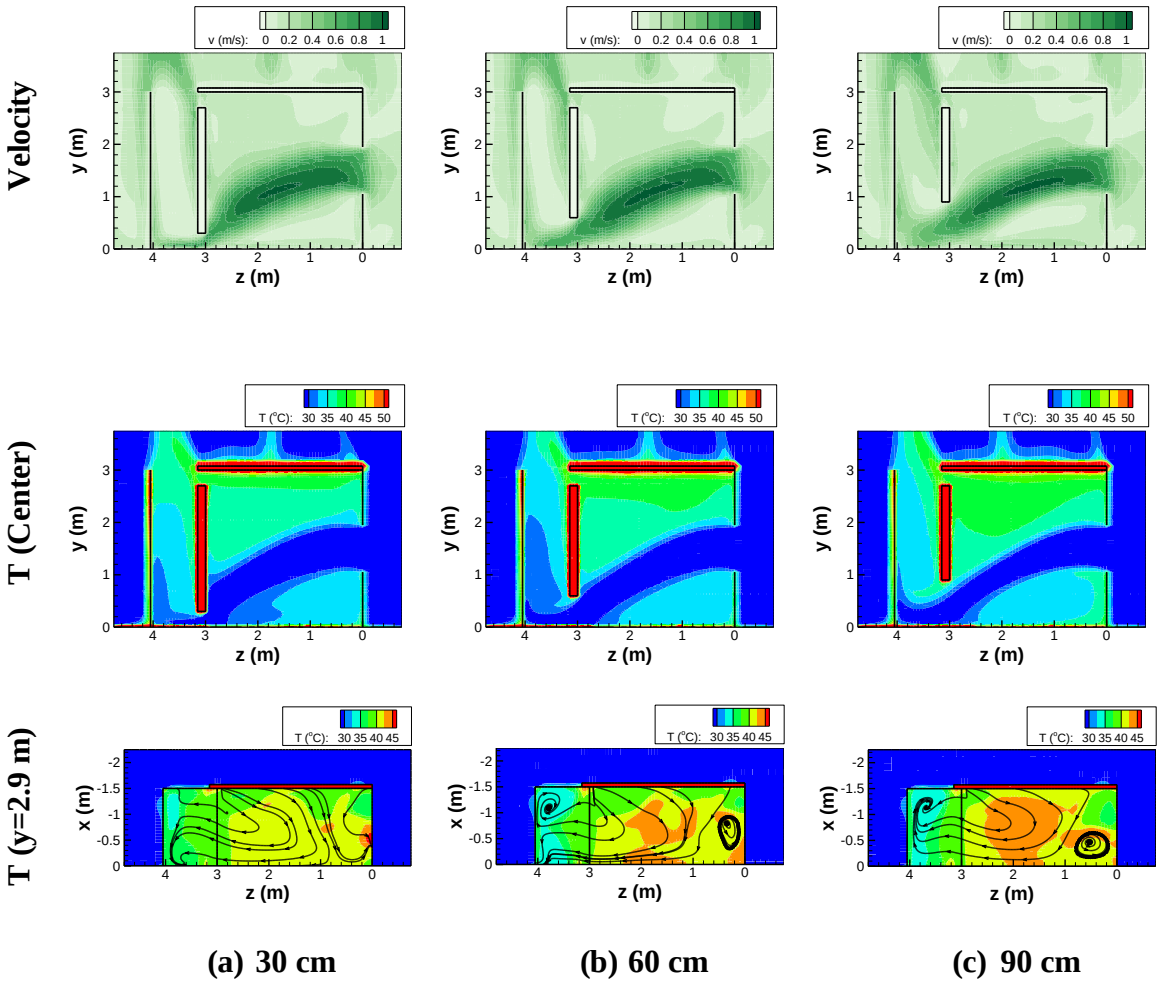

Figure 6.9 Velocity and temperature contours for cases with additional vent of (a) 15 cm, (b) 30 cm, and (c) 45 cm

contours at the center of the room for various $Vent_L$ for a fixed $Vent_U$ = 30 cm. Difference in velocity is insignificant, where the flow patterns and peak velocity look similar regardless of $Vent_L$. The room gets warmer with increasing $Vent_L$, especially the upper portion of the room. Physically, the main flow into the window impinges the absorber for the smallest lower vent size, creating a larger region of cool air in the room. With increasing $Vent_L$, the main crossflow is not disrupted as it flows into the chimney. The last row of Figure 6.9 presents temperature contours superimposed with streamlines on a plane near the ceiling (y = 2.9 m) to examine the effect of $Vent_L$, where the plane cuts through the upper vent. The increase in temperature is more obvious near the ceiling, especially when $Vent_L$ = 90 cm. A recirculation zone forms with increasing $Vent_L$ on the right size of the plane, which is close to the window (inlet), restricting better airflow throughout the room.

Figure 6.10 (a)-(c) show plots of $\dot{m}_{Vent_L}$, $\dot{m}_{Vent_U}$, and ACH_{total} for different sizes of the upper vent with varying $Vent_L$, respectively. Examining Figure 6.10 (a), mass flow rate through the lower vent overlaps for the cases with the upper vents ($Vent_U$ = 15 – 45 cm), which is overall smaller compared to the case without the upper vent ($Vent_U$ = 0 cm). The mass flow rate through the lower vent is relatively constant despite the change in $Vent_L$ and irrespective of the upper vent. Examining Figure 6.10 (b), mass flow rate through the upper vent is overall greater for larger $Vent_U$ increasing the area to allow more warm air to escape (notice $\dot{m}_{Vent_U}$ is equal to 0 for $Vent_U$ = 0 cm). Interestingly, $\dot{m}_{Vent_U}$ increases or decreases depending on the size of $Vent_U$: $\dot{m}_{Vent_U}$ decreases for $Vent_U$ = 15 cm, is constant for $Vent_U$ = 30cm, and increases for $Vent_U$ = 45 cm. The reason may be due to the effect of solar intensity on the room floor with the change in $Vent_U$ as shown in Figure 6.8. While no solar radiation enters when $Vent_U$ = 15 cm, the solar radiation affects more area on the room floor as $Vent_U$ increases to 30 cm and 45 cm, which creates an additional

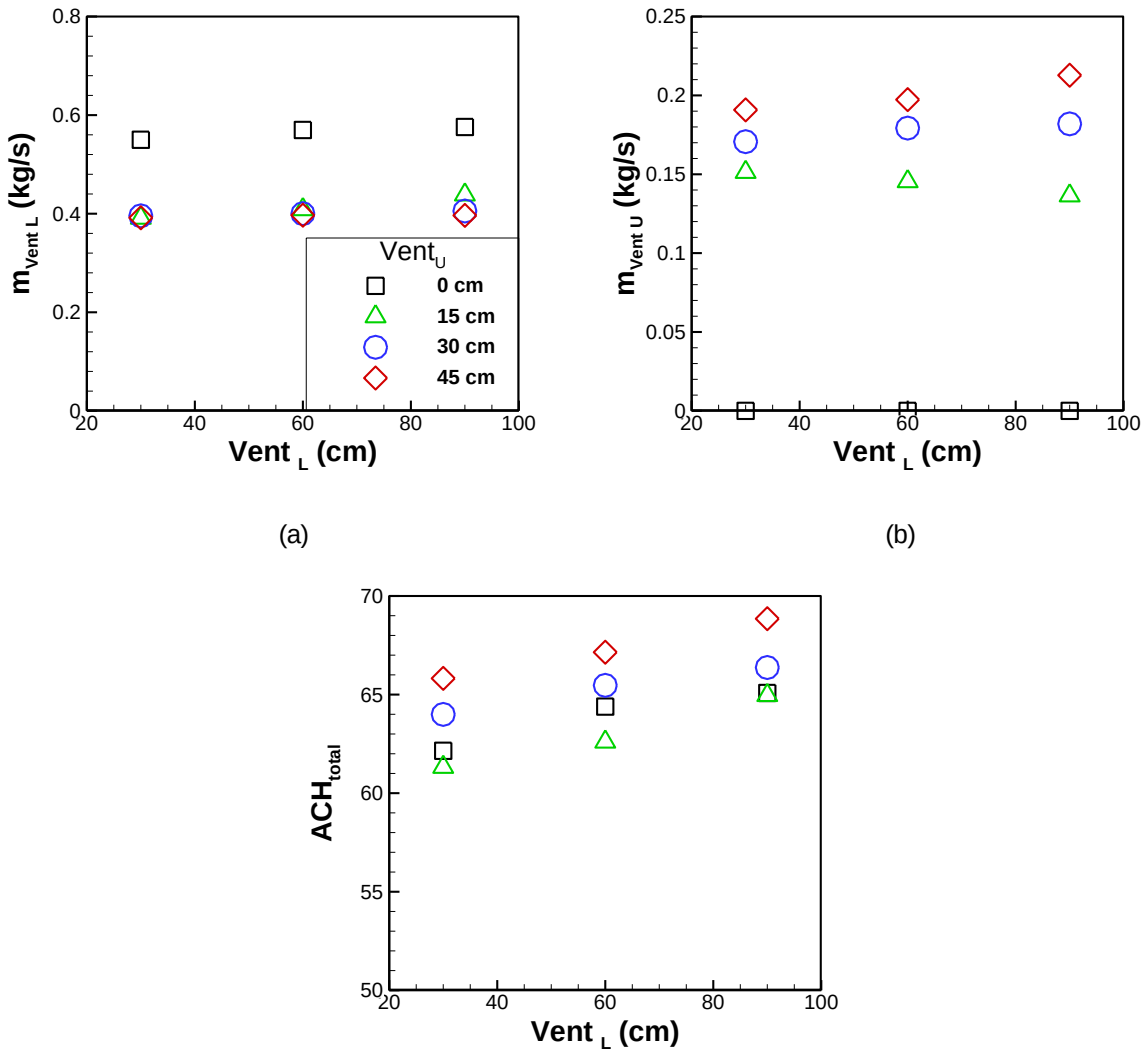

Figure 6.10 The effect of $Vent_L$ on (a) $\dot{m}_{Vent_L}$, (b) $\dot{m}_{Vent_U}$, and (c) ACH_{total}

heat source in the room. In Figure 6.10 (c), ACH_{total} is overall larger for larger $Vent_U$ except a slight drop is noticeable when the upper vent is considered (from $Vent_U = 0$ to 15 cm). ACH_{total} shows an increasing trend with increasing $Vent_L$ for all $Vent_U$.

Figure 6.11 (a) and (b) show plots of average temperatures at the lower and upper vents, respectively, and (c) shows room temperature for different sizes of the upper vent with varying $Vent_L$. Examining Figure 6.11 (a), temperature is overall higher for the case without the upper vent

($Vent_U$ = 0 cm) since the lower vent is the only vent for the warm air to escape. Air temperature at the upper vent is higher compared to the lower vent (Figure 6.11(a-b)) because the warmer air leaves the room through the upper vent. Temperatures at both vents are relatively constant with varying the lower vent size.

Examining Figure 6.11 (c), the change in room temperature due to the lower vent is different for the cases with and without the upper vent. In the absence of the upper vent, the T_{room} decreases

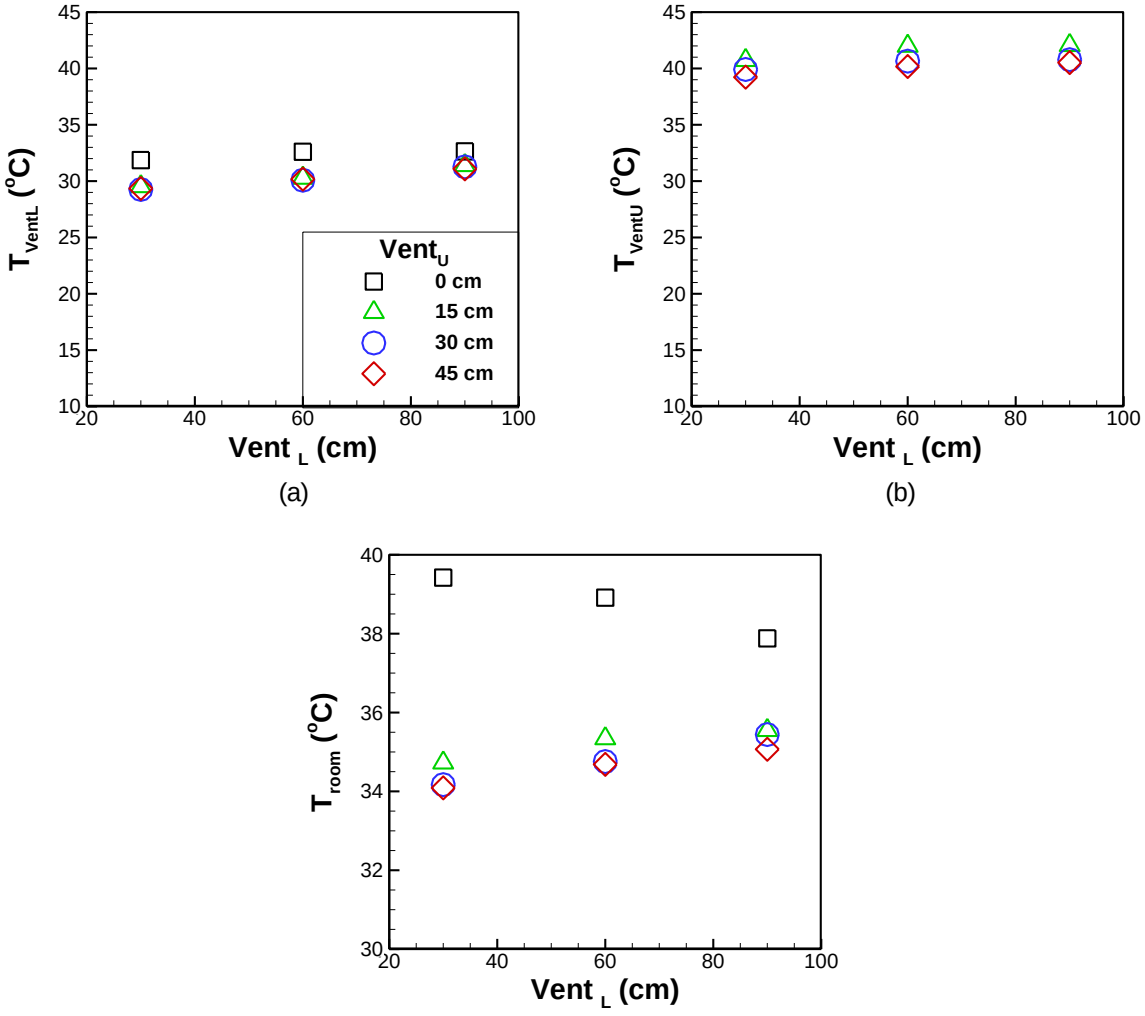

Figure 6.11 Effect of $Vent_L$ on average temperature of air entering through vents, (a) lower and (b) upper vents, and (c) room temperature

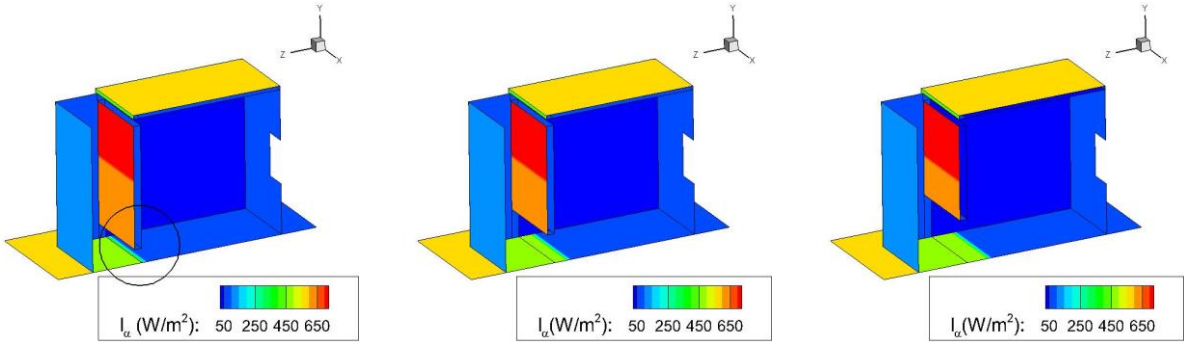

(a) 30 cm (b) 60 cm (c) 90 cm

Figure 6.12 Absorbed solar intensity on the room for *vent* = 15 cm (a) *H* = 30 cm, (b) 60 cm, and (c) 90 cm

with increasing $Vent_{\mathrm{L}}$. However, T_{room} increases when the upper vent is included. An increasing trend of room temperature for the cases with the upper vent is a similar logic as increasing room temperature with increasing $Vent_{\mathrm{U}}$ in section 6.2. Figure 6.12 shows the effect of solar radiation on the building for varying $Vent_{\mathrm{L}}$ with a fixed $Vent_U$ = 15 cm. Differences are noticeable at the room floor (a circled region in (a)), where the green region increases with increasing $Vent_{\mathrm{L}}$. More area in the room is affected by the solar radiation with increasing size of the lower vent, and thus room temperature increases. Considering the case without the upper vent, only the lower vent exhausts the air from the room. More warm air leaves the room as the size of the lower vent increases, and thus room temperature decreases. The conclusion reached by this study is that the upper vent serves the purpose of improving air circulation to exhaust warm stale air near the ceiling.

6.4. Disregard solar absorptivity on room floor

Sections 6.2.2 and 6.3 showed that increasing $Vent_U$ and $Vent_L$ increases the area on the room floor affected by the solar radiation. In reality, the solar radiation through the vents would be minimized or not affect the room floor if a screen or reflective cover is placed over the vent to mitigate the solar radiation. In this section, the absorptivity of the room floor (α_{floor}) is neglected to assume that there is no solar radiation through either the upper or the lower vents, whereas previous cases considered α_{floor} to be 0.5. The effect of the lower and the upper vents sizes on the ventilation rate and the thermal condition is re-evaluated for $\alpha_{floor} = 0$, and the results are compared to $\alpha_{floor} = 0.5$. The difference between allowing solar radiation ($\alpha_{floor} = 0.5$) and blocking solar radiation ($\alpha_{floor} = 0$) through vents is shown by comparing the absorbed solar intensity on the building in Figure 6.13. The green region on the room floor represents the area affected by the solar radiation entering through vents in the system with $\alpha_{floor} = 0.5$. When $\alpha_{floor} = 0$, the room floor is not affected by the solar radiation through the vents and appears as a blue region.

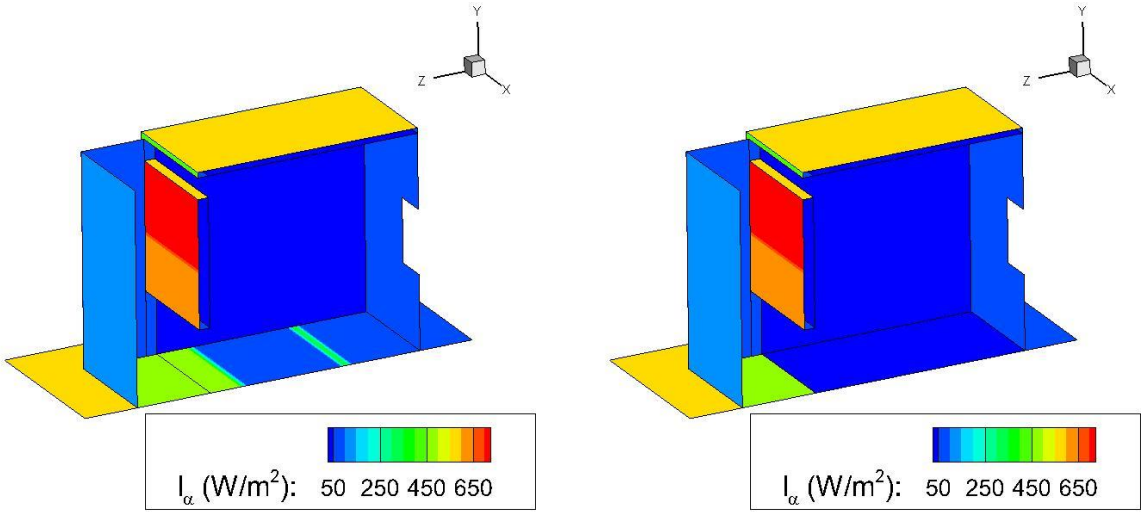

$\alpha_{floor} = 0.5$ $\alpha_{floor} = 0$

Figure 6.13 Absorbed solar intenstiy for the consideration of $\alpha_{floor} = 0.5$ (left) and $\alpha_{floor} = 0$ (right) on the floor

Figure 6.14 investigates the effect of the lower vent on mass flow rates through the lower and upper vents, ACH_{totoal}, and T_{room} for α_{floor} = 0 and 0.5. $Vent_L$ varies from 30 cm to 90 cm and $Vent_U$ is fixed at 15 cm. Examining Figure 6.14 (a) and (b), mass flow rates through the lower vent increase while mass flow rates through the upper vent decrease with increasing $Vent_L$ regardless of α_{floor}. However, the relative change in mass flow rates with respect to $Vent_L$ is smaller as α_{floor}

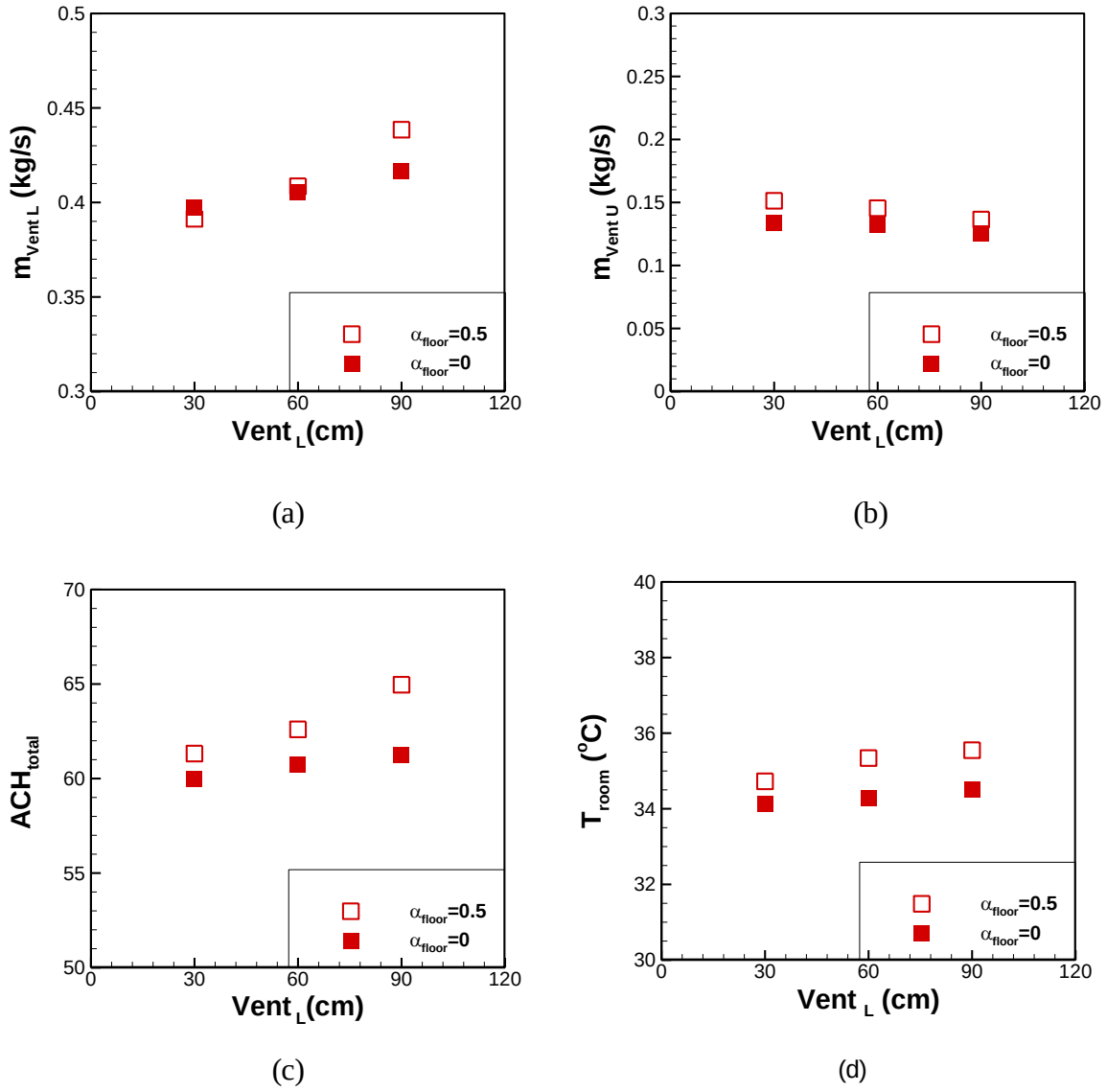

Figure 6.14 The effect of $Vent_L$ on mass flow rates through (a) lower and (b) upper vents, (c) ACH, and (d) room temperature for the cases with and without α_{floor}

= 0. Similarly examining Figure 6.14 (c) and (d), the relative change in ACH and room temperature is smaller when $\alpha_{floor} = 0$ compared to $\alpha_{floor} = 0.5$. Overall ACH and room temperature are lower for the case without α_{floor} due to less absorbed solar energy inside of the building. As solar radiation was allowed through the vents in the solar chimney system in section 6.3, the effect of $Vent_L$ on the solution was obvious and smaller $Vent_L$ was recommended to improve thermal condition of the room. However, the change in ACH_{total} and T_{room} with respect to $Vent_L$ is insignificant when $\alpha_{floor} = 0$, showing almost constant values. The result indicates that the effect of $Vent_L$ on the room condition in section 6.3 was due to the amount of the solar energy affecting the room floor, not due to the change in $Vent_L$. Larger $Vent_L$ allowed more solar radiation into the room, which contributed toward increasing both ACH and thermal condition of the room when $\alpha_{floor} = 0.5$.

Figure 6.15 presents the effect of the upper vent sizes on mass flow rates through the lower and upper vents, ACH_{totoal}, and T_{room} for $\alpha_{floor} = 0$ and 0.5. The $Vent_U$ varies from 0 to 45 cm and $Vent_L$ is fixed at 90 cm. Examining Figure 6.15 (a), mass flow rate through the lower vent steadily decreases until the upper vent size reaches 30 cm and is relatively constant after $Vent_U = 30$ cm regardless of α_{floor}. Examining Figure 6.15 (b), $\dot{m}_{Vent_U}$ steadily increases with increasing $Vent_U$ for $\alpha_{floor} = 0.5$, however, $\dot{m}_{Vent_U}$ is constant after $Vent_U = 30$ cm for $\alpha_{floor} = 0$. ACH slightly decreases as $Vent_U$ increases from 0 cm to 15 cm regardless of α_{floor}. ACH steadily improves with increasing $Vent_U$ for $\alpha_{floor} = 0.5$ from $Vent_U = 15$ cm to 45 cm, however, ACH is constant after $Vent_U = 30$ cm for $\alpha_{floor} = 0$, similar to the changes in mass flow rates. Examining Figure 6.15 (d), room temperature is relatively constant after $Vent_U = 15$ cm regardless of α_{floor}. The result suggests that the upper vent does not need to be larger than 30 cm, $1/10^{th}$ of L_{room}, to exhaust warm air from the room when a screen is considered at the vents to block solar radiation into the room.

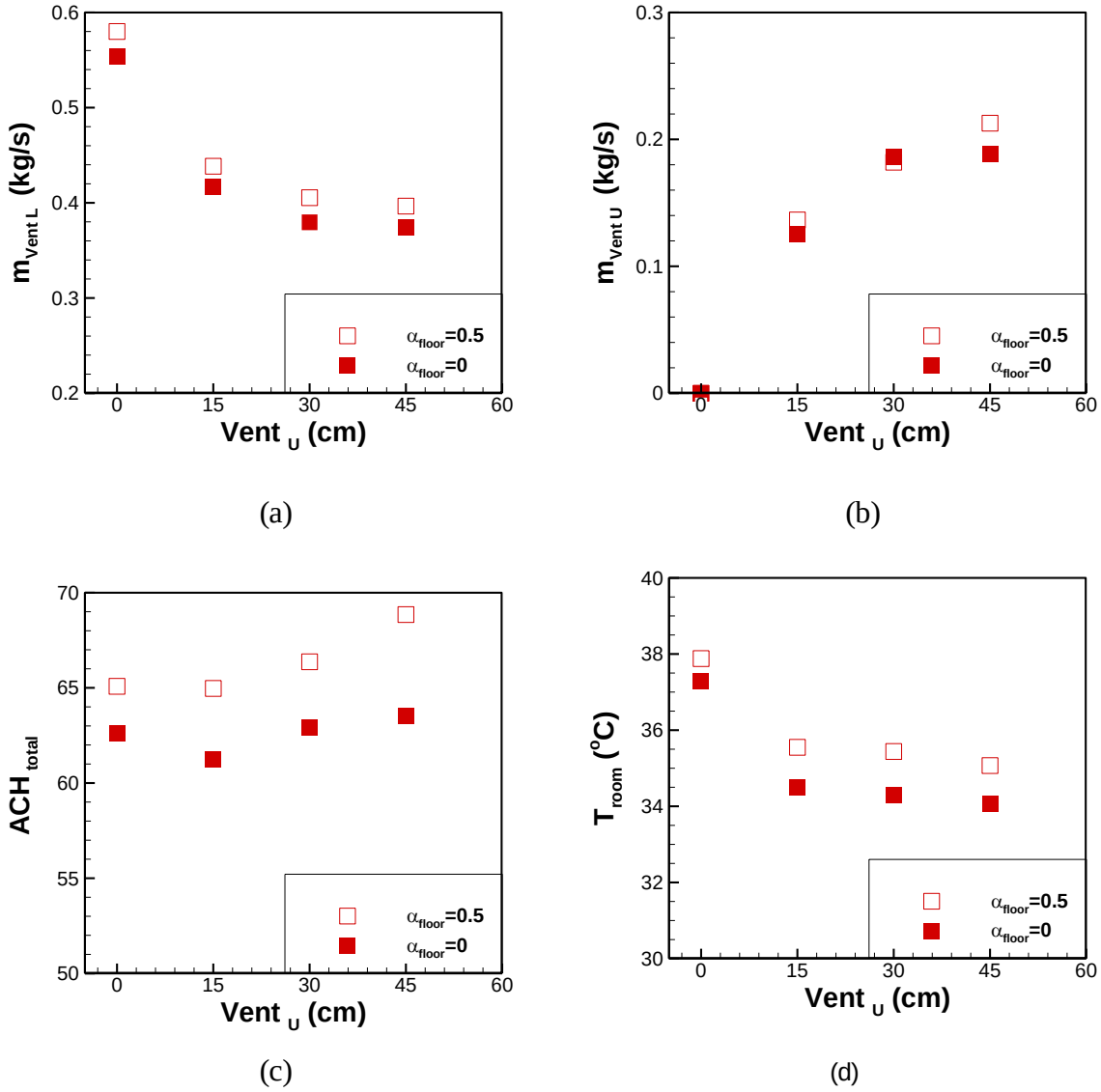

Figure 6.15 The effect of upper vent on mass flow rates through (a) lower and (b) upper vents, (c) ACH, and (d) room temperature for the cases with and without α_{floor}

6.5. The effect of insulation

In the previous sections, wall conditions were modeled identical to Mathur et al. [15], where conduction was allowed through the wall behind the absorber. The room temperature was close to 40°C, which improved to 35°C with the upper vent (section 6.2.2), however, the temperature is still above recommended thermal comfort levels. The issues for overheating in the room despite

the high ACH include poor air circulation, solar radiation absorbed by the room floor, and lack of insulation, especially the wall behind the absorber. The former two factors were discussed in sections 5.3, 6.2.2 and 6.4. The absorber temperature reached approximately 80 °C due to the absorbed solar energy, thus the insulation is an important consideration for the solar chimney system to prevent excessive heat transfer from the absorber to the room. The effect of better insulation is investigated in this section, where the wall behind the absorber is considered adiabatic by assuming no heat transfer from the chimney to the room. A building volume of 64 m^3 is utilized with an upper vent of 40 cm and lower vent of 80 cm are utilized, and solar absorptivity of the room floor is neglected inside of the building.

Figure 6.16 compares velocity and temperature contours with streamlines for the cases with non-adiabatic and adiabatic walls. The airflow patterns in the rooms are similar, where the flow through the lower vent is dominant compared to the flow through the upper vent. When the walls are adiabatic, the peak velocity in the crossflow gets smaller. Improvement in overall thermal condition of the room is noticeable, especially near the ceiling, where the region of highest temperatures is smaller.

The two cases are compared in Table 6.3 by computing mass flow rates through the upper and lower vents, ACH, and room temperature. The immediate difference occurs in mass flow rate through the upper vent because the backside of the absorber is well insulated (adiabatic). Mass flow rate through the lower vent also increases for the adiabatic wall condition. While the amount of heat absorbed by the absorber is constant for both cases, some heat is transferred from the solar chimney to the room by conduction when the backside of the absorber is poorly insulated. The additional heat transfer from the chimney to the room warms the air in the room, and thus the upper vent is more functional (larger mass flow rate) for the case with the poor insulation. When the

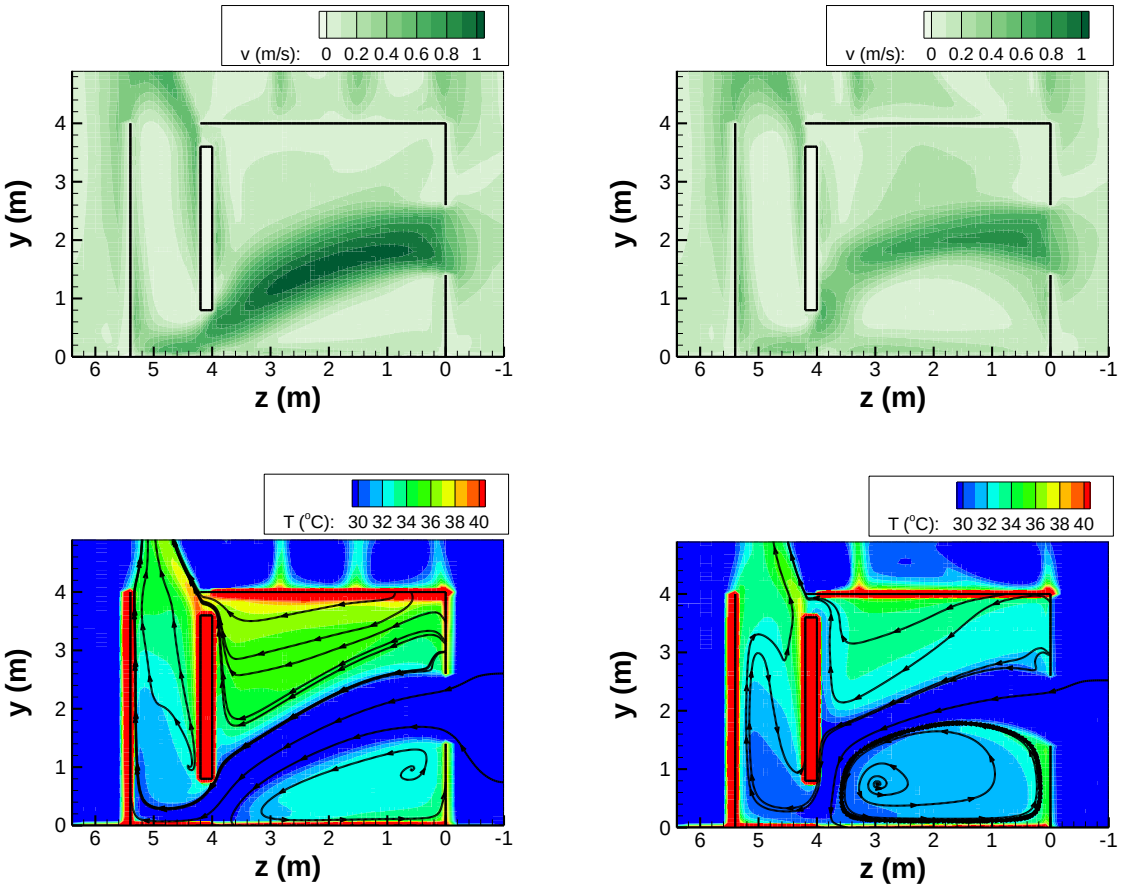

(a) Non-adiabatic (b) Adiabatic

Figure 6.16 Velocity (top) and temperature (bottom) contours for (a) non-adiabatic and (b) adiabatic walls

walls are well-insulated, there is less heat transferred to the room, and thus mass flow rate through the upper vent decreases. The well-insulated absorber radiates more energy to the air within the solar chimney and increases mass flow rates through the lower vent. ACH decreases when the room is well insulated, which may be due to a smaller temperature difference between the room

Table 6.3 Comparison in mass flow rate through vents, ACH_{total}, and T_{room} for non-adiabatic and adiabatic cases

Walls	$\dot{m}_{Vent_U}$ (kg/s)	$\dot{m}_{Vent_L}$ (kg/s)	ACH_{total}	T_{room} (°C)
Non-Adiabatic	0.268	0.843	52.9	33.7
Adiabatic	0.086	0.905	46.2	30.8

and the ambient environment, however, the ACH is still very large. Room temperature improves by 3°C with better insulation.

6.6. Realistic size of the solar chimney

The investigation continues to determine a realistic size of the solar chimney system. The current solar chimney system produces more than enough ACH for the room but does not represent expected values. Baker [14] recommends ACH of 2 to 20 to remove heat from a building, whereas the original model predicted close to 50 for the room of 64 m^3 (refer to section 5.3).

Manitoba Hydro Place (Winnipeg, Canada) integrated many technologies to save energy and naturally ventilate, where one of the techniques was the solar chimney [57]. The total conditioned area is 690,000 ft^2 (64103 m^2), where over 1800 employees are present. The 21-story office tower has a solar chimney shaft that is 15.5 m wide, 2.85 m deep, and 119 m tall with a volume of 5257 m^3 [58]. Taking the ratio between the total conditioned area and the volume of the solar chimney (chimney ratio), it is approximately 12.2 m^{-1}, whereas the original model has a chimney ratio of 0.83 m^{-1} for the room volume of 64 m^3. Another building for comparison purposes is the BCA academy, a zero energy building in Singapore. The solar chimney for BCA academy is utilized to cool one-third of the gross floor area, where the total conditioned area of the building is 23,476 ft^2 (2180 m^2). The solar chimney system was investigated by Wong and Tan [59] and performed well even during cool days with low solar irradiance. The volume of the solar chimney duct is approximately 15 m^3 with a chimney ratio of 50 m^{-1}.

The effect of a smaller solar chimney width on the ventilation performance is investigated here. The investigation continues to determine the effect of the distance between glass and absorber (Z) for the smaller chimney width. While Chapter 4 contains results for different sizes of air gap, a

discussion about its effect on the performance of the solar chimney is missing. The effect of Z on the solar chimney performance is emphasized in this section.

6.6.1. Smaller width of the solar chimney

Figure 6.17 compares the schematics of two different chimney widths, where each has $Vent_U$ = 40 cm and $Vent_L$ = 80 cm for the room volume of 64 m^3. The width of the solar chimney was originally equal to the width of the room, and it is reduced to 1/6 of the room width for the purpose of finding a realistic size of the solar chimney system that produces reasonable ACH for the building. The adiabatic condition is considered for the wall behind the absorber to assume no-heat transfer from the chimney to the room.

Velocity (top) and temperature with streamlines (bottom) contours for two different chimney widths are compared at the center of the room in Figure 6.18. The peak velocity of the crossflow becomes smaller as the chimney width is reduced. In addition, the crossflow deflects relatively quickly from the window to the floor with the smaller chimney width, and forms a recirculation zone on the backside of the absorber due to decreasing velocity. The air velocity in the chimney increases with decreasing chimney width, especially at the lower vent due to the sudden decrease

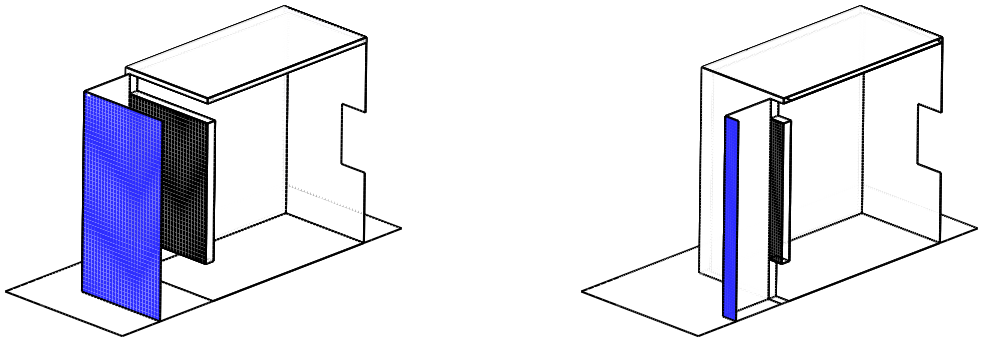

(a) Full width (b) 1/6 width

Figure 6.17 Comparison between full-width and 1/6 width solar chimney

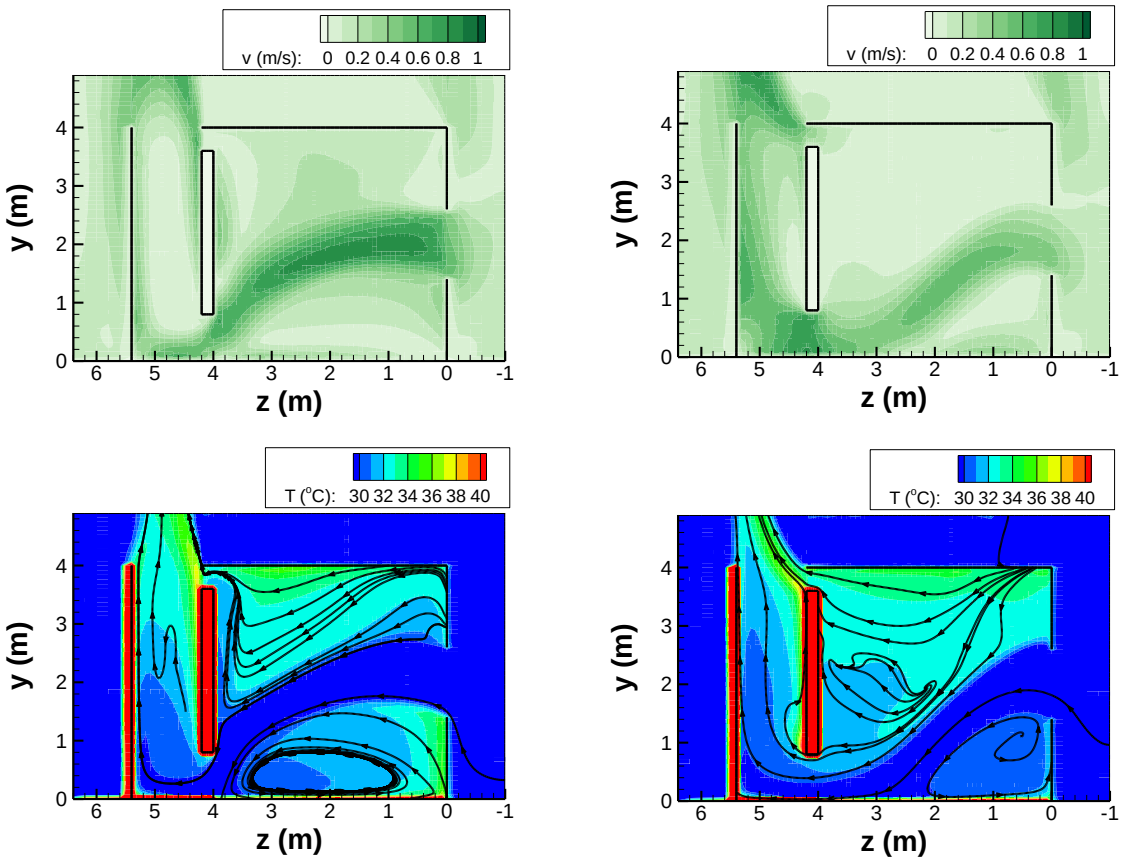

(a) Full width (b) 1/6 L_{room}

Figure 6.18 Velocity (top) and temperature with streamlines (bottom) contours at the center of the room for the solar chimney width equal to (a) full width and (b) 1/6 of L_{room}

in chimney inlet area. The average velocity at the lower vent increases from 0.49 to 0.68 m/s with decreasing chimney width.

6.6.2. Smaller air gap (Z)

In an effort to find a realistic size of the solar chimney system, a smaller air gap is tested. The air gap was originally 1/3 of the room width, and it is reduced to 1/6 of L_{room}. The chimney width remains at 1/6 of L_{room}, and the lower vent is fixed at 1/6 of L_{room}, whereas it was 1/5 of L_{room} in section 6.6.1.

Velocity and temperature contours with streamlines at the center of the room are compared in Figure 6.19 for air gap sizes 1/3 and 1/6 of L_{room}. The peak velocity in the crossflow decreases even more as Z decreases, and the crossflow deflects more from the window to the floor due to decreasing velocity. The recirculation region increases for decreasing air gap. Both air gap sizes show the suddenly increasing air velocity through the lower vent and the upper vent.

Results are summarized in Table 6.4 for the cases with different sizes of the solar chimney system. Cases (a) and (b) show the results for section 6.6.1 (the effect of width of the solar chimney system), and cases (c) and (d) are results for section 6.6.2 (the effect of Z). Comparing case (a) and

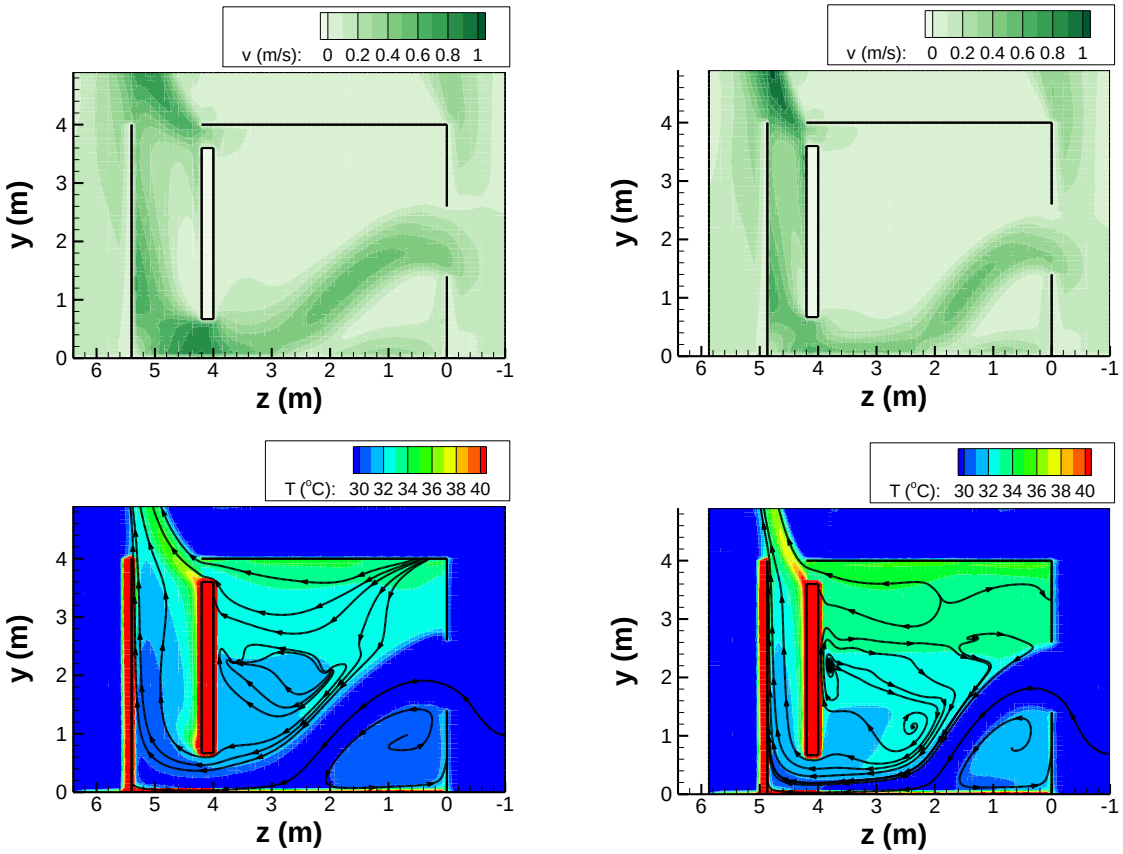

(a) 1/3 Lroom (b) 1/6 Lroom

Figure 6.19 Velocity (top) and temerpature (bottom) contours at the center of the room for Z = (a) 1/3 L_{room} and (b) 1/6 L_{room}

Table 6.4 Mass flow rate, ACH, and room temperature for different width of the solar chimney system

	$\frac{W_{chimney}}{W_{room}}$	$\frac{Z}{W_{room}}$	$\frac{Vent_L}{W_{room}}$	$\dot{m}_{Vent_U}$ (kg/s)	$\dot{m}_{Vent_L}$ (kg/s)	ACH_{total}	T_{room} (°C)
(a)	**1**	1/3	1/5	0.086	0.91	47.2	30.84
(b)	**1/6**	1/3	1/5	0.088	0.42	24.0	31.44
(c)	**1/6**	1/3	1/6	0.093	0.39	23.0	31.45
(d)	**1/6**	1/6	1/6	0.085	0.26	16.7	32.33

(b), the mass flow rate through the lower vent decreases, which is the mass flow rate of the primary flow. However, the mass flow rate through the upper vent is relatively constant despite decreasing upper vent area. The result indicates that the function of the upper vent, which is to exhaust warm air from the room, is not determined by the area of the upper vent, but it is controlled by the amount of warm air in the room. ACH decreases with reducing chimney width while the room temperature stays relatively constant. The change in ACH and T_{room} with the change in lower vent size is insignificant, consistent with the results in section 6.3 (case b and c). Decreasing ACH can be found with decreasing size of the Z (case c and d).

Table 6.5 shows the chimney ratio and the area that absorbs solar intensity in the solar chimney system (absorber and chimney floor). Absorptivity of the absorber and the chimney floor is 0.95 and 0.5, respectively. Relative changes in the area affected by the solar radiation and ACH_{total} are also summarized. Both absorber and chimney floor area decrease by 83% from case (a) to (b) since the chimney width decreases by 83%. The relative change in ACH is approximately 48%. When the lower vent size decreases from case (b) to (c), ACH is relatively constant despite increasing absorber area. The result indicates that the performance of the solar chimney in the building is rather determined by the volume of the solar chimney system (note the chimney ratio remains the same from case b to c). ACH decreases by 27.4% from case (c) to (d), where only the area of the chimney floor changed. These results demonstrate that the chimney floor plays an important role

Table 6.5 parameter length and surface area that absorbed solar intensity

	$\frac{A_{cond}}{V_{chim}}$ (m^{-1})	$A_{absorbed}$ (m^2)			Relative change in Area$_{absorbed}$ (%)			Relative change in ACH$_{total}$ (%)
		absorber	Chimney floor	Total	absorber	Chimney floor	Total	
(a)	0.83	12.8	4.8	17.6				
(b)	5	2.13	0.8	2.93	-83.3	-83.3	-83.3	-48
(c)	5	2.22	0.8	3.02	+4.2	0	+3.1	-4.1
(d)	10	2.22	0.4	2.62	0	-50	-13.2	-27.4

along with the absorber plate to create buoyancy forces. The chimney ratio increases from 0.83 to 10 from case (a) to (d), where ACH for case (d) represents a more reasonable value for ventilating a building. The important point to make for the section is that the original solar chimney system (case a) was too large compared to the room to be conditioned. In summary, a reasonable chimney size will depend on the application. The reasonable chimney ratio for the current building is approximately 10 and can be used as a guideline for other applications.

6.7. Conclusions

The applications of the solar chimney can vary widely depending on the building environment. Considering two important factors (ACH and temperature) for cross-ventilation, the building design was modified to improve both factors. The extension of the solar chimney height improved ACH, however the ventilation was poor, creating undesirable recirculation above the primary flow and thus the room over-heated. The addition of the upper vent improved the air circulation and room thermal condition by exhausting warm air from the room.

In an effort to model a more realistic scenario, the effect of vent sizes (upper and lower), absorbed solar radiation on the room floor, insulation, and chimney sizes were investigated. The study emphasized the necessity of the upper vent for cross-ventilation to improve air circulation inside the building. Increasing size of either the upper or the lower vent had a negative effect on the thermal condition of the building with the consideration of absorptivity on the floor. The effect

of the vent sizes on ACH and room temperature mitigated neglecting the absorptivity on the room floor (assuming a screen is present on the vents), where the changes in solutions were insignificant, especially for the upper vent sizes greater than 1/10 of L_{room}. The study also discussed the importance of insulation, especially for the walls behind the absorber to prevent undesirable heat transfer from the chimney to the room. Lastly, a parametric study was used to determine a reasonable chimney size to achieve proper ventilation. ACH was affected due to the changes in the chimney volume rather than the changes in the vent sizes. A reasonable chimney ratio was found to be approximately 10 for the building design in this study.

Chapter 7. Basement ventilation utilizing solar chimney

7.1. Introduction

The indoor air quality is an important factor for human comfort levels. In particular, the feasibility of using basements is becoming more prevalent, yet ventilating basements has not been sufficiently addressed. In the past, underground spaces were utilized as storage spaces because they are dark, cooler regions, yet poorly ventilated [60, 61]. However, the demand for more living spaces has increased, especially in urban areas, and basements are now commonly used for the purposes of residential living spaces, offices, and public spaces such as subway stations, bars, restaurants, parking lots, etc.

Subway stations can be used as an example to demonstrate the heavy use of underground space, where people spend considerable time [62]. The World's busiest subways are in Tokyo (Japan), Moscow (Russia), Seoul (Korea), and Shanghai (China), where annual passenger rides are over 2 billion in each city. Tokyo has the most passenger rides, which are annually 3.16 billion and daily 8.7 million. Figure 7.1 presents photographs from the subway in Seoul to provide an example of the crowdedness in such areas.

Maintaining good air quality is essential when considering health concerns for passengers as well as the workers, but it is often challenging due to heavy use and overcrowding [63, 64]. Pollutants are generated internally and externally from outside ambient air in such confined areas and these pollutants may accumulate without proper ventilation. However, underground ventilation is often challenging in the summer, where basements are usually cooler compared to ambient outdoor air; thus exhausting hot air to replace cold air underground may be difficult

without mechanical devices, and does not necessarily improve thermal conditions. Still, air circulation is necessary for underground spaces and can also improve thermal comfort by providing a breeze.

While the ventilation in the basement is crucial nowadays due to high occupancy, it is rarely studied, and the application of solar chimney for ventilating basements has not been explored. This chapter investigates basement ventilation utilizing a solar chimney system and suggests possible

Figure 7.1 Crowded subway stations in Seoul

use of solar chimney application in residential or commercial buildings with basements. The main concern is whether ACH is sufficient to replace air underground utilizing an appropriate size of the solar chimney system found in Chapter 6. The study also investigates the effect of human heat sources in a building with a main floor and basement, examining the change in flow patterns and thermal conditions.

7.2. Location of various vents

The primary interest is to determine the appropriate vent locations in the basement for the effective ventilation. The basement ventilation is often challenging because the basement air is usually cooler compared to the outdoor air during the summer. Figure 7.2 shows a layout of the upper and the lower room, which will be labeled as the main room and basement, respectively. Various vent locations and spaces are highlighted with yellow and blue, respectively. The basement volume and main floor volume are identical with a volume of 27 m^3. The duct (connecting the outdoor to the basement) has the same width as the window. This section does not account for the realistic conditions, where the focus is to find the appropriate vent locations for the

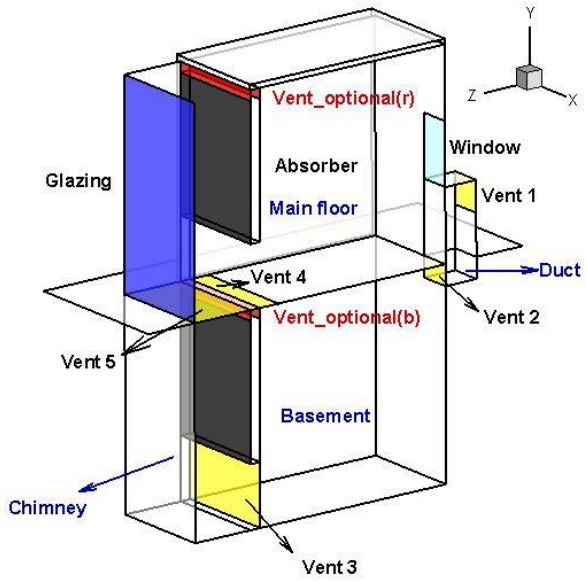

Figure 7.2 Schematic of various vent locations for basement ventilation

Table 7.1 Conditions and location of vents in the basement

	$vent_2$	$vent_3$	$vent_4$	$vent_5$
Test A	Top	Opened	Closed	Opened
Test B	Top	Opened	Opened	Opened
Test C	Bottom	Opened	Closed	Opened
Test D	Bottom	Closed	Opened	Closed

basement. The realistic conditions are implemented in the next section. The basement walls are at constant temperature of 21.85°C (295K), 5°C cooler than the outdoor ambient condition. The initial condition of the basement is also 21.85°C.

Four different combinations of the vent locations for the basement are summarized in Table 7.1, and presented in Figure 7.3, where the opened vents are highlighted as yellow. The exit of the duct, $vent_2$, refers to the inlet vent to the basement, where it is either located at the top (Test A and

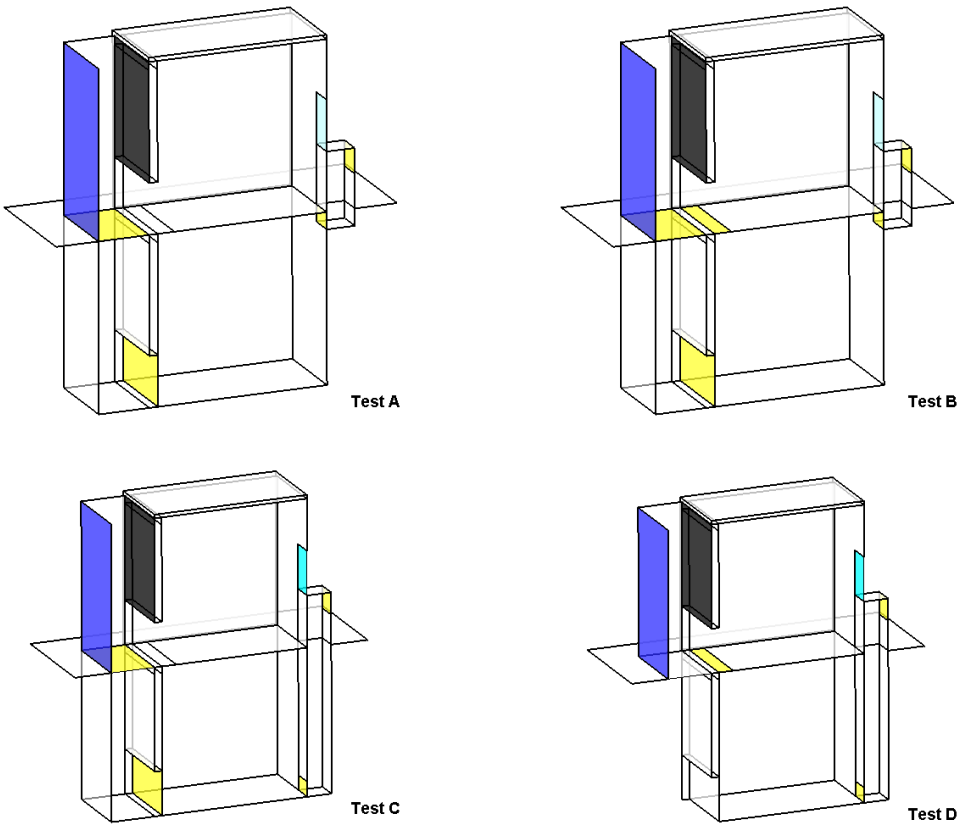

Figure 7.3 Illustration of different vent locations for Test A to D

B) or bottom (Test C and D) of the basement. The solar chimney is extended underground for Test A, considering both $vent_3$ and $vent_5$ opened. Test B accounts for $vent_4$ to be opened in addition to Test A, where $vent_4$ is located at the ceiling of the basement. Test C has the same vent conditions as Test A, but $vent_2$ is located at the bottom section of the basement, having a longer duct. Test D does not consider the extended solar chimney at the basement, but includes a longer duct with $vent_4$ opened.

Figure 7.4 shows velocity and temperature contours superimposed with streamlines for Test A and B at the center of the building. Velocity magnitude of the primary flow in the main floor is large compared to the basement because it is more difficult to draw air into the basement. However,

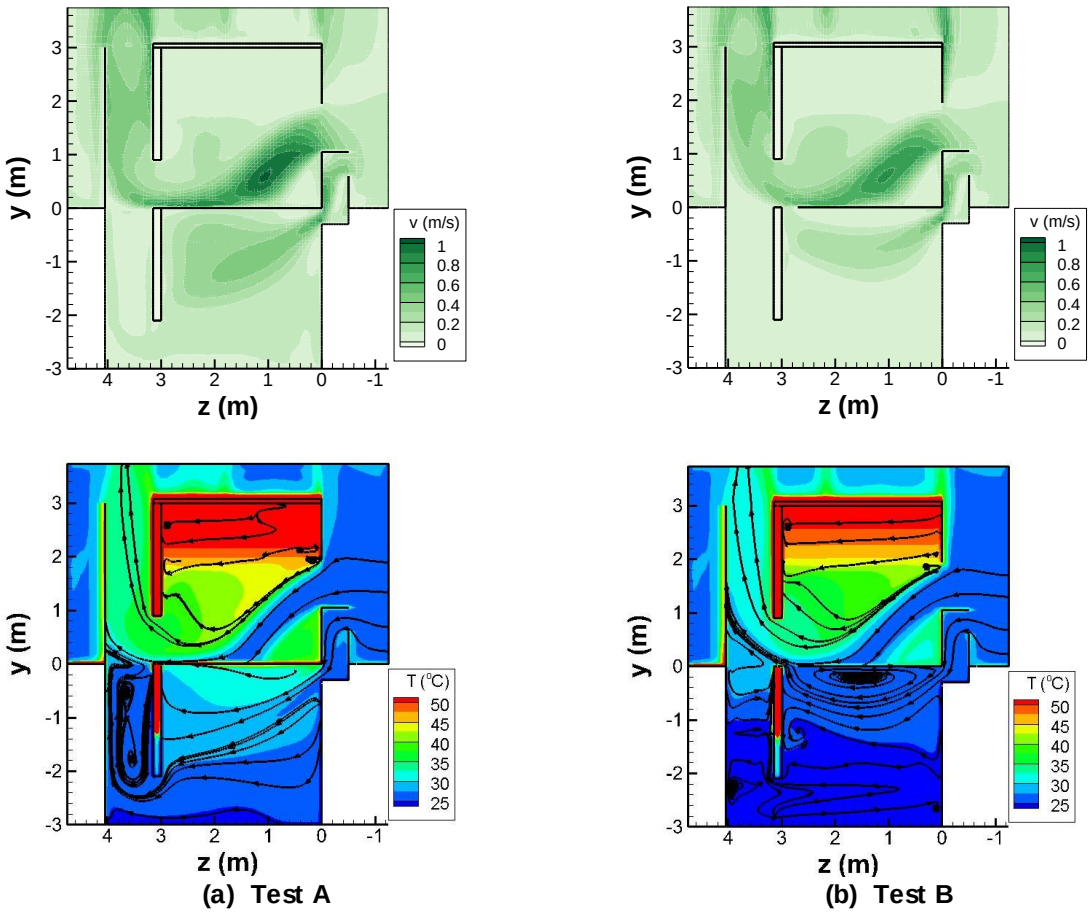

Figure 7.4 Velocity (top) and temperature contours superimposed with streamline (bottom) for (a) Test A and (b) Test B

the presence of the air movement in the basement indicates that the solar chimney system produces enough buoyancy to draw the warm air into the basement. The basement is relatively well ventilated for Test A compared to Test B, where recirculation occurs near the ceiling of the basement. The outdoor ambient air travels along the basement ceiling for Test B because the outdoor ambient air is warmer than the basement air. In contrast to Test A, the lower vent of the basement ($vent_3$) is the only vent to exhaust air from the basement, and thus the outdoor air has to travel across the basement from top to bottom before it leaves.

Test C and D are compared in Figure 7.5, where both cases have a longer duct. Similar flow patterns and thermal conditions are predicted in the main floor compared to Test A and B. The

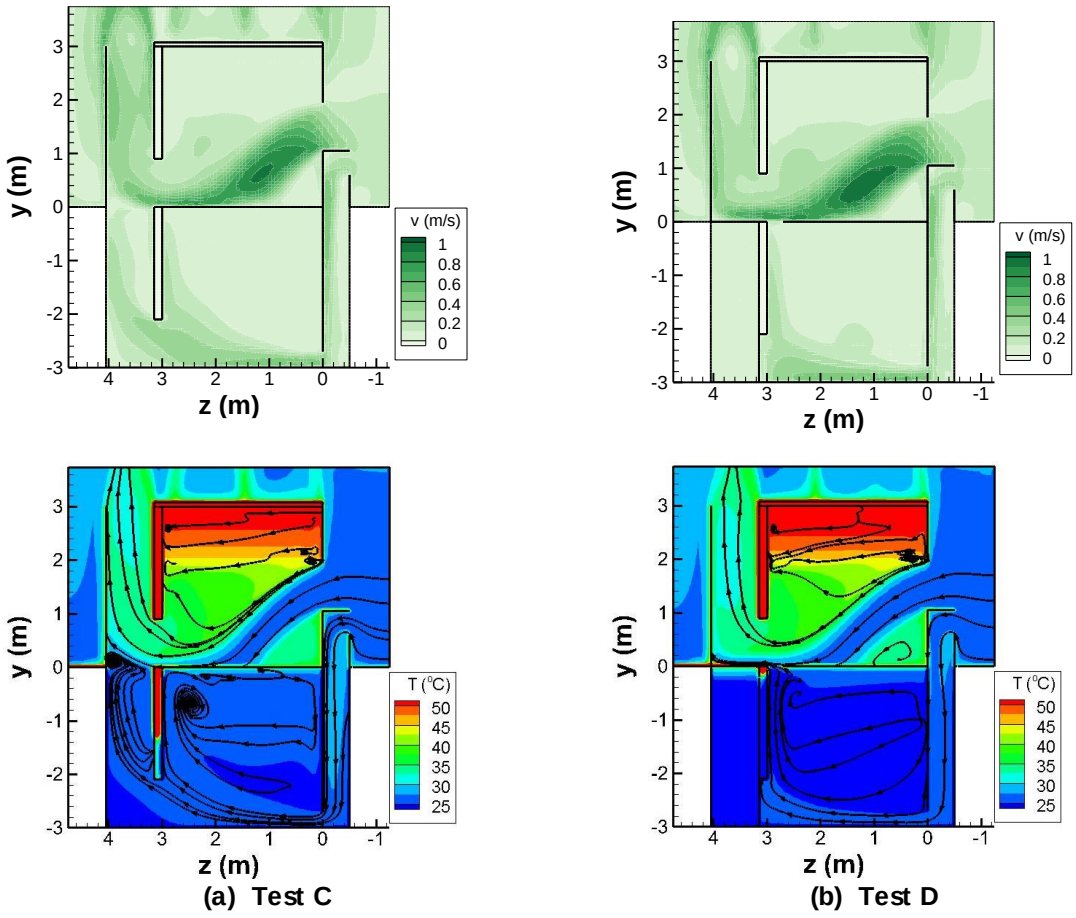

Figure 7.5 Velocity (top) and temperature contours superimposed with streamline (bottom) for (a) Test C and (b) Test D

outdoor ambient air enters at the bottom section of the basement and leaves through the lower vent of the basement chimney for Test C, where a recirculation region forms near the ceiling. The basement is well ventilated for Test D examining the streamlines, where the outdoor air travels from the floor to the ceiling, across the basement. Comparing a short duct (Test A and B) to a long duct (Test C and D), velocity magnitude in the basement is smaller for a longer duct, which is due to larger pressure difference requirements.

Mass flow rates of the air through the vents are compared in Table 7.2. Mass flow rate through $vent_5$ is not presented since it is identical to $vent_3$. Air entering the basement is generally larger when the duct is shorter (Test A and B). Most of the air entering the basement leaves through $vent_4$ for Test B, not properly ventilating the basement space.

ACH and average temperature in the basement and main floor are summarized in Table 7.3 for Test A to D. ACH is relatively large in both spaces compared to the recommended value by Baker [14] because the chimney ratio is 0.83 for Test A – C and 1.66 for Test D (refer to section 6.6). The result, however, demonstrates that the wall-solar chimney has potential for providing enough ventilation to the basement with an appropriate chimney size. ACH for the main floor is largest for Test D, which does not consider the extended solar chimney but includes the floor of the solar chimney. Note that the ACH for the main floor is identical for Test A and C because the chimney

Table 7.2 Mass flow rates through various vents

	Basement			Main floor
Flow direction	**In**	**Out**		**In**
Vents	**$vent_2$**	**$vent_3$**	**$vent_4$**	**Window**
Test A	0.159	0.159	0	0.381
Test B	0.133	0.0126	0.1204	0.310
Test C	0.102	0.102	0	0.380
Test D	0.107	0	0.107	0.423

Table 7.3 ACH and average temperature

	ACH		Temperature (°C)	
	Basement	**Main floor**	**Basement**	**Main floor**
Test A	18	43.0	27.6	39.8
Test B	15	35.1	24.4	37.3
Test C	11.57	42.9	25.0	37.8
Test D	12	47.8	24.9	38

size and the layout are the same. However, ACH in the basement is different for Test A and C due to difference in the duct length. The solar chimney system for Test A and C absorbs same amount of solar energy, but less ACH is induced in the basement for Test C since a longer duct requires a larger pressure difference to draw fresh air.

While large ACH is achieved for all tests, poor air circulation is found for Test B and C, where the inlet and outlet vents are located at the same level, either both vents at the top or bottom sections of the basement. Thus, the recommended vent locations for the basement are Test A and D, where the inlet and outlet vents are located at different heights, creating a diagonal crossflow.

7.3. Realistic considerations

Chapter 6 investigated the effect of the realistic considerations for the solar chimney, which included appropriate vent sizes, the solar radiation effect on the room floor, the insulation on the backside of the absorber, and the proper chimney size. The investigation on the basement ventilation continues in this section accounting for those realistic conditions presented in Chapter 6. The volume of each space is 64 m^3, and the upper vent is included in the main floor chimney. Two sets of different opening locations are compared for the basement, where the first layout has the inlet vent at the upper section (a short duct) and the outlet is located at the lower section (refer

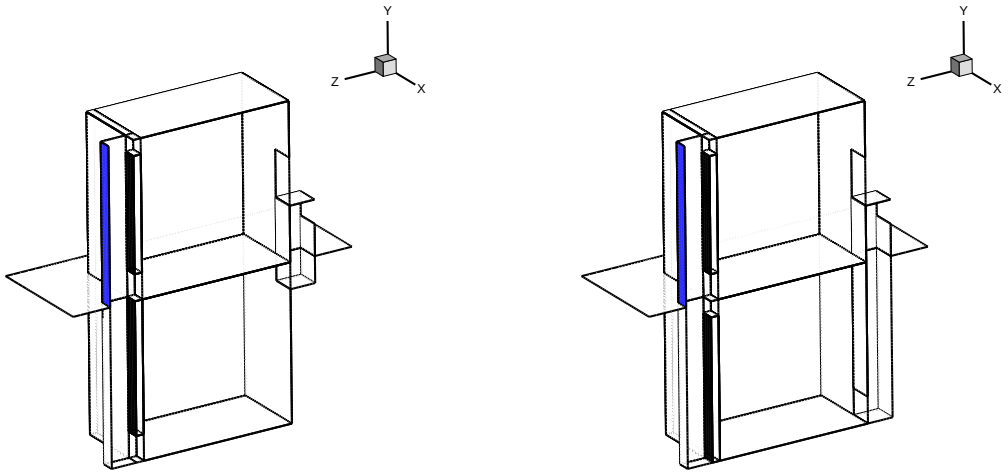

Figure 7.6 Schematics for case E (left) and F (right)

to Test A in section 7.2). The second layout has the inlet vent at the lower section (a long duct) and the outlet at the upper section of the basement, which is similar to Test D in section 7.2 except the basement includes an extended chimney and an upper vent instead of vent$_4$. These new cases are labeled Test E and Test F, respectively. Layouts for the two cases are presented in Figure 7.6. The chimney width, the lower vent, and the air gap (Z) are 1/6 of the room width (L_{room}), and the upper vent is 1/10 of L_{room}, and the chimney ratio is equal to 10 for both cases. The walls behind the absorber are adiabatic assuming no-heat transfer from the chimney to the indoor space.

Velocity and temperature contours at the center of the building are presented in Figure 7.7, and similar flow patterns and thermal conditions are presented for Test E and F. Considering a proper solar chimney size, the velocity magnitude in both spaces are smaller compared to results in section 7.2. Examining temperatures, the outdoor ambient air slightly cools as it descends in the longer duct before it is supplied to the basement. A cool region is present inside the basement chimney for Test E, which affects approximately 1/4 of the main chimney floor. The streamline at that region shows that the crossflow in the main floor is blocked due to the cool region, which is

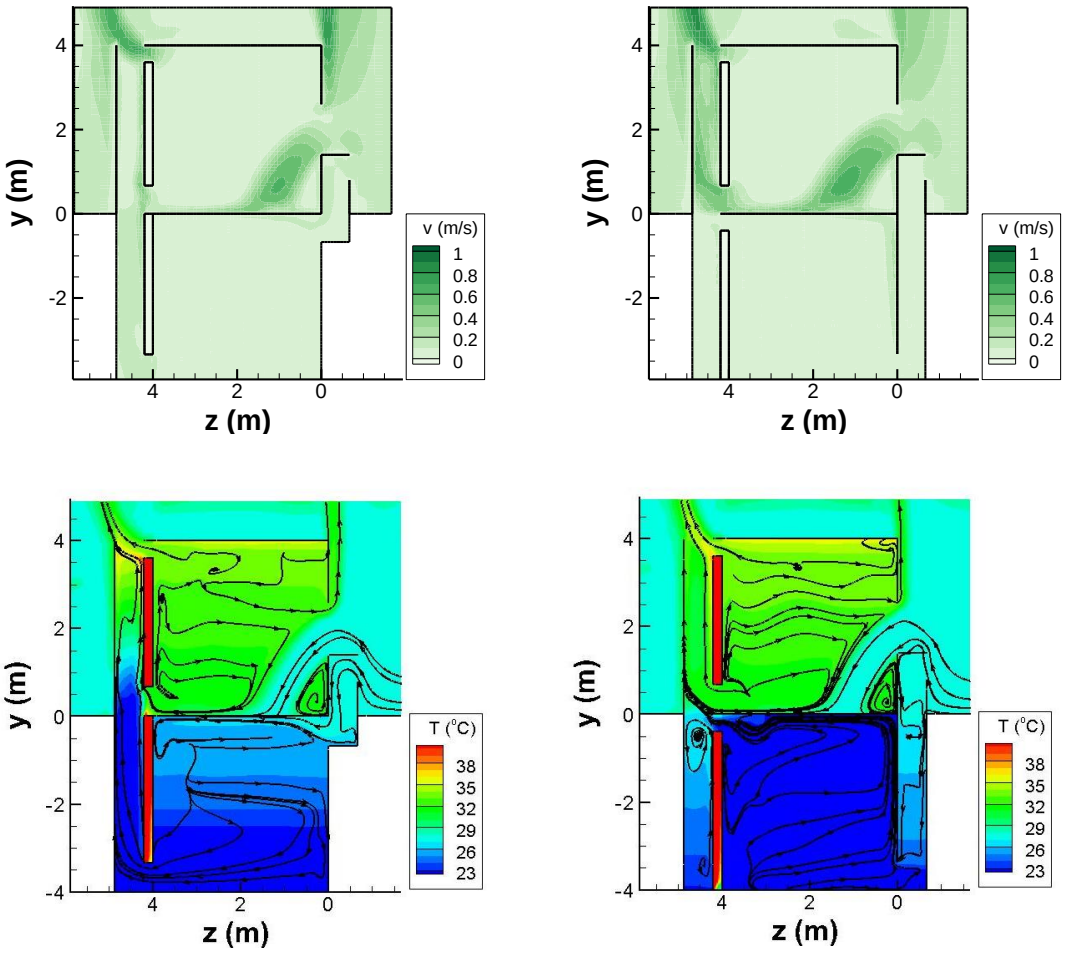

Figure 7.7 Velocity and temperature contours superimposed with streamlines for Test E and F

the flow from the basement chimney. The streamlines in each space show that ventilation is achieved even for the basement, despite the low velocity in the basement. The main floor is well ventilated due to the presence of the upper vent allowing the warm air to exhaust from the space. A recirculation zone is noticeable inside the basement solar chimney for Test E near the section that transitions to the main floor chimney.

Pressure contours for Test E and F are compared in Figure 7.8. The pressure gradient across the building is larger for Test E. The negative pressure and zero-pressure region is observable in

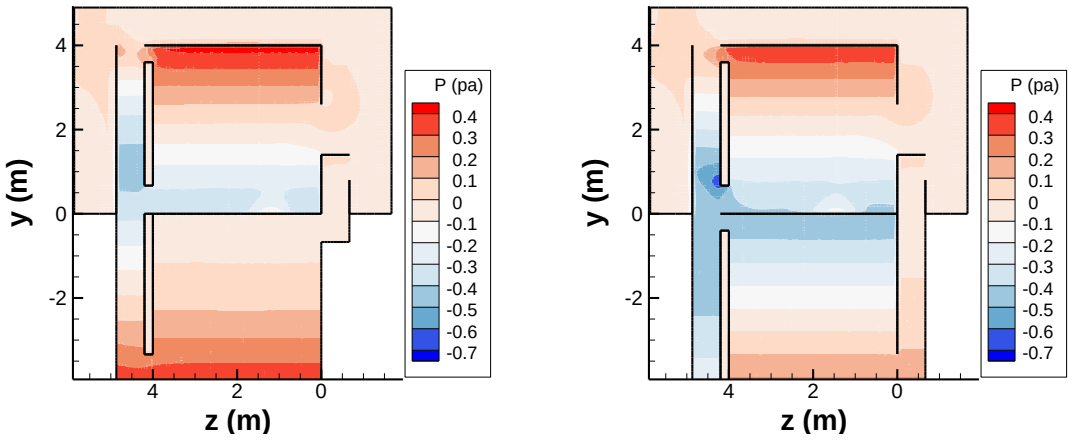

Figure 7.8 Pressure contours for Test E (left) and F (right) (fix case to test)

the basement chimney for Test F, where recirculation occurs. The space inside the chimney is ineffective and a better design option is discussed for Test F in the later section.

ACH and temperature for the room and the basement are summarized in Table 7.4. Baker [14] suggests ACH of 1 – 2 to maintain a minimum air quality, where the predictions meet the requirements. Comparing Test E to F, ACH is larger in the basement for Test E while it is smaller in the main floor. In order for the warm air to enter the basement, it needs to flow against the buoyancy force. Thus, a larger pressure difference is needed to supply warm air deeper underground, which is the reason for less ACH for Test F. The room temperature is relatively the same for two cases. An acceptable ACH recommended to remove heat from the building [14] is between 2 – 20, where both Test E and F demonstrate sufficient ventilation to exhaust warm air

Table 7.4 ACH and average temperature for Test E and F

	ACH		Temperature (°C)	
	Basement	**Main floor**	**Basement**	**Main Floor**
Test E	3.13	8.13	24.0	32.1
Test F	0.9	14.73	22.1	32.0

from the main floor. While Test E appears to be the better ventilation arrangement, further analyses continue to determine what happens if heat sources are included.

7.4. Human heat sources

The effect of human heat loads is investigated using Test E and F from section 7.3. Building layouts and the boundary conditions are identical, where 2 or 6 people are added to the main floor and basement. Figure 7.9 shows schematics for Test E with 2 and 6 people in each space, where human locations are identical for Test F though it is not shown. Each human is modeled as a parallelepiped with a height of 1.7 m and a width of 0.35 m in each side to form a square cross-

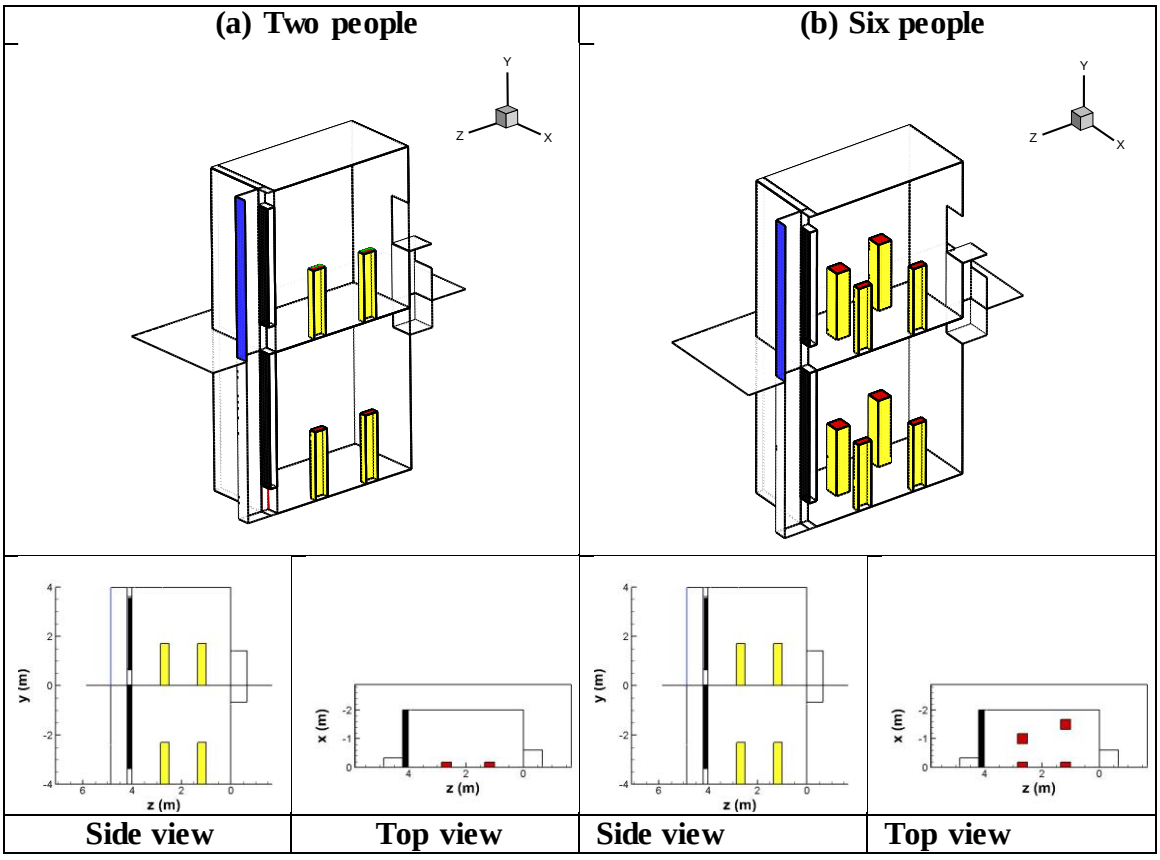

Figure 7.9 Layouts for Test E with consideration of (a) two people and (b) six people in each space

section, and each person releases 75 W heat from the head. Two half humans are considered in each space at the symmetry boundary (center of the room) for both 2 and 6 people scenarios. The additional humans are positioned 1 m and 1.5 m away from the center of the building to represent a congested area. The objective is to investigate the effect of human heat sources on the flow patterns as well as the thermal conditions.

Temperature contours with streamlines are compared for three different scenarios (no human, 2 humans, and 6 humans) at the center of the room (x = 0 m) in Figure 7.10, x = 1 m in Figure 7.11, and x = 1.5 m in Figure 7.12. First focusing on temperature contours at the center of the building in Figure 7.10, the effect of heat sources is noticeable, especially in the basement, where thermal plumes are generated above each person. Overall temperatures increase with increasing number of humans in the building. The human body disrupts the crossflow, and multiple air recirculation regions are noticeable. Examining Test F, the streamlines show that the outdoor ambient air travels along the wall above the inlet of the basement as soon as it enters. The outdoor air tends to rise when it enters the basement because it is warmer than the basement, and thus the bottom portion of the basement is never properly ventilated by the fresh air. Comparing Test E to F, the overall thermal condition in the main floor is similar while the thermal condition in the basement is warmer for Test E.

Figure 7.11and Figure 7.12 shows the contours at x = 1 m and 1.5 m, where each figure shows a plane cutting through each of the additional humans in the congested space. Temperature distribution is similar regardless of the plane. The flow patterns in the main floor are similar for Test E and F.

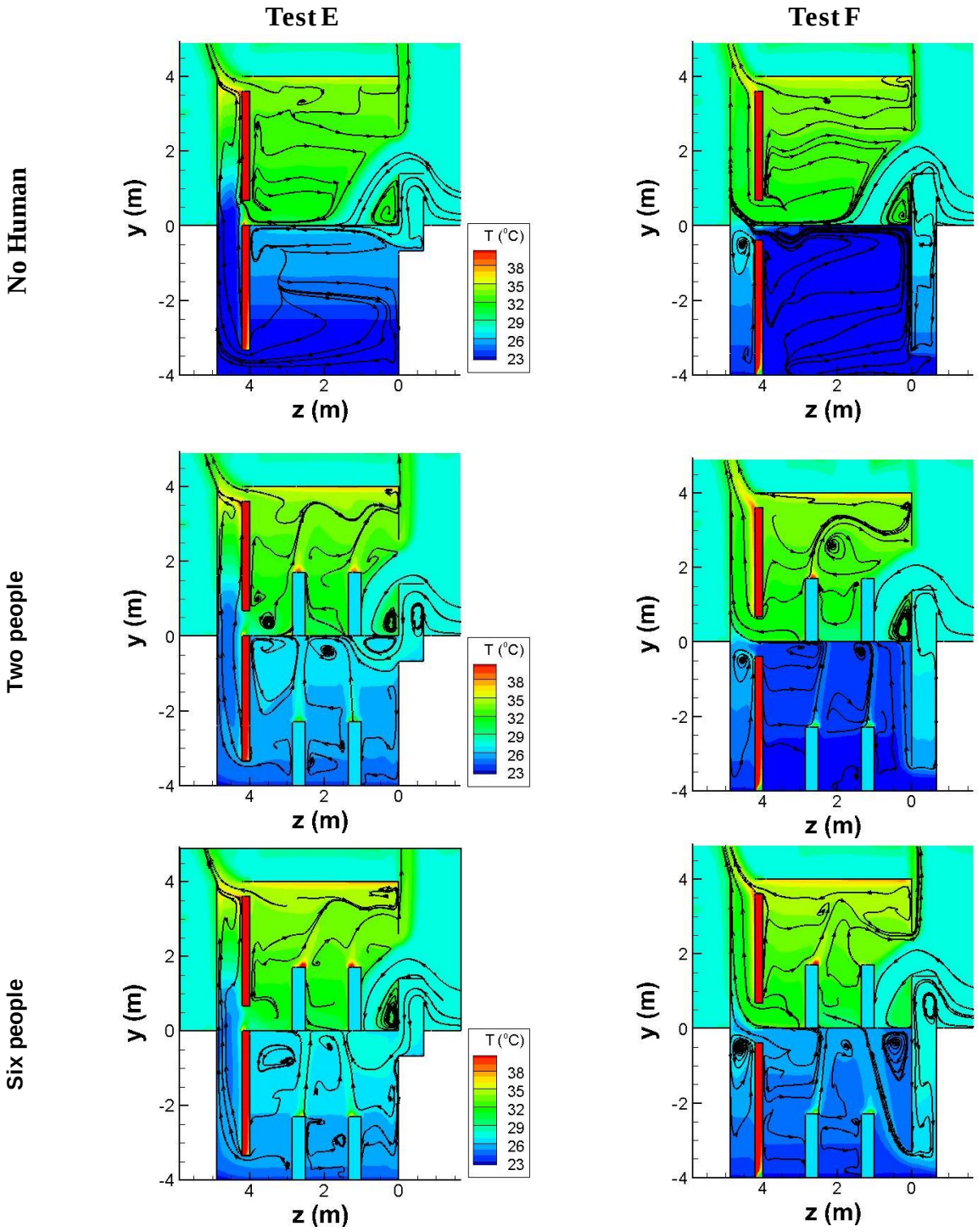

Figure 7.10 Temperature contours for Test E (left) and F (right) with no human, two people, and six people at the center of the building (x = 0 m)

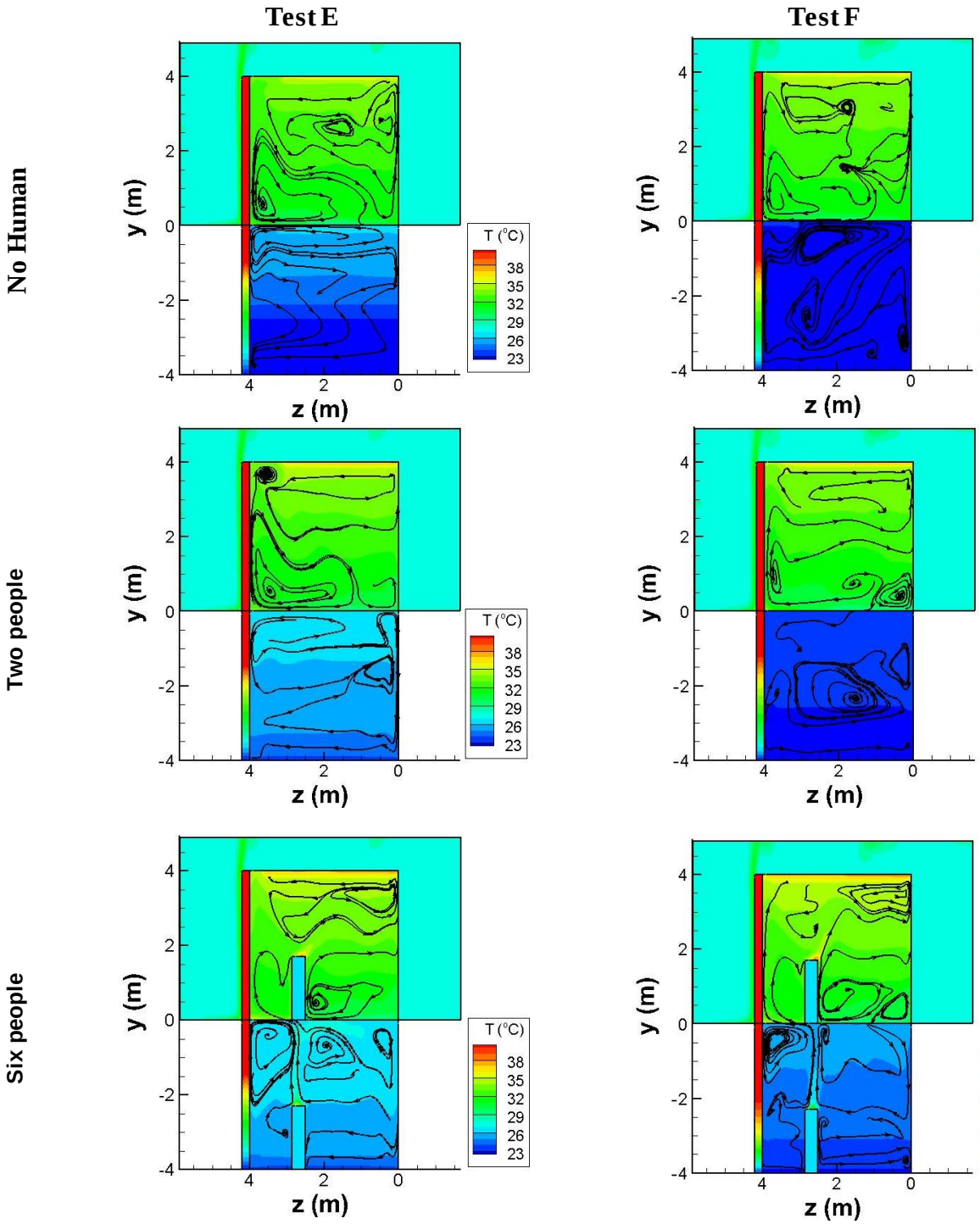

Figure 7.11 Temperature contours for Test E (left) and F (right) with no human, two people, and six people at x = 1 m

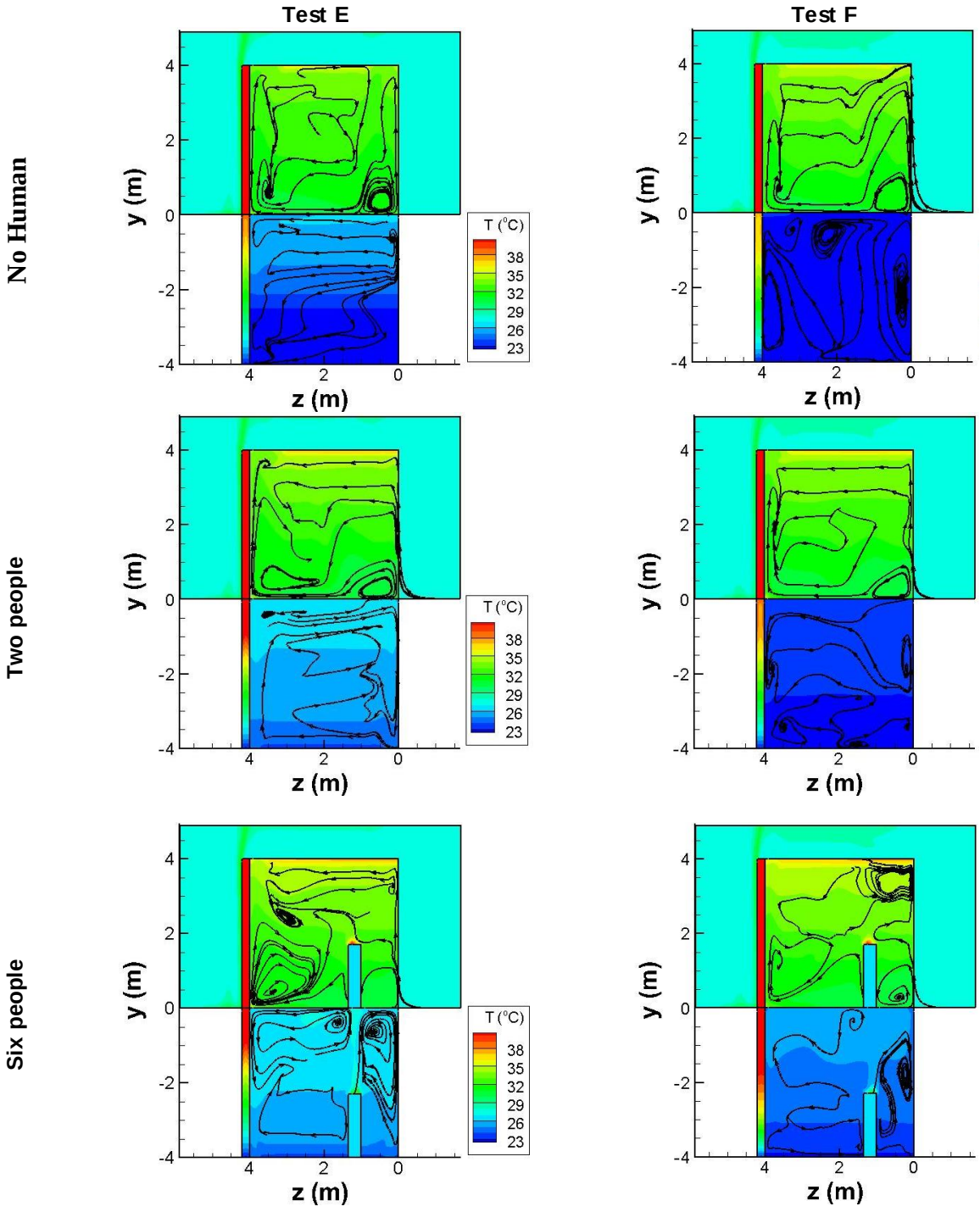

Figure 7.12 Temperature contours for Test E (left) and F (right) with no human, two people, and six people at x = 1.5 m

Temperature contours superimposed with streamlines are shown at different heights of the building in Figure 7.13 and Figure 7.14 for the main floor and the basement, respectively. Two different heights in each space are plotted, (a) y = 0.2 m and (b) 1.5 m, where the levels are near the ankle and the head of the human, respectively. Examining temperature contours in the main floor (Figure 7.13), temperatures are higher at y = 1.5 m compared to y = 0.2 m. The flow patterns and thermal conditions are not much affected by the additional humans at the height of 0.2 m in the main floor. At y = 1.5 m, the effect of humans is more obvious, where the crossflow is disrupted and forms recirculation zones adjacent to the humans. Furthermore, increasing temperatures are noticeable with the addition of the humans. The difference between Test E and F in the main floor is insignificant.

Figure 7.14 shows temperature contours at different heights in the basement. Similar to the main floor, temperatures are higher at the higher level (y = 1.5 m), and temperatures increase with increasing numbers of humans. The reverse flow into the inlet of the basement is more obvious for Test F examining streamlines at y = 0.2 m, which is due to the poor ventilation (see the discussion for Figure 7.10). On the contrary, the flow directs towards the outlet of the basement for Test E at y = 0.2 m. Despite that the fresh air is warmer than the basement air, it ventilates across the basement from top to bottom for Test E, and leaves through the lower vent located at the bottom section of the basement. Buoyancy forces are created with the solar chimney, which allows the warm air to flow downward.

Main floor contours

(a) y = 0.2 m

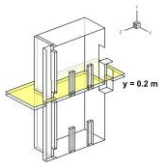

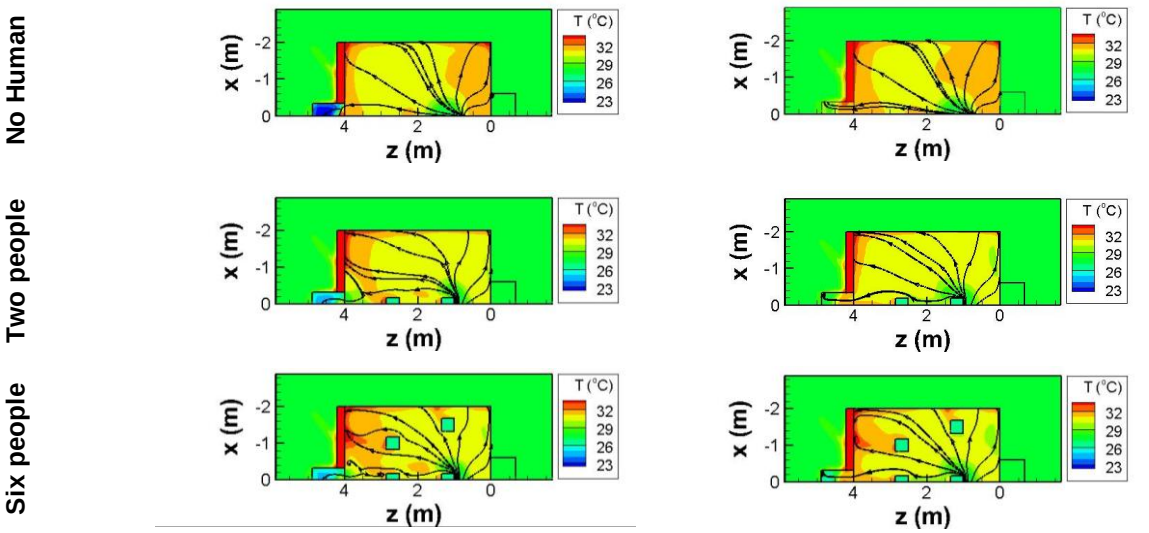

(b) y = 1.5 m

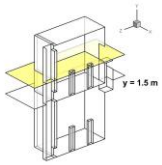

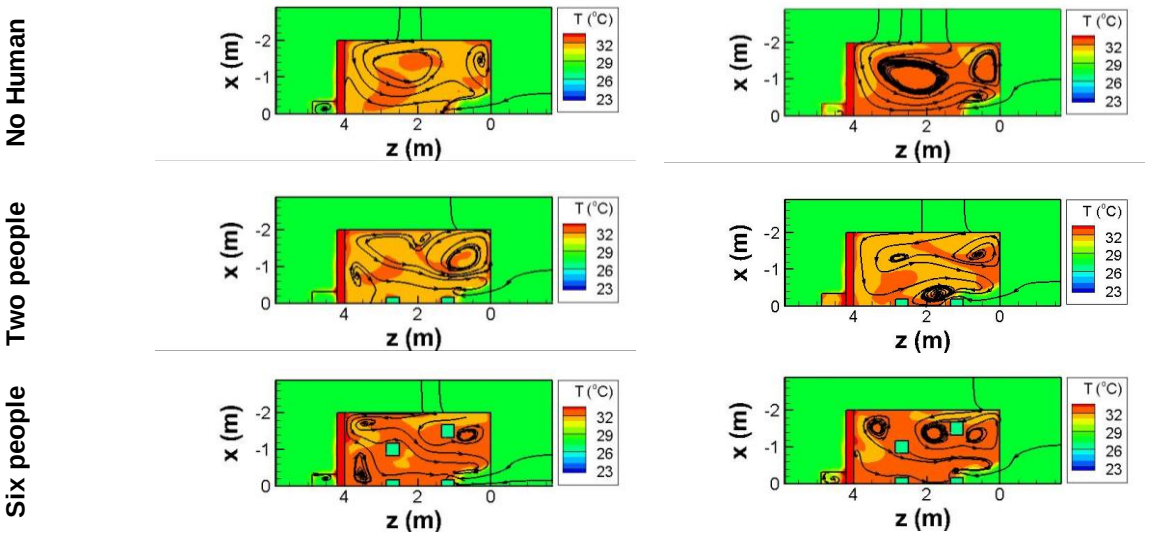

Figure 7.13 Temperature contours for Test E (left) and F (right) with no human, two people, and six people at (a) y = 0.2 m and (b) y = 1.5 m for the main room

Basement contours

(a) y = 0.2 m

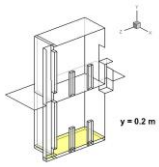

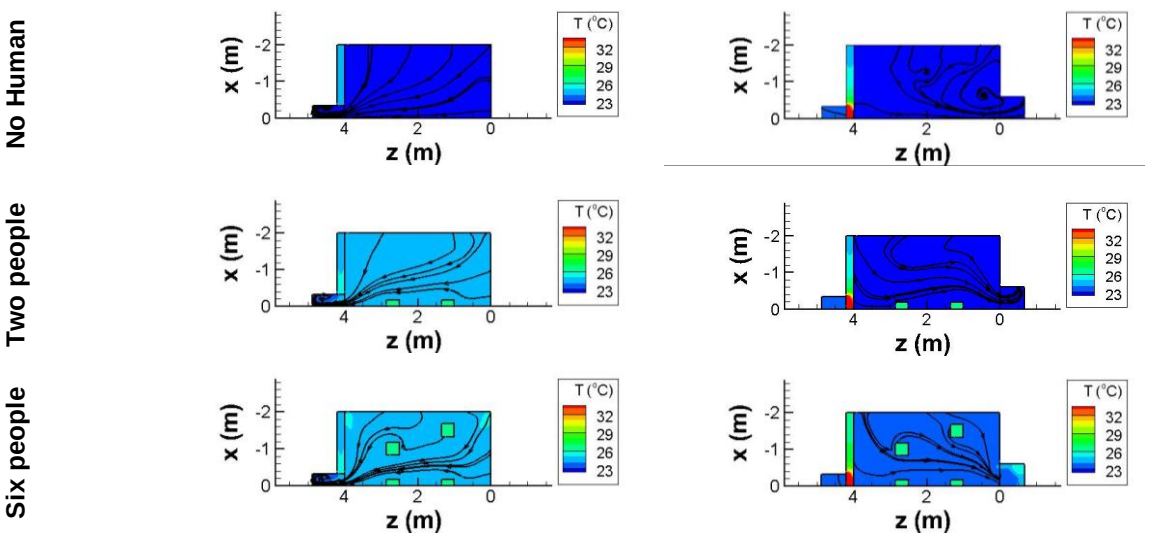

(b) y = 1.5 m

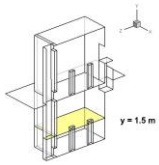

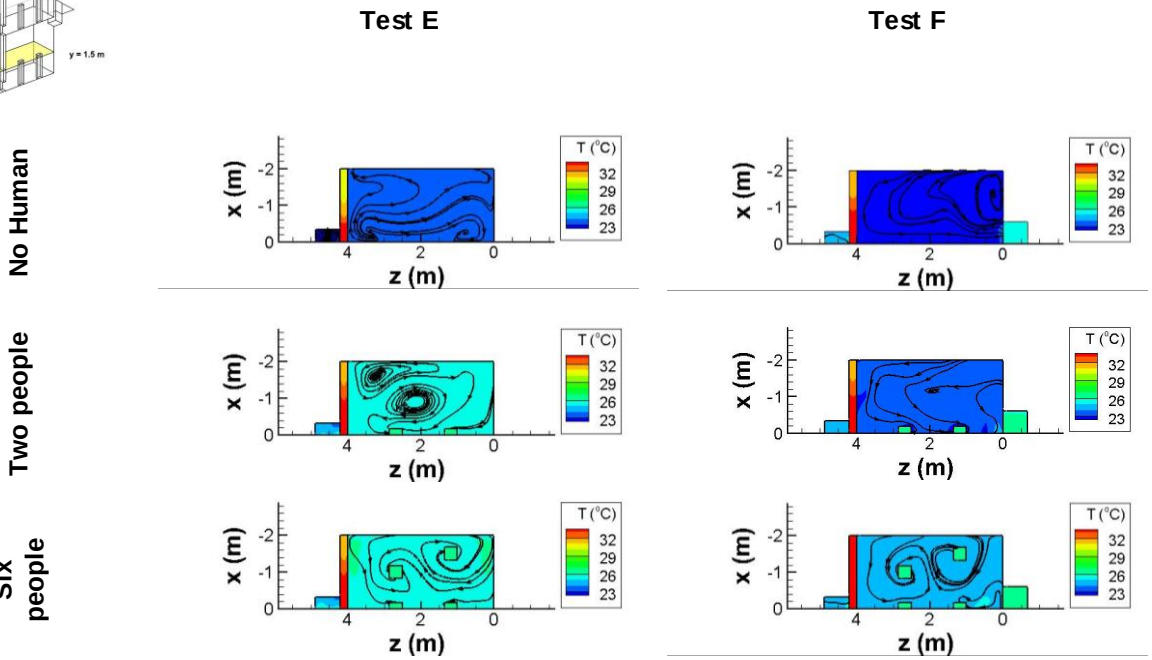

Figure 7.14 Temperature contours for Test E (left) and F (right) with no human, two people, and six people at (a) y= 0.2 m and (b) y = 1.5 m for the basement

Mass flow rates through various vents are summarized in Table 7.5 to further investigate the flow patterns and to compare results with the inclusion of humans. Mass flowing into the basement is larger for Test E regardless of the heat sources, however, the air supplied to the main floor is larger for Test F. Interestingly for Test E, mass flowing out through the upper vent dominates the lower vent in the main floor. Furthermore, mass flow rate at the lower vent of the main floor is negative for Test E when more people are considered in the building, indicating that the air flows into the main room from the chimney. The air flowing through the chimney seems to be blocking the pathway of the crossflow in the main room through the lower vent (also noticeable in the contours in Figure 7.10).

ACH and temperature in each space are summarized in Table 7.6 for Test E and F for three different scenarios. When two people are added to each space, ACH for the basement increases while ACH for the main floor decreases for both Test E and F. Increasing temperature is more obvious in the basement, where temperature for the main floor remains relatively constant despite the consideration of the humans. Increasing basement temperature is due to people as well as more outdoor air affecting the basement (larger ACH). When four more people are added to each space, ACH decreases in the basement while it increases in the main floor for Test E. On the contrary, ACH continues to increase in the basement for Test F, but ACH is decreasing in the main floor. However, both cases induce sufficient ventilation to remove heat from the building.

Table 7.5 Mass flow rates through vents for Test E and F for no heat and heat

		Basement (kg/s)	Main floor (kg/s)		
Flow direction		In = out	In	Out	
		Vent 2	window	$Vent_{Lower}$	$Vent_{Upper}$
No human	Test E	0.066	0.171	0.031	0.14
	Test F	0.012	0.31	0.21	0.091
2 people	Test E	0.1	0.14	-0.009	0.15
	Test F	0.03	0.28	0.18	0.099
6 people	Test E	0.1	0.15	-0.005	0.15
	Test F	0.063	0.23	0.11	0.12

Table 7.6 ACH and average temperature for Test E and F for no human, 2 people and 6 people

		ACH		Temperature (°C)	
		Basement	Main floor	Basement	Main floor
No human	Test E	3.13	8.13	24.0	32.1
	Test F	0.9	14.73	22.1	32.0
2 people	Test E	4.88	6.67	25.7	32.4
	Test F	1.46	13.45	23.2	32.3
6 people	Test E	4.76	7.12	26.1	32.8
	Test F	3.0	11.04	24.6	32.8

7.5. Importance of the lower vent in the basement

In section 7.4, human heat sources were considered in the building for two different cases. Proper ventilation was conducted for Test E in the building, however, poor ventilation was detected near the floor of the basement for Test F, where the air was recirculating. Another problem for Test F was that the basement chimney space was not functioning effectively due to the presence of a recirculation region within the chimney. In this section, the lower vent is added to the basement chimney system for Test F, where the new case will be referred as Test G. Two people are considered in the main floor and basement, where the isometric and side view of the building are presented in

Figure 7.15 (top view is same as the one shown in Figure 7.9 for two people). The objective is to compare air circulation between Test F and G, and investigate the effect of the lower vent of the basement solar chimney on the ventilation.

Figure 7.16 compares temperature contours superimposed with streamlines for Test F and G at various locations, $x = 0$ m (center of the building), $y = 0.2$ m and 1.5 m in the main floor and the basement. The contours for Test F in Figure 7.16 are identical to the ones presented for two humans in Figure 7.10, Figure 7.13, and Figure 7.14. Overall flow patterns and temperature distribution

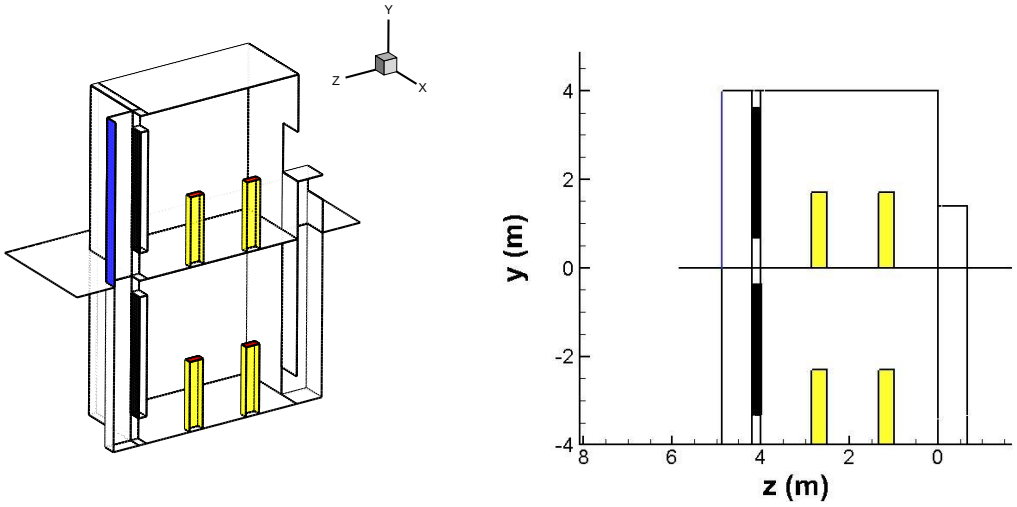

(a) Isometric view **(b) Side view**

Figure 7.15 Building layout for Test G with consideration of two people (a) isometric view (b) side view

are not significantly affected by the addition of the lower vent in the basement, especially near the main floor. Examining streamlines at the center of the building (x = 0 m), the air circulation inside the basement chimney is better with the inclusion of the lower vent. The contours at different heights in the main floor are almost identical for Test F and G. Examining the contours at y = 0.2 m in the basement, the air still flows into the basement (towards right) for Test G. However, the air also flows through the lower vent of the basement chimney (towards left). While the problem of adequately and effectively supplying fresh air in the basement still persists, air circulation improves by exhausting the cool air that originally recirculated near the floor without the lower vent. A cooler region is detected for Test G at y = 1.5 m in the basement, which may be due to better air circulation.

Mass flow rates, ACH, and temperatures for Test F and G are summarized in Table 7.7 and Table 7.8. The difference between Test F and G is insignificant, except the mass flow rate

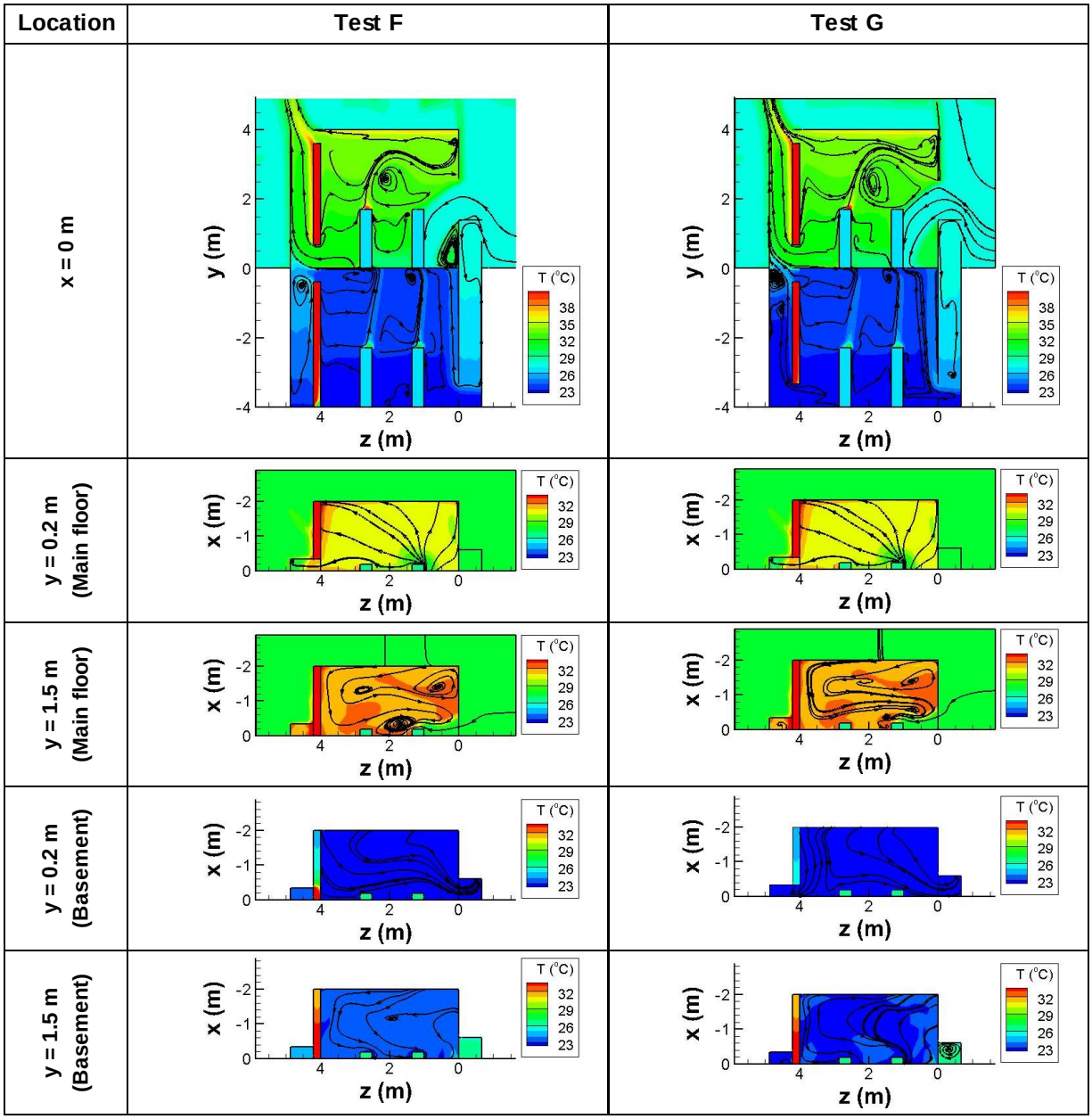

Figure 7.16 Temperature contours superimposed with streamlines for Test F and G at various locations: x = 0 m, y = 0.2 and 1.5 m in the main floor and basement

distribution in the basement. Approximately one-half of the fresh air entering the basement exhausts through the lower vent for Test G. The result demonstrates that the lower vent is essential for ventilating the basement during hot seasons, otherwise the lower section of the basement will not be properly ventilated. In addition, the constant ACH despite the additional vent indicates that

Table 7.7 mass flow rates through vents for Test F and G with two people in each space

	Basement (kg/s)			Main floor (kg/s)		
Flow direction	**In**	**Out**		**In**	**Out**	
	Vent 2	**$Vent_{Lower}$**	**$Vent_{Upper}$**	**window**	**$Vent_{Lower}$**	**$Vent_{Upper}$**
Test F	0.03	0	0.03	0.28	0.18	0.099
Test G	0.031	0.014	0.017	0.28	0.18	0.098

Table 7.8 ACH and temperature for Test F and G with two people in each space

	ACH		Temperature (°C)	
	Basement	**Main floor**	**Basement**	**Main floor**
Test F	1.46	13.45	23.2	32.3
Test G	1.464	13.4	23.1	32.3

ACH is not affected by the number or locations of the outlet vents, but it is rather due to the solar chimney size and the location of the inlet vent.

7.6. Conclusions

Basement spaces are utilized for the various applications with increasing demand of the living spaces. This study investigated the application of the solar chimney system to naturally ventilate the basements in the hot seasons. First, optimal vent locations were determined by testing different combinations of the inlet and the outlet vent locations. The basement ventilation is challenging because the warm air needs to flow downwards to enter the basement and be distributed around the basement. Additionally, it is desirable for fresh air to be evenly distributed in the cooler space. Appropriate vent locations were found where the study recommended the inlet and the outlet vents to be at different levels of the basement to create significant crossflow. However, it was relatively more difficult to draw the fresh air into the basement when the inlet vent was located at the bottom section using a long duct because a larger pressure difference is required.

The study on the basement ventilation continued with considering multiple humans in the building, where a congested scenario was also investigated. A sufficient ACH was predicted even

with the inclusion of the humans. The best ventilation was achieved when the inlet vent was located at the top section and the outlet vent was located at the bottom section. The fresh air entered the basement relatively easier when the duct was shorter, and was evenly distributed into the basement with the outlet vent at the lower section. When the inlet vent was located at the bottom (a long duct), the poor ventilation near the basement floor was detected due to the fact that the outdoor ambient air ascended when it entered the cool basement. Thus, the lower vent was added to the chimney in addition to the upper vent and the long duct. The lower vent improved air circulation, especially at the bottom section of the basement, where approximately 50% of the air exhausted through the lower vent. ACH in the basement did not change despite the consideration of the lower vent, which demonstrated that ACH does not depend on the number and the locations of the outlet vents, but it depends on the size of the solar chimney and the locations of the inlet vent.

Chapter 8. Conclusions and Future work

8.1. Summary

Energy consumption as well as the demand for the energy usage by society continues to rise, where the majority of the energy consumption is involved with conditioning the buildings. The solar chimney is a natural ventilation technique that has the potential of saving energy as well as maintaining good air quality in the building. While research on natural ventilation is important, it is often challenging to analyze the building due to its massive size. Computational fluid dynamics is a cost-effective numerical tool and it is easy to modify the building design compared to conventional experiments. Additionally, CFD offers detailed information on important variables such as velocity, pressure, solar intensity, etc. Thus, CFD has a great potential as a tool to analyze, design and optimize natural ventilation strategies in a building. In this study, the application of the wall-solar chimney for building ventilation was investigated using CFD.

The predictions of air change per hour were validated with the experimental data by Mathur et al. The solar chimney system was modeled using a three-dimensional domain. In addition, both laminar and turbulent models were utilized to better understand the flow in the chimney with changes in the air gap and chimney inlet size. The study found that the flow can be either laminar or turbulent depending on the size of the air gap and the chimney inlet, where the chimney inlet has a more significant effect on the flow regime. A new hydraulic diameter was developed using both the air gap and the chimney inlet and was utilized to calculate the Rayleigh number, where the transition from laminar to turbulent occurred at $Ra^* \sim 0.8 \times 10^8$.

The experimental study of Mathur et al. and the validated simulations utilized a room volume of 1 m^3 whereas a typical room volume is approximately 27 m^3. While a small-scale study can be helpful to understand the effect of various parameters in the system, it is not certain that the airflow

predictions in the small-scale model will agree with the airflow in the actual size of the building. Thus, the study sought a relationship between a small-scale and a full-scale model of the wall-solar chimney system. Air velocity increased with increasing room size, and the relationship between the average velocity ratio F and the room size d was $F = d^{1/3}$ regardless of the room layout. Room temperatures decreased with increasing room size, where $T^*_{overall} \approx 0.28 \cdot d^{-1/3}$. A parametric study was conducted, and variations in the position of the ventilation window, solar chimney dimensions, ambient temperature, and solar intensity were considered. Regression analysis was used to develop a relationship between velocity at the window and multiple non-dimensional variables. The predictions of velocity using the mathematical model were in very good agreement with the experiments and numerical data from Mathur et al., including results from random cases that were simulated.

The optimization of the solar chimney system was considered to suggest ways to improve the performance of the solar chimney. First, an extended chimney height was proposed to improve ACH, where the extended chimney height successfully induced larger ACH regardless of the surface type for the extended section. Poor air circulation was evident using the original design provided by the experimental study of Mathur et al., where a recirculation zone developed above the primary crossflow and the room was over-heating. An upper vent was included, which improved the air circulation by exhausting the warm air from the room. The study demonstrated the importance of the upper vent as a modification to the chimney section.

The presence of the upper vent improved the air circulation, and thus the room temperature also decreased. However, the room was still over-heating because factors such as solar radiation through the vents and poor insulation were disregarded in the original model. Solar radiation entered through the vents in the original model, and affected the room floor providing unnecessary

heat to the building. In reality, solar radiation through the vents would be prevented by having a screen over the vents that reflects solar radiation. Another crucial factor was the insulation. The absorber reaches a very high temperature as the sunlight radiates to the absorber, and it is important to prevent heat transfer from the absorber to the room. However, the wall behind the absorber was poorly insulated for the original model. When the model accounted for the screens over the vents and good insulation on the backside wall of the absorber, reasonable temperatures were predicted in the building.

Another issue was that ACH was unrealistic for the original model due to the size of the solar chimney. The solar chimney system was relatively large compared to the conditioned space, where the ratio between the total conditioned area and the solar chimney volume (chimney ratio) is normally larger than 10, however the ratio was less than 1 for the original model. A smaller chimney size was modeled by reducing the air gap and the chimney width while the chimney height remained constant. A reasonable ACH was produced when the chimney ratio was equal to 10.

Lastly, the application of the solar chimney system for the basement ventilation was investigated. Proper air circulation occurred when the inlet and the outlet vents were located at the top and the bottom, respectively. A sufficient ACH was predicted even when considering humans in the building.

8.2. Significance and contribution

The main objective for this research was to computationally model a wall-solar chimney system and demonstrate the potential of the solar chimney for building ventilation. Research on natural ventilation strategies is essential since building energy consumption continues to rise. While published literature provided the mathematical models for the wall-solar chimney system,

key factors (flow regime, 3D effect, and etc.) were ignored for the simplicity of the problem. In this study, these factors were considered and it was determined that the flow can be either laminar or turbulent in the small-scale model depending on the parameters of the solar chimney system whereas other literature assumed the flow to be laminar at all times. Realizing the difficulties of studying full-scale models, the study proposed a mathematical model to predict velocity at the inlet using multiple variables (window position, size of the room, vent sizes for the solar chimney system, and ambient temperature).

While the first portion of the dissertation strictly focused on the validation and modeling a wall-solar chimney system, the second portion focused on the optimization of the system and the considerations for using a solar chimney system in reality. The study suggested a couple of models to improve the performance of the solar chimney system. In addition, the study provided the lists of important factors that may be considered for a more realistic application and investigated the effect of each factor on the ventilation performance.

Lastly, the application of the solar chimney system was investigated for the use of underground ventilation. Despite the importance, basement ventilation is rarely studied. The study recommended appropriate vent locations for the basement, which is especially relevant during hot seasons when ambient air is warmer than indoor environments. Additionally, the work also showed the capability of the wall-solar chimney to properly ventilate the basement even for a congested scenario.

8.3. Future work

The application of the solar chimney system to ventilate underground space has not been explored sufficiently, and this study demonstrated the potential use of the solar chimney system for the basement. In order to find the optimal vent locations in the basement, only extreme locations

were tested, either near the ceiling or the floor. While this study recommends locating the inlet vent near the ceiling of the basement and the lower vent to exhaust stale warm air from the basement, the investigation on other inlet locations are recommended to optimize the vent locations.

While this study provided useful information for ventilating a residential space with the basement, public spaces are much larger and congested. Continuing the work, the performance of the solar chimney system on much larger spaces or possibly much longer spaces is necessary. In addition, the required solar chimney size must be determined to effectively ventilate the long and large underground space.

This study focused on air circulations, ACH, temperatures, and flow patterns in the building. However, the evaluation of human comfort is a much difficult problem, where multiple factors have to be considered including human body heat, metabolic rate, humidity, air contaminants, and perception. It would be an interesting study to investigate these factors and evaluate the human comfort for a realistic scenario.

References

[1] Administration, US Energy Information, 2015, "*Monthly Energy Review*".

[2] Pieprzyk, B., Kortluke, N., and Hilje, P.R., 2009, "*The impact of fossil fuels-Greenhouse gas emissions, environmental consequences and socio-econmic effcts*".

[3] Hansen, J., Reudy, R., Sato, M., and Lo, K., 2010, "*Global Surface Temperature Change*", Reviews of Geophysics. 48, RG4004.

[4] (EIA), U.S. Energy Information Administration, 2014, "*International Energy Outlook 2014*".

[5] Energy, U.S. Department of, 2012, "*2011 Buildings Energy Data Book*", Energy Efficiency & Renewable Energy.

[6] Agency, U.S. Envrionmental Protection, 1989, "*Report to Congresss on indoor air quality*". Vol. 2. 1989, Washington D.C.

[7] Emmerich, S.J., Axley, J.W., and Dols, W.S., 2001, "*Natural Ventilation Review and Plan for Design and Analysis Tools*", NIST Interagency Report 6781.

[8] Feng, J., Xu, Z., and Jie, Y. , 2008, "*Natural ventilation potential analysis of office building in China*", Journal of Tongji University, (1): p. 92-96.

[9] Brodrick, J.R. and Westphalen, D. , 2001, "*Uncovering Auxiliary Energy Use*", ASHRAE Journal. 43(2): p. 58-61.

[10] Schulze, T. and Eicker, U., 2012, "*Controlled natural ventilation for energy efficient buildings*", Energy and buildings. 56: p. 221-232.

[11] Zhai, X.Q., Song, Z.P., and Wang, R.Z., 2011, "*A review for the applications of solar chimneys in buildings*", Renewable and Sustainable Energy Review. 15: p. 3757-3767.

[12] Perlin, J. and Butti, K., 1980, "*A Gold Tread: 2500 Years of Solar Architecture and Technology*". 1980.

[13] ASHRAE, 2010, "*ASHRAE Standard 55-2010*", Thermal Environment Standards for Human Occupancy. Atlanta, GA.

[14] Baker, N. 2014, *Natural ventilation-Stack ventilation* Available from: http://www.architecture.com/SustainabilityHub/Designstrategies/Air/1-2-1-2-Naturalventilation-stackventilation.aspx.

[15] Mathur, Jyotirmay, Bansal, N.K., Mathur, Sanjay, Jain, Meenakshi, and Anupma, 2006, "*Experimental investigations on solar chimney for room ventilation*", Solar Energy. 80: p. 927-935.

[16] Gan, G., 2000, "*Effective depth of fresh air distribution in rooms with single-sided natural ventilation*", ENergy and Buildings. 31: p. 65-73.

[17] Peren, J.I., Hooff, T.van, Leite, B.C.C., and Blocken, B., 2014, "*CFD analysis of cross-ventilation of a generic isolated building with asymmetric opening positions: Impact of roof angle and opening location*", Building and Environment. 85: p. 263-276.

[18] Nie, P., Zhou, J., Tong, B., Zhang, Q., and Zhang, G., 2015, "*Numerical study on the effect of natural ventilation and optimal orientation of residential buildings in Changsha, China"*, Procedia Engineering. 121: p. 1230-1237.

[19] Stoakes, P., Passe, U., and Battaglia, F., 2011, "*Predicting natural ventilation flows in whole buildings. Part 1: The Viipuri Library"*, Building Simulation. 4: p. 263-276.

[20] Stoakes, P., Passe, U., and Battaglia, F., 2011, "*Predicting natural ventilation flows in whole buildings. Part 2: The Esherick House"*, Building Simulation. 4: p. 365-377.

[21] Allocca, C., Chen, Q., and Glicksman, L.R., 2003, "*Design analysis of single-sided natural ventilation"*, Energy and Buildings. 35: p. 785-795.

[22] Cheuong, J. O.P. and Liu, C.H., 2011, "*CFD simulations of natural ventilation behaviour in high-rise buildings in regular and staggered arrangements at various spacings"*, Energy and Buildings. 43: p. 1149-1158.

[23] Park, D., 2013, "*Numerical simulations of airflow and heat trnasfer in a room with a large opening"*, Virginia Tech, Blacksburg VA, USA, Thesis.

[24] Environmental. 2015, *Air Changes Per Hour ACH*. ALS Environmental; Available from: http://www.caslab.com/Air_Changes_Per_Hour_ACH_Meaning/.

[25] ASHRAE, 2012, "*Thermal Environmental Conditions for Human Occupancy"*, ANSI/ASHRAE Standard 55-2010.

[26] Khedari, Joseph, Boonsri, Boonlert, and Hirunlabh, Jongjit, 2000, "*Ventilation impact of a solar chimney on indoor temperature fluctuation and air change in a school building"*, Energy and Buildings. 32: p. 89-93.

[27] Khedari, Joseph, Rachapradit, Ninnart, and Hirunlabh, Jongjit, 2003, "*Field study of performance of solar chimney with air-conditioned building"*, Energy. 28: p. 1099-1114.

[28] Miyazaki, T., Akisawa, A., and Kashiwagi, T., 2006, "*The effects of solar chimneys on thermal load mitigation of office buildings under the Japanese climate"*, Renewable Energy. 31: p. 987-1010.

[29] Haghighi, A.P. and Maerefat, M. , 2014, "*Solar ventilation and heating of buildings in sunny winter days using solar chimney"*, Sustainable Cities and Society. 10: p. 72-79.

[30] Lee, Kwang Ho and Strand, Richard K., 2009, "*Enhancement of natural ventilation in buildings using a thermal chimney"*, Energy and Buildings 41: p. 615-621.

[31] U.S. Department of Energy. 2014, *EnergyPlus Energy Simulation Software*. Available from: http://apps1.eere.energy.gov/buildings/energyplus/energyplus_about.cfm.

[32] Al-Kayiem, Hussain H., Sreejaya, K.V., and Ul-Haq Gilani, Syed Ihtsham, 2014, "*Mathematical analysis of the influence of the chimney height and collector area on the performance of a roof top solar chimney"*, Energy and Buildings 68: p. 305-311.

[33] Punyasompun, Sompop, Hirunlabh, Jognjit, Khedari, Joseph, and Zeghmati, Belkacem, 2009, "*Investigation on the application of solar chimney for multi-storey buildings"*, Renewable Energy. 34: p. 2545-2561.

[34] Oz, S., Fogel, S., Dubosky, V., Ziskind, G., and Letan, R., 2004, "*Solar-Assisted Induced Ventilation of Small Field Structures"*, Journal Of Solar Energy Engineering. 126: p. 781-788.

[35] Ong, K.S. and Chow, C.C., 2003, "*Performance of a solar chimney"*, Solar Energy. 74: p. 1-17.

[36] Bassiouny, Ramadan and Koura, Nader, 2008, "*An anayltical and numerical study of solar chimney use for room natural ventilation"*, Energy and Buildings. 40: p. 865-873.

[37] El-Agouz, S.A., 2008, "*The effect of internal heat source and opening locations on environmental natural ventilation"*, Energy and Buildings. 40: p. 409-418.

[38] Cho, Y.J. and Awbi, H.B., 2007, "*A study of the effect of heat source location in a ventilated room using multiple regression analysis"*, Building and Environment. 42: p. 2072-2082.

[39] Park, D. and Battaglia, F., 2015, "*Effect of heat loads and ambient conditions on thermal comfort for single-sided ventilation"*, Building Simulation 8(2): p. 167-178.

[40] Cengel, Yunus A. and Afshin, J. Ghajar, 2011, "*Heat and Mass Transfer: Fundamentals and Applications"*. 4 ed. Heating and cooling for buildings 2011.

[41] Murakami, Shuzo, Kato, SHinsuke, and Zeng, Jie, 2000, "*Combined simulation of airflow, radiation and moisture transport for heat release from a human body"*, Building and Environment. 35: p. 489-500.

[42] Carven, Brent A. and Settles, Gary S., 2006, "*A computational and experimental investigation of the human thermal plume"*, Journal of Fluid Engineering. 128(6): p. 1251-1258.

[43] Stamou, A. and Katsiris, I., 2006, "*Verification of a CFD model for indoor airflow and heat transfer"*, Building and Environment. 41: p. 1171-1181.

[44] Incorporated, Ansys, 2009, "*Fluent 12.0 User's Guide"*.

[45] Incorporated, Ansys, 2009, "*13.2.4 Natural Convection and Buoyancy-Driven Flows (User's Guide)"*.

[46] Raithby, G.D. and Chui, E.H., 1990, "*A Finite-Volume Method for Predicting a Radiant Heat Transfer in Enclosures with Participating Media"*, J. Heat Transfer. 112: p. 415-423.

[47] Mathur, S.R. and Murthy, J.Y., 1999, "*Coupled ordinates method for multigrid acceleration of radiation calculations"*, Journal of Thermophysics and Heat Transfer. 13(4): p. 467-473.

[48] Chorin, A. J., 1968, "*Numerical solution of navier-stokes equations"*, Mathematics of Computation. 22: p. 745-762.

[49] Ferziger J.H., Peric M., 2002, "*Computational Methods for Fluid Dynamics"*. 3rd edition.

[50] J., Roache P., 1994, "*Perspective: A method for uniform reporting of grid refinement studies"*, International Journal of Heat and Fluid Flow. 24: p. 54-66.

[51] Richardson L., Gaunt A., 1927, "*The Deferred Approach to the Limit. Part I. Single Lattic. Part ll. Interpenetrationg Lattices"*, The Philosophical Transcations of the Royal Society

of London. Series A, Containing papers of a Mathematical or Physical Character, 116(3): p. 405-41.

[52] Incorporated, Ansys, 2009, "*FLUENT 12.0 User's Guide.*".

[53] Park, D. and Battaglia, F., 2015, "*Application of a Wall-Solar Chimney for Passive Ventilation of Dwellings*", Journal Of Solar Energy Engineering. 137(6).

[54] Incropera, F.P., DeWitt, D.P., Bergman, T.L., and Lavine, A.S., 2007, "*Fundamentals of Heat and Mass Transfer*", John Wiley and Sons, Inc.

[55] Roache, P.J., 1994, "*Perspective: A method for uniform reporting of grid refinement studies*", Journal of Fluids Engineering. 116(3): p. 405-413.

[56] Munson, Bruce R., Young, Donal F., Okiishi, Theodore H., and Huebsch, Wade W., 2009, "*Fundamentals of Fluid Mechanics*". Sixth edition ed. 2009: John Wiley & Sons, Inc.

[57] Kuwabara, Bruce, Auer, Thomas, Akerstream, Tom, Klym, Glen, Pauls, Mark, Opie, Kael, and Peterson, John, 2011, "*Harnessing Climate*", High Performing Buildings, American Society of Heating, Refrigerating and Air-conditioning Engineers, Inc.

[58] KPMB. 2009, *Manitoba Hydro Place - A Climate Responsive Design Model - Solar chimney*. Available from: http://www.manitobahydroplace.com/integrated-elements/solar-chimney/.

[59] Tan, Alex Yong Kwang and Wong, Nyuk Hien, 2012, "*Natural ventilation performance of classroom with solar chimney system*", Energy and Buildings. 53: p. 19-27.

[60] Bu, Zhen and Kato, Shinsuke, 2011, "*Wind-induced ventilation performances and airflow characteristics in an areaway-attached basment with a single-sided opening*", Building and Environment. 46: p. 911-921.

[61] Bu, Zhen, Kato, Shinsuke, and Takahashi, Takeo, 2010, "*Wind tunnel experiments on wind-induced natural ventilation rate in residential basements with areaway space*", Building and Environment. 45: p. 2263-2272.

[62] About.com. 2015, *Busiest Subways-The world's Busiest Subway Systems in Major Cities*. Available from: http://geography.about.com/od/urbaneconomicgeography/a/Busiest-Subways.htm.

[63] Brauner, EV, Frederiksen, M, Kolarik, B, and Gunnarsen, L, 2014, "*Typical benign indoor aerosol concentrations in public spaces and designing biosensors for pathogen detection: a review*", Building Environment. 82: p. 190-202.

[64] Kim, M, Liu, H, Kim, JT, and Yoo, C, 2013, "*Sensor fault identification and reconstruction of indoor air quality (IAQ) data using a multivariate non-Gaussian model in underground building space*", Energy Building. 66: p. 384-94.